Title

Theory of Positivity-Preserving Numerical Methods for Thin Viscous Liquids Flowing Down Vertical Fibers

Author

Kim, Bohyun

Publication Date

2023

Peer reviewed|Thesis/dissertation

UNIVERSITY OF CALIFORNIA
Los Angeles

Theory of Positivity-Preserving Numerical Methods for Thin Viscous Liquids Flowing Down Vertical Fibers

A dissertation submitted in partial satisfaction
of the requirements for the degree
Doctor of Philosophy in Mathematics

by

Bohyun Kim

2023

ABSTRACT OF THE DISSERTATION

Theory of Positivity-Preserving Numerical Methods for Thin Viscous Liquids Flowing Down Vertical Fibers

by

Bohyun Kim
Doctor of Philosophy in Mathematics
University of California, Los Angeles, 2023
Professor Andrea Bertozzi, Chair

A thin liquid film flowing down a vertical fiber exhibits complex and captivating interfacial dynamics of an unsteady flow, including the formation of droplets, irregular traveling waves, and a string of beads. The dynamics of traveling beads are particularly applicable in various fluid experiments due to their high surface-area-to-volume ratio, which enhances gas diffusion towards the liquid surface. Recent studies verified that when the flow undergoes regime transitions, the motion of the film thickness changes dramatically. The dynamics of the liquid film are influenced by the cylindrical geometry of the fiber and the presence of stabilizing and destabilizing forces, which pose additional challenges for numerical simulations. Many current numerical simulations of fiber coating dynamics, such as direct numerical simulation (DNS), rely on the full Navier-Stokes equations. Such numerical simulations incur significant computational costs, often requiring several days on a desktop computer. As a result of the high computational cost, it is not feasible to simulate regime transitions or extend the computational domain further downstream of the fluid.

In order to overcome these challenges, several reduced-order models using lubrication

approximations have been developed. These models are much simpler than the full Navier-Stokes equations, yet they are capable of capturing droplet dynamics and transient patterns of the flow. However, these models have drawbacks in terms of their versatility, as one needs to modify the form of the equations depending on the assumptions made regarding boundary conditions and the scales of the problem. Depending on the boundary conditions at the solid-liquid interface, one may observe singularities, cusps, and non-classical shocks in finite time. If one were to consider a liquid film with a moderate thickness or a moderate Reynolds number, the resulting equation would exhibit significant differences.

In this dissertation, we consider a model for fiber coating at low Reynolds numbers with geometry such that the fluid thickness is larger than the fiber radius. We present a computationally efficient numerical method that can maintain the positivity of the film thickness as well as conserve the volume of the fluid in a coarse mesh setting. Our method allows simulations of regimes with isolated droplets and the Rayleigh-Plateau instability, commonly observed in laboratory experiments but particularly difficult to simulate. We create our positivity-preserving numerical method in the following way. First, we present a conserved and dissipative quantity for our continuous model. Next, we construct a continuous in time and discrete-in-space numerical method that satisfies the discrete equivalent of conservation of mass and an entropy estimate. We provide a proof of the positivity of our numerical method using a priori and a posteriori bounds and a proof of second-order consistency. Finally, we show that our method can be implemented efficiently using an adaptive time-stepping method to describe solutions that correspond quantitatively to laboratory experiments.

The dissertation of Bohyun Kim is approved.

Christina Kim

Marcus Leigh Roper

Yongho Ju

Andrea Bertozzi, Committee Chair

University of California, Los Angeles

2023

TABLE OF CONTENTS

LIST OF FIGURES

LIST OF TABLES

ACKNOWLEDGMENTS

First and foremost, I would like to express my gratitude to my advisor Dr. Andrea Bertozzi, who has guided my Ph.D. journey as a mentor, teacher, and academic role model for the past six years. Words cannot express my gratitude for your sincere encouragement throughout graduate school. In moments of difficulty and doubt, you firmly believed in my capabilities. Your trust has been a cornerstone in allowing me to focus on my studies and pursue my dream career fully. I have shed a few tears at your honest yet insightful remarks, but such priceless words have become my lifelong lesson to carry. I am truly fortunate to have you as my Ph.D. advisor.

Next, I would like to extend my gratitude to Dr. Hangjie Ji, whom I consider to be a significant contributor and secondary advisor to my Ph.D. research. When I first met you during the 2019 Division of Fluid Dynamics conference, I was fragile and uncertain about my future. You have been a constant source of emotional support throughout my Ph.D. journey. Your expertise, insights, and dedication to the field of research have been truly inspiring. Thank you for your guidance and support, and for being a source of inspiration throughout this journey.

To my committee member, Inwon, I must admit that I initially felt intimidated by your presence. However, the anxiety has motivated me further to grow as a mathematician. I appreciate this a lot. I also love PDE now. To my committee member, Marcus, your passion for mathematical modeling and dedication to teaching has consistently served as a source of inspiration for me. Thank you for being a role model and mentor. To my committee member, Sungtaek, even though our interactions may have been few, I want to express my appreciation for the collaboration. I have watched your captivating fluid videos from the lab too many times. The collaboration opportunity made me seriously like fluid dynamics.

I would like to express my gratitude to Dr. Leah Zhornitskaya, whose inspiration has been instrumental in writing the thesis. She has ignited my passion for learning PDE and

numerical methods for the past two years, for which I am truly grateful.

I enjoyed collaborating with Prof. Bertozzi's postdocs and students, who also inspired me to produce wonderful research. Thank you for the helpful discussions with Sean Carney, Eric Hester, Weiqi Chu, Yoni Dukler, and Jason Brown.

I acknowledge the following reprinted images used in Figure 3.1 from [KRS12b, PN03], Figure 3.2 from [KRS12a, SAB94], Figure 3.4 from [ZSJ18, SZJ17], Figure 3.5 from [JFS19], and Figure 5.1 from [GB21]. The permission was granted for the thesis title "Theory of positivity-preserving numerical methods for thin viscous liquid films", but the title has changed and the permission was again requested for "Theory of Positivity-Preserving Numerical Methods for Thin Viscous Liquids Flowing Down Vertical Fibers". I acknowledge the work of [ZB00] for the reproduced images in Figure 2.1-2.3 and the work of [BGW01] for the reproduced image in Figure 2.4.

Chapter 4 is adapted from [KJB23], and I acknowledge my coauthors, Hangjie Ji, Andrea L. Bertozzi, Abolfazl Sadeghpour, and Y. Sungtaek Ju. Hangjie Ji contributed to mathematical modeling and provided insight into the problem, and I designed the positivity-preserving numerical method. Andrea L. Bertozzi guided and provided directions for the research. Albofazl Sadeghpour and Y. Sungtaek Ju provided laboratory experimental data and details of the experiments.

I would also like to express my gratitude for the generous funding provided by the Simons Math + X Investigator Award (Grant No. 510776), UCLA Eugene V. Cota-Robles Fellowship, and the NSF grant DGE-1829071, which supported the research presented in this thesis. The research in Chapter 4 was supported by the Simons Foundation Math + X Investigator Award number 510776, Faculty Research and Professional Development Program (FRPD) provided by NC State University, and the NSF grant DGE-1829071. I acknowledge all of these grants.

I would like to express my gratitude to all my friends from both my undergraduate and

graduate studies. I am truly fortunate to have shared this journey with such a remarkable group of individuals. Thank you, Sharat Chandra, Kevin Bui, Shyr-Shea Chang, Michael Puthawala, Gyu Eun Lee, Blaine Talbut, Christopher Shriver, Kaitlyn Shriver, Paul Han, Chanel Han, Thomas Tu, Siting Liu, Victoria Kala, Yuzo Makitani, and Brian Barch.

I am also deeply indebted to the professors who have significantly shaped my passion for mathematics since my undergraduate studies. I would like to express my appreciation to Dr. Hongkai Zhao, Dr. Jack Xin, Dr. Alessandra Pantano, Dr. Natalia Komarova, Dr. Deanna Needell, and Dr. Yifei Lou.

To my dear friends Hyunjin, Hyewon, and Jiyeon, even though you are in South Korea, your support and eternal friendship have meant the world to me. Despite the distance, your constant encouragement and presence have been a source of comfort.

I would like to acknowledge my family, who has supported me and encouraged me to pursue higher education beyond college. Dad, you were a bit too insistent on me earning a Ph.D., but I am glad I did in the end. Mom, you always told me to quit the program because I worked too hard, but I know you were rooting for me from the bottom of your heart on the days I got stuck. My younger brother Sewon, thank you for cheering me on throughout graduate school, and I owe you countably many burritos that have given me mathematical inspiration to finish my Ph.D. Ajossi, you always claimed that Adidas manufactures the best shoes, but I finally understood what you meant, thanks to my Ph.D. study.

Finally, this endeavor would not have been possible without Kyung Ha, my fiancée and my lifelong math friend. You were always there to give me a loving hug whenever I was sad, angry, or happy. You have made my experience at UCLA exceptional and unforgettable since our first date at the local ramen restaurant, Daikokuya, on November 5th, 2016. I am grateful to have you as a partner with whom I can discuss, joke about, and be madly in love with math for the rest of my life.

VITA

2016	B.S. in Mathematics and Minor in Computer Science, University of California, Irvine
2016–2018	Teaching Assistant, Mathematics Department, University of California Los Angeles (UCLA)
2019	Research Mentor for Research Experience for Undergraduate at UCLA
2022	Instructor, UCLA

PUBLICATIONS

Kim, B., Ji, H., Bertozzi., A., Sadeghpour A., Ju, S. "A positivity-preserving numerical method for a thin liquid film on a vertical cylindrical fiber (submitted for publication)." In *Journal of Computational Physics*.

Kim, B., Lou, Y. "Two-Step Blind Deconvolution of UPC-A Barcode Images." In: Demir, I., Lou, Y., Wang, X., Welker, K. (eds) *Advances in Data Science. Association for Women in Mathematics Series*, vol 26 (2021), Springer, Cham. *https://doi.org/10.1007/978-3-030-79891-8_3*.

Birns, S., **Kim, B.**, Ku, S., and Stangl, K. "A Practical Study of Longitudinal Reference-Based Compressed Sensing for MRI." In *Rose-Hulman Undergraduate Mathematics Journal*, Vol. 17, Iss. 2, Article 1 (2016), *https://scholar.rose-hulman.edu/rhumj/vol17/iss2/1*.

CHAPTER 1

Introduction

When a thin, annular layer of liquid flows down a narrow vertical cylindrical fiber, such as a hair or a microscale tube, one can observe a fascinating physical phenomenon: an unstable flow exhibiting complex traveling waves and bead patterns [Que90, KDB01, Lor78, XD85, Que99]. Several patterns emerge, including traveling beads patterns that create high-curvature regions that act as radial sinks. These patterns provide suitable geometry to design devices for heat transfer [ZWJ15, HIM94] and mass transfer [CUM00, GLH12] along the liquid-gas interfaces [SZJ19, GB21]. Such devices have application in various fields of engineering [ZSW17, ZSJ18, UMO03, GLH12, CUM00, SZJ19], motivating comprehensive theoretical and experimental studies over the last few decades [Que90, CD99, CM09, RTG09, RTG08, KRS12c, RK12, JFS19, JFS21]. Although there have been many comprehensive theoretical and experimental studies, numerical methods for simulating the traveling waves and bead patterns have not been explored in depth. In this thesis, we focus on designing numerical methods for efficiently simulating the coating flow on a vertical cylindrical fiber.

To better comprehend and create numerical methods for the coating flow on a vertical cylindrical fiber, it is necessary to investigate models that use lubrication approximation. Lubrication approximations are applied to simplify the Navier-Stokes equations and study the dynamics of thin liquid films [BB02]. The study of thin liquid films is a well-developed field with numerous models describing case-by-case situations. Examples include a model for the rain flowing down a window [Mye98], the drying process of paint layers [Mye98], a fluid drop spreading on a surface [Mye98], the deicing process on an airplane wing [MCT02],

the tears of wine phenomenon [DJF20], and many others. Myers provided a comprehensive review article on thin-film flow driven by surface tension, highlighting the significant role of surface tension in determining the dynamics of thin liquid flow [Mye98]. We refer readers to [ODB97, CM09] for more recent reviews.

The lubrication approximation is valid when the thickness of the liquid film is much smaller than its length scale. These equations are simpler in structure, making it easier to design numerical methods. However, it is still not simple enough to consider lubrication-type equations that approximate coating flows because they typically incorporate many different nonlinear terms to describe the intricate flow dynamics. Thus, we first review the simplest equation involving lubrication approximation to set the stage for the thesis: an equation describing thin liquid flow on a solid substrate.

1.1 Lubrication equation derivation: a thin liquid film on a solid surface

In this section, we derive the most basic form of a lubrication equation from the Navier-Stokes equations, modeling a viscous fluid on a solid substrate. The equation describes the flow where the pressure is dominated by surface tension and negligibly affected by other complex forces. We follow the derivation and analysis by Bertozzi et al. [BBD94], but [KCD16] provides an alternative discussion in depth.

Consider a two-dimensional Newtonian flow of a thin liquid film on a solid substrate, as described in Figure 1.1. Assuming that the thickness of the liquid film is much smaller than the length scale, a lubrication equation can be derived from the following two-dimensional

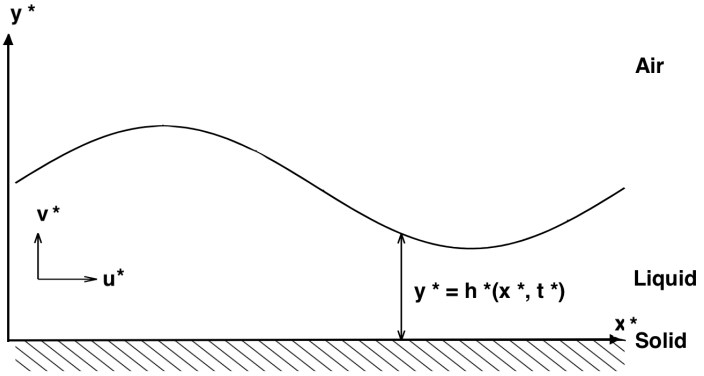

Figure 1.1: Illustration of a two-dimensional thin viscous liquid on a solid surface.

Navier-Stokes Equations [Bat67, KCD16],

$$u^*_{t^*} + u^* u^*_{x^*} + v^* u^*_{y^*} = -\frac{p^*_{x^*}}{\rho} + \nu \left(u^*_{x^* x^*} + u_{y^* y^*} \right), \tag{1.1}$$

$$v^*_{t^*} + u^* v^*_{x^*} + v^* v^*_{y^*} = -\frac{p^*_{y^*}}{\rho} + \nu \left(v^*_{x^* x^*} + v_{y^* y^*} \right), \tag{1.2}$$

$$u^*_{x^*} + v^*_{y^*} = 0. \tag{1.3}$$

Equations (1.1)-(1.3) represent the dimensional Navier-Stokes equations, where u^* and v^* represent the fluid velocity in the x and y direction, respectively, and p denotes the pressure. The density ρ and the kinematic viscosity ν of the fluid are assumed to be constants. Various boundary conditions can be considered, but the simplest conditions at the solid-liquid interface are the no-slip [BBD94] and no-penetration [CM09] boundary conditions,

$$u^* = 0, \quad v^* = 0 \quad \text{at} \quad y^* = 0. \tag{1.4}$$

In order to derive the lubrication equation for the thin viscous film, we need to nondimensionalize the equations using an appropriate scaling. We adopt the scaling suggested by [KCD16],

$$\begin{aligned} &x = x^*/L, \quad y = y^*/H, \quad u = u^*/U, \quad v = v^*/V, \\ &t = t^* U/L, \quad p = p^*/P, \end{aligned} \tag{1.5}$$

where L is a characteristic length scale of the film, H is a characteristic thickness scale of the film, U is a characteristic velocity of the flow in the x direction, V is a characteristic velocity of the flow in the y direction, and P is the atmospheric pressure. As we scale the continuity equation (1.3) with Equation (1.5),

$$\frac{U}{L}u_x + \frac{V}{H}v_y = 0. \tag{1.6}$$

As a result,

$$\frac{U}{L} \sim \frac{V}{H} \implies V \sim \frac{H}{L}U \sim \epsilon U, \tag{1.7}$$

for $\epsilon = H/L \ll 1$. This assumption makes sense since the thickness scale H is much smaller than the length scale L. Using the above assumption (1.7) and the scaling (1.5), we simplify Equations (1.1)-(1.3) as the following,

$$\epsilon^2 Re(u_t + uu_x + vu_y) = -\frac{1}{\Lambda}p_x + \epsilon^2 u_{xx} + u_{yy}, \tag{1.8}$$

$$\epsilon^4 Re(v_t + uv_x + vv_y) = -\frac{1}{\Lambda}p_y + \epsilon^4 v_{xx} + \epsilon^2 v_{yy}, \tag{1.9}$$

$$u_x + v_y = 0, \tag{1.10}$$

where $Re = UL/\nu$ is the Reynolds number, and $\Lambda = \mu UL/PH^2$. Assuming that we choose the scaling coefficients correctly, all the dimensionless derivative terms should be of order one [KCD16]. In other words, $\Lambda = O(1)$. Note that we assume $Re = O(1)$ due to the viscosity of the fluid. In addition, using $\epsilon = H/L \ll 1$, we collect the leading order terms,

$$\frac{1}{\mu}p_x = u_{yy}, \tag{1.11}$$

$$\frac{1}{\rho}p_y = 0, \tag{1.12}$$

$$u_x + v_y = 0, \tag{1.13}$$

where μ is the dynamic viscosity of the fluid.

Equation (1.11)-(1.13) is the simplest form of the lubrication approximation producing a zeroth-order approximation of the Navier-Stokes equations.

In order to derive the evolution equation of liquid film $h(x,t)$, we solve Equation (1.11)-(1.13) with respect to boundary conditions at the solid-liquid interface and liquid-gas interface. At the solid-liquid interface, an immense frictional force is applied to the liquid, whereas the tangential component of the liquid stress tensor vanishes at the liquid-gas boundary. Thus, the gradient of u_y is inevitably large across the thin film [BBD94]. We integrate Equation (1.11) with respect to y and use the boundary condition at the liquid-gas interface to get

$$u = \frac{p_x}{\mu}\left(\frac{y^2}{2} - hy - B\right). \tag{1.14}$$

Here, we use B to represent the interaction at the solid-liquid interface. Averaging Equation (1.14) in the y direction, we get

$$\bar{u} = -\frac{p_x}{3\mu}(h^2 + 3B). \tag{1.15}$$

Finally, the conservation of mass implies that

$$h_t + (\bar{u}h)_x = 0. \tag{1.16}$$

Hence,

$$h_t + \left(\frac{\gamma}{3\mu}(h^3 + Bh)h_{xxx}\right)_x. \tag{1.17}$$

Here, the pressure jump is estimated by the Gibbs-Thompson relation, $\Delta p = \gamma\kappa$[1], where γ is the surface tension and κ is the mean curvature of the liquid-gas interface. We may approximate $\kappa \simeq h_{xx}$, assuming the surface tension to be dominant. The value of B is determined by boundary conditions at the solid-liquid interface. We assume $B = 0$ when the thickness scales $h \gg H$, corresponding to the no-slip boundary condition [BBD94]. When the surface is porous, $B = \alpha$, where α represents the degree of porosity of the surface [NM83]. In the case of the Navier slip condition, $B = ch$, where c represents the amount of slippage [Gen85].

[1]Here, we use Δ to denote the difference. If it is used in PDE, we use it to denote the Laplacian. If it is used in the numerical method, it is used to denote the difference. The meaning of each should be clear from the context.

1.2 Model lubrication equation

Lubrication-type equations frequently share the following characteristics; h is sufficiently small compared to the length scale L, and the flux is dominated by the same functional form other than differences in the exponent of h. In the case of Equation (1.17), the flux is $\frac{\gamma}{3\mu}(h^3 + Bh)h_{xxx}$. Other types of fluid dynamics can be considered by slightly changing the flux. For example, we can generalize Equation (1.17) by

$$h_t + (f(h)h_{xxx})_x = 0, \quad f(h) \sim h^n. \tag{1.18}$$

Altogether, Equation (1.18) allows us to model Hele-Shaw flow when $n = 1$, polymeric liquids when $n = 2$, and macroscopic thin films when $n = 3$ in a single equation. Often, one considers $f(h) \sim h^n$, $n \in (0, 3)$. We discuss this further in Chapter 2.

1.3 The scope of the thesis

The thesis reviews and investigates topics in designing positivity-preserving numerical methods for lubrication-type equations, particularly focusing on fiber coating equations. In Chapter 2, we provide a literature review of positivity-preserving numerical methods for lubrication-type equations. In addition, topics on the analysis of higher-order nonlinear PDEs, positivity-preserving numerical methods for parabolic PDEs, and the application of numerical methods are reviewed. After the literature review, we discuss the necessary ingredients to design positivity-preserving numerical methods and reproduce numerical simulations of existing positivity-preserving methods. In Chapter 3, we review previous research on the fiber coating problem, including experimental and theoretical studies. We primarily focus on mathematical models of a thin liquid film flowing down a vertical fiber and derive the current state-of-the-art model used in Chapter 4. In Chapter 4, we present a novel positivity-preserving numerical method for a fiber coating equation as our contribution. Our method is computationally efficient and maintains the positivity of the film thickness while conserving the volume of

the fluid under coarse mesh settings. This chapter also includes simulations of the numerical method compared with experimental data and a previously proposed numerical method. Finally, in Chapter 5, we conclude the thesis with a few remarks and suggest future research directions.

CHAPTER 2

Positivity-preserving numerical methods

2.1 Literature review of positivity-preserving numerical methods

In this section, we provide a literature review of positivity-preserving numerical methods for lubrication-type equations. We have specifically focused on articles that cited the work of Zhornitskaya & Bertozzi [ZB00], which include over 161 articles. We have divided them into four categories and summarized the work of a few representative articles from each category for the readers' convenience.

2.1.1 Prior work on positivity-preserving numerical methods for lubrication-type equations

In this section, we review the articles that studied positivity-preserving schemes on lubrication-type equations. Such articles include ones that designed a novel positivity-preserving (or nonnegativity-preserving) numerical method, analyzed positivity-preserving (or nonnegativity-preserving) numerical methods, or presented extensive studies on the simulation of positivity-preserving (or nonnegativity-preserving) numerical methods. The articles in this category are the most relevant to the thesis.

First, we focus on articles that designed numerical schemes for the basic lubrication equation (2.40) with or without a generalized pressure term [ZB00, WB03, Gru03, GR00, GR01, GBR02]. Among them, we specifically point out the following articles from Zhornitskaya & Bertozzi [ZB00], Grün [Gru03], Grün & Rumpf [GR00], and Witelski & Bowen [WB03].

These articles are highly relevant and foundational in understanding the problems discussed throughout the thesis.

Zhornitskaya & Bertozzi [ZB00] proposed a novel positivity-preserving finite difference method for simulating lubrication-type equations of the form (2.40). Their work is particularly inspiring for the thesis because it is desirable to design a positivity-preserving numerical method that allows efficient simulation of fiber coating dynamics with coarse spatial resolution. The numerical method ensured the positivity of the solution regardless of the spatial resolution in one dimension and was extended to two dimensions assuming additional regularity of analytical solutions. Prior numerical methods commonly required significant grid refinement to simulate solutions near singularities. Through a series of simulations, Zhornitskaya & Bertozzi demonstrated that their method could compute solutions near singularities by calculating a regularized PDE (see Section 2.3.1). Such a regularization technique is effective for studying singularity formation and defining solutions beyond the singular time. The method preserved the positivity of numerical solutions even when the continuum PDE was known to only preserve nonnegativity. The authors established proofs of second-order consistency, stability near a flat state, and convergence of the numerical method, which can serve as guidelines for proving such properties of more complex numerical methods. The article also provided a finite element generalization of the numerical method, which allowed simulations on nonuniform grids (e.g., a locally refined grid near singularities).

In [GR00], Grün & Rumpf presented a nonnegativity-preserving finite element numerical scheme for the basic fourth-order lubrication equation (2.40) that models the time evolution of film thickness of a viscous liquid. The paper established proofs of the convergence and nonnegativity-preserving properties of the numerical scheme. This paper produced a significant improvement to the finite element method proposed by Barrett et al. [BBG98] because the method guarantees nonnegativity independent of the grid size. Discrete solutions are guaranteed to be positive under restricted conditions, which is the major difference from the results provided by Zhornitskaya & Bertozzi [ZB00]. The method solved for a

discrete solution in time and space that preserves qualitatively desired properties such as the nonnegativity, a uniform discrete Hölder continuity, and a discrete analog of an energy estimate. The article also established proofs of the existence and compactness in time of discrete solutions.

In [WB03], Witelski & Bowen developed an alternating direction implicit (ADI) method to solve a fourth-order thin film PDE for a surface-tension-driven flow. The proposed ADI method is second-order accurate and unconditionally stable for linear problems with constant coefficients but has solution-dependent stability and convergence properties for nonlinear problems. Regardless, the authors not only proposed a framework for creating a two-dimensional numerical method for lubrication-type equations but also extended the ADI method to the following generalized higher order linear parabolic PDE explored by Bernis & Friedman [BF90],

$$u_t + (-1)^{m-1}\nabla \cdot (f(u)\nabla\nabla^{2m}u) = 0, \quad m = 2, 3, \cdots . \tag{2.1}$$

A self-similar solution was simulated for equation (2.40) with $f(h) = h$ by the Grün & Rumpf's nonnegativity-preserving method [GR00].

In [Gru03], Grün presented a finite element scheme for a lubrication-type equation incorporating nonlinear pressure terms such as van der Waals interactions in multiple space dimensions. The author considered equation (2.53) presented in Section 2.3.2. As a by-product of an entropy and energy estimate, results on the existence and positivity of discrete solutions almost everywhere were established to equations with singular lower-order terms. This was a generalization of the work of [GR01] to multiple space dimensions.

The study of moving contact lines is a well-recognized topic that has been investigated along with lubrication-type equations. It is often the case that the front of the thin fluid becomes unstable, developing a wavy pattern such as fingering instability [Mun04, KD01] and saw-tooth [Kal00, KD01] patterns. These instabilities are not desirable for technical applications in engineering, chemistry, and biology since they may form dry regions [KD01]. Therefore, the

problem introduced plenty of articles that investigated simulations of positivity-preserving numerical methods in the context of moving contact lines of thin film droplets [DK02, DKB00, MW05, Gom12, SRX07].

One representative article was published by Diez and Kondic [DK02], in which the authors presented a computational method for calculating quasi-three-dimensional unsteady flows, specifically the coalescence of a linear array of sessile drops of thin liquid films on a solid, horizontal substrate. The authors used a modified positivity-preserving scheme by Zhornitskaya & Bertozzi [ZB00] to avoid "false" (negative) singularities caused by a numerical method near the moving fronts. According to a series of numerical experiments, the equivalent results were observed from both the precursor film model and the slip model, while the precursor model significantly reduced the computational cost. Numerical simulations were presented for the different grid resolutions. The method captured the topological transitions of the flow, such as merging or a rupture of a film, and incorporated additional driving mechanisms of the fluid dynamics, such as centrifugal, thermocapillary, or van der Waals forces. While the quadratic convergence to the exact solution for radial and elliptic drops was discussed, a mathematical proof was not provided.

Another article discussing the numerical method in the context of moving contact lines was introduced by Münch and Wagner [MW05]. The authors mainly focused on linear stability analysis of a lubrication-type equation and extended the model to incorporate the full nonlinear curvature. The model described the dewetting process of a thin polymer film on a hydrophobized substrate driven by van der Waals forces under the no-slip or slip condition. The authors observed that a small perturbation of the receding front was amplified in the slip case by orders of magnitude larger than in the no-slip case. The authors observed that the slip case had asymmetric protrusions extending toward the trench, while for the no-slip case, the protrusions were symmetrical.

Positivity-preserving numerical methods for lubrication equations also have been discussed in the context of identifying dewetting patterns of a thin film. For example, Becker et

al. [BGS03] presented a numerical simulation of dewetting dynamics of a thin film with a semi-implicit linear finite element method. The method was derived from the nonnegativity-preserving numerical method from Grun & Rumpf [Gru03, GR00] because the model incorporated nonlinear pressure effects. The numerical simulations were in good agreement with highly controlled laboratory experiment data for various film-rupture patterns. Normalized Minkowski functionals were used for calculating sums over weighted pixels for digitized data laboratory experiments and simulations and analyzing the dewetting patterns.

Since thin film flows driven by gravity can be observed on an inclined surface, positivity-preserving numerical algorithms in this context were also investigated [KD01, Aja04, BGL02, MWW18, DKB00]. For example, Kondic & Diez [KD01] presented fully nonlinear time-dependent simulations of a thin liquid film flowing down an inclined plane, assuming a complete wetting situation. The authors investigated film instability patterns with nonlinear waves, such as fingering instabilities and saw-tooth wave patterns at varying inclination angles and sizes of the domain. The numerical schemes proposed by Zhornitskaya & Bertozzi [ZB00] were verified to be significantly efficient in [DKB00]. The authors ensured the work was specifically restricted to cases where the fluid thickness is kept constant far behind the apparent contact line. Such configuration allows one to understand many features of the moving contact line problem without introducing additional complications, such as the effect of shear thinning given a constant volume of the fluid.

Several articles were discussed in the context of Hele-Shaw cell equations [LGB07, GT06, PRT04]. Lu et al. [LGB07] proposed a diffuse-interface model describing the motion of Hele-Shaw cell drops that undergo topological changes by the effect of electrowetting. The model describes the fluid interfacial dynamics through a nonlinear Cahn–Hilliard equation of one phase-field variable. A series of asymptotic analyses were carried out, assuming a small interface thickness. Consequently, the asymptotic analysis showed that the model in the article is equivalent to Hele-Shaw flow with voltage-modified Young–Laplace boundary conditions on the free surface. The contact angles and their effect on the model are also

discussed

Gosse & Toscani [GT06] derived a nonnegativity-preserving numerical method and expanded the theoretical and numerical study of Hele-Shaw cell models. The authors utilized an idea from mass transportation to develop a simple numerical scheme that is stable, entropy-decreasing, and convergent toward the unique solution of the continuous problem. Homogeneous cooling states of the problem are displayed numerically. Section 5 of the paper is entirely devoted to the study of a mollified Hele-Shaw cell equation for which the authors proposed a nonnegativity-preserving scheme based on entropy estimates and numerical results. A numerical example of Hele-Shaw cell film rupture was presented as well.

Another topic that was investigated in depth is lubrication-type equations in the context of the thermocapillary migration of flow on a heated surface [GH10, AW03, AK09, Gom12, TKS07]. For example, Ajaev & Wilis [AW03] develop a mathematical model of the thermocapillary flow of thin films of molten metals to study the rupture of the film under two different patterns: point rupture and ring rupture. The model is formulated assuming that the laser beam radius is much larger than the thickness of the molten metal. By analyzing numerical simulations, the authors concluded that the transition between two rupture patterns depends on the disjoining pressure. The proposed model slightly deviates from standard lubrication-type equations because it incorporates a nonlinear evaporative flux term, an unsteady heat conduction term, and a positive disjoining pressure term.

Several other topics are discussed in the context of positivity-preserving numerical methods for lubrication-type equations. Some examples include: polymer flow [SMC12, PHM19]; flow driven by surfactant [BN04, BGL02, LPD19]; flow with stochastic noise [NCM15, FG18], stochastic porous-media flow [GG19], evaporative flow [KA09], capillary-driven flow [BSR13], laminar flow with a free liquid-gas interface [OM17], flow on a media during a heat-assisted magnetic recording (HAMR) process [Raj13], blood flow in the vicinity of atheroma [Chu10], simulation of flow at real-time frame rate [VRB18], and many more. We *especially* focus on the following articles [GR01, DK02, DKB00, BGL02, SRX07, PHM19, Gom12, VRB18, Chu10,

GR00, WB03, GBR02, Gru03, GT06, PRT04, BN04, PHM19, LPD19, FG18, LHV13]. These articles presented a numerical scheme that solves equations similar to our main problem (2.41). Many of them include proofs of the positivity of numerical solutions and the convergence of numerical methods. For example, Lu et al. [LHV13] designed a numerical scheme utilizing cut-off methods. The convergence analysis and applications demonstrated that a cutoff method is an effective tool for computing nonnegative solutions.

2.1.2 Prior work on the positivity of continuous solutions of lubrication-type equations

In this section, we review the articles that proved the analytical properties of lubrication-type equations, such as proving the existence of a strong or weak solution and the positivity of analytical solutions. It is crucial to understand the properties of the continuous solution of PDE when designing numerical methods because one can often construct the discrete equivalent of those properties [ZB00, GR00, GR01, Gru03, BBG98]. If one can incorporate those discrete properties in numerical methods, it is possible to construct positivity-preserving, or even better, other physical properties preserving numerical methods [ZB00, GR00, GR01, Gru03, BBG98].

Bernis & Friedman set the stage for studying higher-order nonlinear degenerate parabolic equations of the form

$$\frac{\partial h}{\partial t} + (-1)^{m-1}\frac{\partial}{\partial x}\left(f(h)\frac{\partial^{2m+1}h}{\partial x^{2m+1}}\right) = 0, \tag{2.2}$$

where

$$f(h) = |h|^n f_0(h), \quad f_0(h) > 0, \quad n, m \geq 1. \tag{2.3}$$

Such an equation arises in modeling viscous droplets spreading over a solid surface [Gre78, GM81, Hoc81, Lac82] and also in the oxidation of silicon in semiconductor devices [Kin89, TK87]. In such cases, $f(h)$ often takes the form of $f(h) = |h|^3 + o(|u|^3)$ as $|h| \to 0$. The authors provided a general framework for analyzing PDEs of the form (2.2) to establish

results such as the existence of a smooth weak solution or a proof of the nonnegativity of a solution. The authors introduced a quantity later referred to as entropy and established a bound on the entropy to prove the positivity of a continuous solution. The entropy estimate technique is still used in recent work, such as [JTC22, CPT10].

We illustrate an example for the simplest case,

$$\begin{aligned} &h_t + (f(h)h_{xxx})_x = 0 \quad \text{in} \quad Q_{T_0} = \Omega \times (0, T_0), \\ &h(x, 0) = h_0(x), \quad h_0 \in H^1(\Omega), \end{aligned} \tag{2.4}$$

where $m = 1$ for $T_0 > 0$ and Ω bounded, e.g., $\Omega = \{-a < x < a\}$. One can impose simple boundary conditions such as

$$h_x = h_{xxx} = 0 \quad \text{on} \quad x = \pm a. \tag{2.5}$$

The authors assumed that

$$f(h) = |h|^n f_0(h), \quad f_0 \in C^{1+\alpha}(\mathbb{R}^1), \quad f_0 > 0, \quad \alpha \in (0, 1), \quad n > 1. \tag{2.6}$$

Equation (2.4) is degenerate at $h = 0$. By regularizing this to a uniformly parabolic equation, one can use classical Schauder theory to prove local existence. This can be done by adding a small diffusion term with $\epsilon > 0$ to the equation and relaxing the initial condition to an approximating $C^{4+\alpha}$ function,

$$\begin{aligned} &h_t + ((f(h) + \epsilon)h_{xxx})_x = 0 \quad \text{in} \quad Q_{T_0} = \Omega \times (0, T_0), \\ &h(x, 0) = h_{0\epsilon}(x), \quad h_{0\epsilon} \in C^{4+\alpha}(\Omega). \end{aligned} \tag{2.7}$$

This example will be discussed for both showing the existence of a smooth weak solution and proving the nonnegativity of the weak solution.

First, we focus on the framework for showing the existence of a smooth weak solution. The procedure is detailed in Sections 2 and 3 of their work [BF90]. Equation (2.7) is not degenerate so that one can apply the parabolic Schauder estimates [Fri58, Sol65] to show

that the equation admits a unique solution for a short time interval Q_σ, for small $\sigma > 0$. The Schauder estimates also guarantee a Hölder condition of

$$h_t, h_x, h_{xx}, h_{xxx}, h_{xxxx} \quad \text{in} \quad \overline{Q_\sigma}. \tag{2.8}$$

Additional smoothness properties are guaranteed for the solution h_ϵ of the regularized PDE (2.7) on Q_σ. These include

$$|h_\epsilon(x,t)| \leq A, \tag{2.9}$$

$$|h_\epsilon(x_2,t) - h_\epsilon(x_1,t)| \leq K|x_2 - x_1|^{1/2}, \tag{2.10}$$

$$|h_\epsilon(x,t_2) - h_\epsilon(x,t_1)| \leq M|t_2 - t_1|^{1/8}, \tag{2.11}$$

for arbitrary $x_1, x_2, x, t_1, t_2, t \in Q_\sigma$, where constants A, K, and M are independent of σ and ϵ. In other words, one can find an upper bound on the $C_{x,t}^{1/2,1/8}$-norm of h_ϵ in Q_σ, which allows one to extend the solution h_ϵ to Q_{T_0} for the desired $T_0 > 0$ in Equation (2.7).

Now that one has obtained an equicontinuous and uniformly bounded family of solutions $\{h_\epsilon\}$ in $\overline{Q_{T_0}}$, taking its subsequence as $\epsilon \to 0$ allows one to obtain a weak solution h, which satisfies

$$\int_{Q_{T_0}} h\phi_t + \int_{\overline{Q_{T_0}}\backslash(\{h=0\}\cup\{t=0\})} f(h)h_{xxx}\phi_x = 0, \tag{2.12}$$

for all $\phi \in Lip(\overline{Q_{T_0}})$ with $\phi = 0$ near $t = 0$ and $t = T_0$. In fact, this weak solution h is *very* weak in the sense that it even includes a stationary solution with compact support of form $(x-b)^+(c-x)^+$, for $-a < b < c < a$. However, despite its "weakness", the solution naturally satisfies $h \in_{x,t}^{1/2,1/8} (\overline{Q_{T_0}})$ as well as assures conditions:

$$h_t, h_x, h_{xx}, h_{xxx}, h_{xxxx} \in C(\overline{Q_{T_0}}\backslash\{h = 0\} \cup \{t = 0\}). \tag{2.13}$$

Next, we describe the general framework for proving the nonnegativity of the weak solution given that the initial condition $h_0 \geq 0$ and $h_0 \in H^1(\Omega)$. The procedure is described in detail

in Section 4 of the work [BF90]. Bernis & Friedman introduced the following function $G_\epsilon(s)$ by setting

$$g_\epsilon(s) = -\int_s^A \frac{dr}{f(r)+\epsilon}, \quad G_\epsilon(s) = -\int_s^A g_\epsilon(r)dr, \tag{2.14}$$

for $A > \max|h_\epsilon|$ for all small ϵ. Because of how we defined $f(h)$ in equation (2.6), one can already obtain the following useful properties:

$$g_\epsilon(s) \le 0, G_\epsilon(s) \ge 0 \quad \text{if} \quad s \le A. \tag{2.15}$$

In addition, one can analyze the behavior of the limit $G_0(s) = \lim_{\epsilon\to 0} G_\epsilon(s)$,

$$G_0(s) = \begin{cases} A_0 + O(s^{2-n}) & \text{if} \quad 1 < n < 2, \quad A_0 > 0, \\ C_2 \log \frac{1}{s} + O(1) & \text{if} \quad n = 2, \quad C_2 > 0, \\ C_1 s^{2-n} + R(s) & \text{if} \quad n > 2, \end{cases} \tag{2.16}$$

where

$$C_1 > 0, \quad R(s) = \begin{cases} O(s^3 - n) & \text{if} \quad n > 3, \\ O(\log\left(\frac{1}{s}\right)) & \text{if} \quad n = 3, \\ O(1) & \text{if} \quad n < 3. \end{cases} \tag{2.17}$$

At first glance, it might be hard to understand why one should consider $G_\epsilon(s)$. Equation (2.4) becomes degenerate as $|h| \to 0$, which will make the $G_\epsilon(s)$ extremely large. However, this is exactly why it is important to consider $G_\epsilon(s)$; bounding $G_\epsilon(s)$ would imply $|h| \not\to 0$. This intuition turns out to be correct. Bernis & Friedman multiplied equation (2.7) by $g_\epsilon(h_\epsilon)$ and integrated over Q_T, for $0 < T < T_0$, to obtain

$$\int_\Omega G_\epsilon(h_\epsilon(x,T)) + \int_{Q_T} h_{\epsilon,xx}^2 = \int_\Omega G_\epsilon(h_{0\epsilon}(x)). \tag{2.18}$$

This allows one to have an upper bound on $\int_\Omega G_\epsilon(h_\epsilon(x,T))$ over any time T by restricting initial condition $h_{0\epsilon}(x)$. For example, one can let

$$\int_\Omega G_\epsilon(h_{0\epsilon}(x)) \le C, \quad \text{where} \quad C \quad \text{is independent of small } \epsilon. \tag{2.19}$$

At this point, one observes that $h \geq 0$ holds as $\epsilon \to 0$ due to uniform convergence of family of Hölder continuous functions. Otherwise, equation (2.18) would be contradicted.

We emphasize that Bernis & Friedman proved the uniqueness and the strict positivity of the solution $h(x,t)$ in Q_{T_0} for $n > 4$, in addition to the nonnegativity result for $n > 1$. Later we note that the result was improved by Bertozzi et al. [BBD94] as the authors showed the positivity of weak solutions for $n > 3.5$. The work of Bernis & Friedman has inspired many mathematicians to study higher-order parabolic equations. In particular, two notable papers were followed by Berttozi & Pugh. The first article [BP96] explores properties of weak solutions of

$$h_t + (f(h)h_{xxx})_x = 0, \quad f(h) = |h|^n \quad \text{on } S^1, \tag{2.20}$$

with respect to periodic boundary conditions and initial condition $h(x,0) \geq 0$. Equation (2.20) has several exact solutions.

One important example is a compactly supported source-type solution, which is guaranteed to exist for $0 < n < 3$ [BPW92]. These are solutions of the form

$$h(x,t) = t^{-\alpha}H(\eta), \quad \eta = xt^{-\alpha}, \quad \alpha = 1/(n+4), \tag{2.21}$$

where $H(\eta)$ solves the following ordinary differential equation:

$$H^n(\eta)H^{(3)}(\eta) = \alpha\eta H(\eta). \tag{2.22}$$

These source-type solutions do not exist for $n \geq 3$ because of the structure of equation (2.22). Another important example is a traveling-wave solution of form $h(x,t) = H(x-ct)$. Specifically, for $n < 2$, there exist compactly supported traveling-wave solutions. For $\frac{3}{2} < n < 3$, advancing-front solutions exist and can be solved as

$$h(x,t) = \begin{cases} A(x-ct)^{3/n} & \text{if } x > ct, \\ 0, & \text{otherwise,} \end{cases} \quad \text{for} \quad c = \left(\frac{3}{n} - 2\right)\left(\frac{3}{n} - 1\right)\frac{3A^n}{n}. \tag{2.23}$$

For $n \geq 3$, there are no advancing-front traveling-wave solutions [BKO93].

Bertozzi & Pugh [BP96] further proved the existence of a nonnegative weak solution for all time for $0 < n < 3$. For $0 < n < \frac{3}{8}$, the authors considered weak solutions in a sense of equation (2.12) whereas for $\frac{3}{8} < n < 3$, the authors considered weak solutions in a sense of distribution. In particular, for a test function $\phi \in C_c^\infty((0,T); C^\infty(S^1))$, the weak solutions for $\frac{3}{8} < n \leq 1$ satisfy

$$\int_{Q_T} h\phi_t - \int_{Q_T} f(h)h_{xx}\phi_{xx} - \int_{Q_T} nh^{n-\alpha}\left(\frac{h^\alpha}{\alpha}\right)_x h_{xx}\phi_x = 0 \quad \text{for} \quad 1/2 - s/4 \leq \alpha < n. \tag{2.24}$$

The weak solutions for $1 < n < 2$ satisfy

$$\int_{Q_T} h\phi_t - \int_{Q_T} f(h)h_{xx}\phi_{xx} - \int_{Q_T} f'(h)h_x h_{xx}\phi_x = 0. \tag{2.25}$$

The weak solutions for $n = 2$ satisfy

$$\begin{aligned} &\int_{Q_T} h\phi_t + \frac{1}{\alpha}\int_{Q_T} h^{1-\alpha}\left(\frac{h^\alpha}{\alpha}\right)_x h_x^2\phi_x + \frac{3}{2}\int_{Q_T} f'(h)h_x^2\phi_{xx} + \int_{Q_T} f(h)h_x\phi_{xxx} = 0 \\ &\quad \text{for} \quad r/4 + 1/2 < \alpha < 1, \quad 0 < r < 1. \end{aligned} \tag{2.26}$$

The weak solutions for $2 < n < 3$ satisfy

$$\begin{aligned} &\int_{Q_T} h\phi_t + \frac{3}{2}\int_{Q_T} f'(h)h_x^2\phi_{xx} + \frac{1}{2}\int_{Q_T} f''(h)h_x^3\phi_x + \int_{Q_T} f(h)h_x\phi_{xxx} = 0 \\ &\quad \text{for} \quad 0 < r < 1, \ 0 < 2 + r - n < 1. \end{aligned} \tag{2.27}$$

In all four cases, $s < \min(2 - n, 1/2)$ and $Q_T = S^1 \times (0,T)$. Bertozzi & Pugh also provided detailed results on regularities in Section 2–4. The existence and regularity proofs followed the general framework suggested by Bernis & Friedman [BF90]. We highlight that their regularity conditions of weak solutions for $0 < n < 3$ are in perfect agreement with the regularity of zero local contact angle for nonnegative source-type solutions. This is meaningful to consider since the boundary of the weak solution's support corresponds to the contact line in the spreading droplet problem.

Finally, Bertozzi & Pugh [BP96] broadened the discussion to the study of the long-time behavior and the existence of a weak solution for $0 < n < \infty$. In particular, the authors

proved an additional result for $0 < n < 3$, which is the physically meaningful case for lubrication approximation for thin films. The proof states that there exist constants $A, c > 0$ such that

$$\|h(x,t) - \overline{h}\|_{L^\infty(S^1)} \leq Ae^{-ct}, \tag{2.28}$$

for $\overline{h} = \frac{1}{|S^1|}\int_{S^1} h_0(x)dx$ and initial condition $h_0 \geq 0, h_0 \in H^1(S^1)$. Using this fact, the authors concluded that there exists a weak solution that becomes strong in finite time (after all $t > T^*$ for some $T^* > 0$) as long as h_0 is not identically zero. It is also implied that the solution asymptotically approaches its mean as $t \to \infty$. The result was shown by using Poincare's inequality, interpolation inequality, and their original inequalities involving entropy.

The second article of Bertozzi & Pugh [BP94] explored the properties of weak solutions of

$$h_t + (h^n h_{xxx} - (h^m)_x)_x = 0 \tag{2.29}$$

to investigate the effect of second-order nonlinear diffusion terms with periodic boundary conditions. Such diffusion terms are introduced in the context of the flow through a porous medium but are also used to describe a cutoff long-range van der Waals interaction. Including a van der Waals term allows one to describe film rupture (in the repulsive case) and the precursor dynamic of thin film (in the attractive case) [Gen85, WD82]. The presence of the van der Waals term has been observed in recent studies that model fiber coating dynamics as well. For example, a diffusion term proportional to $-\frac{A_H}{h^3}$ was used [JFS19, JFS21, DLL19, JSJ20].

By including an additional second-order term from equation (2.20), one can expect competition between the second-order term and the fourth-order term. In the case when $n \geq 3$ and $1 < m < 2$, the leading order asymptotics solution is proportional to $(x-x(t))^{1/(1-m)}$ at the leading edge. This means there are locally advancing traveling-wave solutions and the behavior of the boundary at the support is dominated by the second-order term. For $3/2 < n < 3$ and $1 < m < 2$, the equation is dominated by the term that gives higher regularity. In the case when $n = 3/2$ and $1 < m < 2$, log dependence is expected since the equation is dominated by the fourth-order term.

The presence of the second-order term leads to additional regularity results. In the case when $n \geq 3$ and $1 < m < 2$, the following regularity is guaranteed,

$$\begin{aligned} & h^{\frac{m+1}{2}} \in L^2(0,T;H^2(S^1)), \\ & (h^\gamma)_x \in L^4(Q_T) \quad \text{for all} \quad \gamma \geq \frac{m+1}{4}, \\ & (h_x^{\frac{\alpha+m-1}{2}} \in L^2(Q_T) \quad \text{for all} \quad \alpha \geq \alpha_0 > 0. \end{aligned} \tag{2.30}$$

Similar to the work of Bertozzi & Pugh [BP96], the authors achieved the existence of a nonnegative weak solution in the distributional sense. In particular, for a test function $\phi \in C_c^\infty((0,T);C^\infty(S^1))$ and $f(h) = h^n$, the weak solution for $1 < n < 2$ and $1 < m < 2$ satisfies

$$\int_{Q_T} h\phi_t - \int_{Q_T} f(h)h_{xx}\phi_{xx} - \int_{Q_T} f'(h)h_{xx}h_x\phi_x - \int_{Q_T} (h^m)_x\phi_x = 0. \tag{2.31}$$

The weak solution for $n > 2$ and $1 < m < 2$ satisfies

$$\int_{Q_T} h\phi_t + \frac{3}{2}\int_{Q_T} f'(h)h_x^2\phi_{xx} + \frac{1}{2}\int_{Q_T} f''(h)h_x^3\phi_x + \int_{Q_T} f(h)h_x\phi_{xxx} - \int_{Q_T} (h^m)_x\phi_x = 0. \tag{2.32}$$

Similar to [BP96], the weak solution for $n = 2$ can be derived by modifying the above equation. The nonnegative weak solution also has time t^* after which the solution is guaranteed to be a positive strong solution, converging to the mean as $t \to \infty$. This is because, similar to [BP96] again, equation (2.28) holds.

The second paper of Bertozzi & Pugh [BP94] can be viewed in parallel with the article by Passo et al. [PGS01]. In this paper, the authors considered a fourth-order degenerate parabolic equation with respect to the Neumann boundary conditions,

$$\begin{aligned} & h_t + \nabla \cdot (h^n \nabla \Delta h - h^m \nabla h) = 0, \quad h(x,0) \geq 0, \quad m \in \mathbb{R}, \quad n \in \mathbb{R}^+, \\ & \nabla h \cdot \nu = \nabla \Delta h \cdot \nu = 0 \quad \text{on} \quad \partial\Omega \times \mathbb{R}^+. \end{aligned} \tag{2.33}$$

The paper provided a proof on the existence of a weak solution for equation (2.33) when

$\frac{1}{8} < n < 4, m > -1$. For any test function $\phi \in C_c^\infty(\Omega \times [0,\infty))$, a weak solution h satisfies

$$\int_0^\infty \int_\Omega h\phi_t + \int_\Omega \phi(x,0)h(x,0) + \frac{1}{m+1}\int_0^\infty \int_\Omega h^{m+1}\Delta\phi + \frac{n(n-1)}{2}\int_\mathcal{P} h^{n-2}|\nabla h|^2 \nabla h \nabla\phi$$
$$+ \frac{n}{2}\int_\mathcal{P} h^{n-1}|\nabla h|^2\Delta\phi + \frac{n}{2}\int_\mathcal{P} h^{n-1}D^2\phi\nabla h\nabla h + \int_0^\infty\int_\Omega h^n \nabla h \nabla\Delta\phi = 0. \tag{2.34}$$

Note that the definition above involves $\mathcal{P} = \{h : h(x,t) > 0\}$, similar to the definition in equation (2.12). Still, these solutions satisfy the following entropy estimate:

$$\frac{1}{\alpha(\alpha+1)}\int_\Omega [h^{\alpha+1}(x,t) - h^{\alpha+1}(x,0)] + \int_{\Omega_t} |\nabla h^{\frac{\alpha+m+1}{2}}|^2 + |\nabla h^{\frac{\alpha+n+1}{4}}|^4 + |D^2 h^{\frac{\alpha+n+1}{2}}|^2 \le 0,$$
$$\text{for} \quad \alpha \in (1/2 - n, 2 - n)\backslash\{(0,-1)\}. \tag{2.35}$$

The above entropy estimate leads to various regularity properties. Using these regularity properties, Passo et al. [PGS01] estimated the propagation speed of the solutions. The authors proved that solutions have an infinite speed of propagation if $m < 0$ and $0 < m - n + 2 < 1/2$ by showing that solutions with compactly supported initial data are positive in finite time almost everywhere in the domain Ω. On the other hand, the authors showed that the solutions have a finite speed of propagation if $m > 0$ and $1/8 < n < 2$. These investigations further contributed to the understanding of the interplay between the fourth-order term and the second-order term in equation (2.33).

Finally, we must mention the work of Bertozzi et al. [BBD94], as it has served as an inspiration for many mathematicians to investigate singular behaviors of PDEs, particularly those arising from interfacial flows [Ber96b, Ber95b, ZB00, Bra12, ZL99, BBW98, BF03, MBU10, MBH10, JW17, BT07, Egg18]. The study of singular behaviors contributed to the design of robust positivity-preserving numerical methods.

Several other articles established the positivity of weak solutions for lubrication-type equations and investigated the regularity of solutions [Zha09, TW18, Mic15, FG18]. Some of them focused on proving the existence of a Cauchy solution [Gru05, Gru01, AK09, BF90].

These articles are mathematically interesting and can be utilized to prove the existence of a numerical solution.

Grün [Gru01] investigate Bernis' interpolation inequality [Ber96a] arising from the lubrication equation (2.40) with the Neuman Boundary conditions (2.33),

$$\int_\Omega h^{n-4}|\nabla h|^6 + \int_\Omega h^{n-2}|\nabla h|^2|D^2h|^2 \leq C\int_\Omega h^n|\nabla\Delta h|^2 \quad \text{for} \quad h \in H^2(\Omega).$$

The author established a generalized estimate in multiple spatial dimensions ($\mathbb{R}^d, d \leq 6$) under a few additional assumptions. While there were many results describing the regularity of strong solutions, which is important for proving the positivity of solutions, extending these results to multiple dimensions has remained challenging. In one dimension, the proof of the estimate relies on the Sobolev embedding theorem. However, generalizing the regularity analysis for the case $2 \leq n < 3$ to multiple dimensions is particularly important, as these cases are physically relevant. Moreover, for the fiber coating application, investigating the regularity of solutions in multiple dimensions is crucial in order to extend the numerical method accordingly.

The work of Grün [Gru05] can be viewed in parallel with the article [Gru01]. Grün [Gru05] considered the thin film equation in the multi-dimensional setting and solved the Cauchy problem in the parameter regimen $n \in [2, 3)$, where n could be understood as the term controlling the slippage of the solid-liquid interface. The author's new interpolation inequalities were applied to the energy estimate, allowing control of third-order derivatives of appropriate powers of solutions. The article also provided a proof of the existence of a regular, strong solution to the Cauchy problem with compactly supported initial data. Some key integral estimates were established to provide further insight into the qualitative behavior of solutions, like the finite speed of propagation or occurrence of a waiting time phenomenon.

Lastly, if equation (2.41) is not guaranteed to be positive all the time, the work of Poulios et al. [PVK18] will become useful. The authors introduced a method to enforce the nonnegativity of solutions for lubrication-type equations by incorporating an additional flow

term. We also expect the following articles to be useful [AB20, GW03] since these articles introduced Lyapunov functionals for lubrication-type of thin-film equations. These functionals can be used to establish entropy or other types of estimates on analytical solutions.

2.1.3 Prior work on positivity-preserving numerical methods for fourth-order nonlinear parabolic PDEs

In this section, we review the articles that designed positivity-preserving schemes for solving fourth-order nonlinear parabolic PDEs other than lubrication-type equations. Although these equations are not specifically used to model viscous fluid, the articles introduced various transformation techniques to prove the positivity of numerical solutions of higher-order parabolic equations. There are also a few similarities between these equations and lubrication-type equations, such as the existence of a non-decreasing entropy. While the techniques introduced in this section are not directly applied to the problems addressed in the thesis, the work of these authors could be utilized for other lubrication-type problems with some modifications.

The main focus of the discussion is on positivity-preserving numerical methods for fourth-order nonlinear parabolic systems that arise in modeling quantum semiconductor devices [JP01, JP03]. There are various models at different scales, ranging from microscopic to macroscopic [JP01]. Two notable macroscopic-level models are the quantum hydrodynamics model (QHD) and the quantum drift-diffusion model (QDD), derived by asymptotic analysis. The QHD describes the behavior of electron density flow in quantum semiconductor devices in a "fluid-like" structure. The model was developed by adding $O(\hbar^2)$ correction to the classical hydrodynamic equations. While the primary application of QHD equations is in quantum semiconductor devices, it has also been studied in the context of fluid models of the nucleus, superconductivity, and superfluidity [Gar94]. In the limit where relaxation time

approaches zero, a coupled QHD system can be written by the following single equation,

$$n_t = \nabla \cdot \left(n \nabla \left(-\varepsilon^2 \frac{\Delta \sqrt{n}}{\sqrt{n}} + \theta \log(n) + V \right) \right) \tag{2.36}$$

on a bounded domain Ω [JP01]. Here, n represents the electron density, ε represents a scaled Planck constant, θ represents a scaled temperature, and V represents the electrostatic potential. Positivity-preserving numerical methods are desired for the QHD equations since the electron density $n(x,t)$ must remain positive.

Jüngel & Pinnau [JP01] introduced a positivity-preserving numerical scheme for equation (2.36). The authors derived an implicit semi-discretization using the backward Euler method after writing equation (2.36) into a system of equations. The authors proved the existence and strict positivity of discretized solutions using an exponential transformation of variable, $\rho = \sqrt{n} = e^u$. In addition, the authors proved a stability estimate and the convergence of the numerical solution, which is essentially a consequence of the boundedness of entropy. For an extensive review of QHD, we refer the readers to Gardner [Gar94] and Jüngel & Pinnau [JP01].

QDD, on the other hand, is a drift-diffusion model with a quantum correction term [Moc83]. One can view QDD as the isothermal QHD in the limit of zero relaxation time [Pin00]. Several articles investigated positivity-preserving numerical methods of QDD, including works by [DMM10, MO17, Pin02, BEJ14, Pin01, CJT03]. Some of them specifically focused on positivity-preserving numerical methods for the Derida-Lebowitz-Speer-Spohn (DLSS) equation [DMM10, MO17], which is a simplification of QDD in the limit of zero temperature and vanishing electric fields [JM08]. The DLSS equation [DLS91] was initially discussed in analyzing interface fluctuations in a two-dimensional spin system commonly referred to as the Toom model. However, it gained significant attention and has been extensively studied due to its simpler form [DMR05, Jun09]. The DLSS equation can be written as

$$n_t + 2 \left[n \left(\frac{(\sqrt{n})_{xx}}{\sqrt{n}} \right)_x \right]_x = 0 \quad \text{on} \quad \Omega_T. \tag{2.37}$$

In this case, $n(x,t)$ is the electron density again, which must remain positive.

Düring et al. [DMM10] developed a fully practical numerical scheme for the DLSS equation that preserves the conservation of mass and nonnegativity of the numerical solutions. Other numerical methods for maintaining the positivity of a DLSS solution were introduced as well [Jun09, Lau05, DMR05]. For a comprehensive review of the topic, we refer the readers to the article by Pinnau [Pin02]. In this article, the author covered several topics, such as the existence and uniqueness of analytical solutions and asymptotic limits.

2.1.4 Prior work on the application of positivity-preserving numerical methods for parabolic PDEs

In this section, we present a collection of articles inspired by positivity-preserving numerical methods. These articles either directly applied positivity numerical methods to simulations or incorporated ideas from positivity-preserving numerical methods, such as utilizing entropy or energy estimation techniques. Some of these articles also established connections to the field of lubrication theory. We present the application of positivity-preserving methods through various examples in different scenarios, from and beyond the field lubrication theory.

One apparent application of the positivity-preserving numerical method is in the context of describing thin film dynamics. For example, the spreading of droplets remains an interesting topic within the scientific community due to its versatile applications [Gen85, ODB97]. However, there are challenges due to the presence of a fourth-order term, which can make the numerical method extremely stiff. Additionally, describing the dynamics near the wetting line requires the need for numerical grid refinement. Gaskell et al. [GJS04] presented an efficient and fully implicit time-adaptive multigrid method for simulating droplet spreading on heterogeneous substrates. The authors utilized Zhornitskaya & Bertozzi's positivity-preserving numerical method [ZB00] to develop their numerical approach. The validity of the method was demonstrated by successfully reproducing a wide range of analytical and numerical results from previous studies, as well as by generating new simulations regarding droplet motion on heterogeneous substrates. Alleborn & Raszillier [AR04] also presented a model for the

spreading and sorption of a droplet on a thick porous substrate. The model was derived using the lubrication approximation, characterizing the droplet profile above and inside the porous substrate. The model incorporated the influence of the precursor film as well as disjoining pressures, which play crucial roles in wetting and dewetting phenomena. The proposed model successfully captured the dynamics of spreading and sorption for axisymmetric droplets as well as more complex three-dimensional sorption scenarios.

Modeling thin liquid film on an inclined heated surface is another example of application. Ajaev et al. [AGS10] introduced a model that captures the dynamics of an evaporating thin liquid film on such a surface. The model incorporated disjoining pressure effect, as thin fluids are strongly influenced by it. The objective of the study was to investigate the relationship between the static and dynamic contact angles and various factors, including wetting properties, the rate of evaporation, and the effects of heating. The results demonstrated that the static contact angle increases as the heater temperature rises while the dynamic contact angle increases as the evaporative mass loss increases. The authors conducted numerical simulations using Zhornitskaya & Bertozzi's [ZB00] positivity-preserving numerical method to accurately simulate these intricate phenomena. The simulations yielded valuable information regarding the profiles of the evaporating liquid film near the moving contact line, with particular emphasis on different forms of disjoining pressure.

Another application of thin films arises in biological contexts. Maki et al. [MBH10, MBU10] modeled a tear film of a human on a stationary eye-shaped domain after blinking. The model was created using lubrication approximation and the effects of viscosity, surface tension, gravity, and boundary conditions were considered. As a result, the authors were able to gain insight into the thin-tear-film movement on the entire eye surface. The evolution equation was solved numerically with an overset grid method on an eye-shaped (curved) domain constructed from measured eyelid data.

In simulating several models discussed above, such as the model of the tear film on a human eye geometry [MBD08], the model of droplet spreading in multiple spatial dimensions [GJS04]

or vapor bubbles between two plates [AHM02], there is a need for positivity-preserving numerical methods that can be applied to more general geometries. Greer et al. [GBS06] also acknowledged this need. Greer et al. [GBS06] developed a numerical method for solving fourth-order PDEs on general geometries, including the Cahn–Hilliard equation and a lubrication model for curved surfaces. The authors extended a previously introduced method for solving PDEs on implicit surfaces numerically. This was done by representing the surface on which the PDE is defined as the level set of a smooth function and rewriting the relevant equations in terms of Euclidean coordinates and derivatives of the level set function [BCO01]. The PDE was computed using simple finite differences, which is challenging to apply on surfaces with complex geometries. The method utilized convexity splitting, ADI method, and iterative solvers to overcome challenges arising from higher-order degenerate PDEs. However, it is important to note that the resulting numerical method was not positivity-preserving. Given the application of these equations in thin film and mixed fluids, it would be valuable to design a positivity-preserving numerical method that works on various geometries.

As mentioned before, the Cahn-Hilliard system is a well-known degenerate fourth-order system of PDEs that models phase separation and coarsening phenomena of multi-components. Because the model deals with the concentration of fluids, the components have to be nonnegative. Barrett et al. [BBG01] developed and analyzed a finite element approximation of the degenerate Cahn-Hilliard system with a degenerate mobility matrix. The numerical method was designed based on a continuous piecewise linear finite element method that discretizes the fractional concentration of multi-components in space. An implicit Euler method was used to discretize in time. Fortunately, the Cahn-Hilliard system was shown to have an associated entropy that gives H^2 estimates of concentration vector $\mathbf{u}$. The analysis of the method included the stability bounds holding in all space dimensions and the convergence in the case of one space dimension.

Discussions on positivity-preserving numerical methods can also be found in the context of nonlinear cross-diffusion PDE models. In a typical nonlinear cross-diffusion system, there

are two second-order parabolic nonlinear PDEs, where each equation describes the population density of a species. Again, the population density needs to remain positive. Barrett & Blowey [BB04] presented a fully discrete finite element approximation for a nonlinear cross-diffusion equation that describes the interaction of two species in a population. The method was derived to be consistent with a discrete analog of an entropy estimate. The authors demonstrated the well-posedness of the approximation and proved convergence in space dimensions $d \leq 3$. The existence of a discrete solution was established by exploiting the entropy estimate. Furthermore, the authors provided numerical experiments in one space dimension that are consistent with the theoretical results. Bruna & Chapman [BC12] introduced a model that describes inter-species competition using a stochastic diffusion approach. Each species is represented as a finite-size particle and these particles interact with each other while undergoing Brownian motion. The authors derived two kinds of models; a continuum PDE model describing the macroscopic interaction of the species and an N-coupled system of stochastic differential equations describing the microscopic interaction of the species. The system of two species resulted in a nonlinear cross-diffusion system describing the population density of each species. The validity of their approach was supported by comparing a numerical simulation of the continuum model with a stochastic simulation of a discrete particle-based model.

Another intriguing application is in image denoising [BG04]. Bertozzi & Greer discussed the connection between lubrication-type equations and image-denoising equations. The latter is a fourth-order nonlinear diffusion equation motivated by Tumblin and Turk's "low-curvature image simplifiers",

$$h_t = -\nabla \cdot (g(\Delta h)\nabla \Delta h) + \lambda(f - h), \tag{2.38}$$

where $g(s) = k^2/(k^2 + s^2)$ is a curvature threshold and λ is a fidelity term. This type of equation has been studied in the context of image denoising and image segmentation for one- and two-dimensional images. The authors derived pointwise estimates for Δh which allowed them to prove the global regularity of smooth solutions in one dimension. For two-dimensional

cases, the authors presented a constraint for finite-time singularities depending on the initial data. Their estimates were derived by making a key change of variable, namely $\tan w = \Delta h$, which was first observed in [GB04]. After applying the change of variable, equation (2.38) becomes

$$w_t + \cos^2(w)\Delta^2 w = 0, \tag{2.39}$$

which is similar to the classical lubrication equation (2.40). Thus, these connections were used to design an effective finite difference method that satisfies the discrete equivalent of a priori bounds on smoothness in one and two dimensions.

The application of positivity-preserving numerical methods is not limited to the examples above. It can be applied in various other domains such as modeling tumor growth [KS08, WLF08, CGR17] and atmospheric circulation [DD07], where nonlinear, and many times higher order parabolic PDEs are commonly used. Recent advancements in biomathematics and biofluids also demonstrate a noteworthy potential for the application of these numerical methods. For instance, Klapper and Dockery [KD06] developed equations that provide a qualitative constitutive description of biofilm by incorporating the effects of viscoelasticity and cohesion using a polymer-solvent theory.

2.2 Fundamentals of positive-preserving numerical methods

In this section, we discuss the necessary ingredients to design a positivity-preserving numerical scheme. We specifically consider the work of Zhornitskaya & Bertozzi [ZB00], which was an inspiration for the new work in the thesis. The general problem the authors consider is

$$h_t + \nabla \cdot (f(h)\nabla\Delta h) = 0, \quad \text{where} \quad f(h) \sim h^n \quad \text{as} \quad h \to 0, \tag{2.40}$$

which is the most basic form of the lubrication equation. Some distinguished properties of Equation (2.40) are that this fourth-order equation is degenerate and diffusive, guaranteeing smoothness whenever the solution is positive. Despite such a delightful property on regularity,

Equation (2.40) induces numerical instability and "false" (negative) singularities as $h \to 0$ [BBD94]. While preserving positivity, it is desirable for the equation to satisfy fundamental physical properties such as conservation of mass, surface energy dissipation, and nonlinear entropy dissipation.

The above equation (2.40) if written in 1-dimension possesses many similarities with the following problem:

$$\begin{aligned}
&\partial_t \left(h + \frac{\alpha}{2}h^2\right) + \partial_x \left[\mathcal{M}(h)\left(1 - \partial_x\left[Z_{FS}(h) - \partial_x^2 h\right]\right)\right] = 0,\\
&\mathcal{M}(h) = \frac{h^3\phi(\alpha h)}{3\phi(\alpha)}, \quad \phi(X) = \frac{3}{16X^3}[(1+X)^4(4\log(1+X) - 3) + 4(1+X)^2 - 1], \quad (2.41)\\
&\mathcal{Z}_{FS}(h) = -\frac{A_H}{h^3} + \frac{\alpha}{\eta(1+\alpha h)} \quad \text{for} \quad \alpha, A_H, \eta > 0.
\end{aligned}$$

Aside from $\partial_t \left(h + \frac{\alpha}{2}h^2\right)$ term, one can observe that the mobility term $\mathcal{M}(h) \sim h^3$ is very similar to $f(h)$ in Equation (2.40) although $\mathcal{M}(h)$ depends on α for Equation (2.41). We can also view the $\nabla\Delta h$ term in Equation (2.40), which is written as h_{xxx} in the case of one dimension, is being replaced by $\partial_x(\partial_x^2 h)$ in Equation (2.41). One distinct term that adds richness to the intricate behavior to Equation (2.41) is $Z_{FS}(h)$ term, which consists of a destabilizing term $\frac{\alpha}{\eta(1+\alpha h)}$ and a stabilizing term $-\frac{A}{h^3}$.

Notice that $f(h) \sim h^n$ from Equation (2.40) can be discretized based on the following equation:

$$a(s_1, s_2) = \begin{cases} f(s_1) & \text{if } s_1 = s_2 \\ \frac{s_1 - s_2}{G'(s_1) - G'(s_2)} & \text{if } s_1 \neq s_2 \end{cases}, \quad \text{where } G''(s) = \frac{1}{f(s)}. \tag{2.42}$$

Eqaution (2.42) can be used to formulate various finite difference methods using implicit or semi-implicit time stepping.

2.3 Numerical examples

2.3.1 Regularizing a singular PDE

In this section, we reproduce an example from Section 9 of Zhornitskaya & Bertozzi's work [ZB00]. The authors considered a weak solution of

$$h_t + \partial_x(f(h)\partial_x^3 h) = 0, \quad f(h) = h^{1/2}, \tag{2.43}$$

where the fractional power of $1/2$ was chosen because the numerical solution develops a singularity in finite time [Ber95b]. The authors imposed the following positive initial conditions,

$$h_0(x) = 0.8 - \cos(\pi x) + 0.25\cos(2\pi x), \quad x \in [0, 1]. \tag{2.44}$$

To calculate solutions past the singularity, Zhornitskaya & Bertozzi introduced the following regularized problem,

$$h_{\epsilon t} + \partial_x(f_\epsilon(h_\epsilon)\partial_x^3 h_\epsilon) = 0, \;\; f_\epsilon(h_\epsilon) = \frac{h_\epsilon^4 f(h_\epsilon)}{\epsilon f(h_\epsilon) + h_\epsilon^4}, \;\; f(h) = h^{1/2}. \tag{2.45}$$

The regularized problem described in Equation (2.45) ensures that the analytical solution of the equation remains positive for all $\epsilon > 0$, as $f_\epsilon(h_\epsilon) \sim h_\epsilon^4/\epsilon$ as $h_\epsilon \to 0$ [BF90, BBD94]. We employ a numerical scheme that forms the basis of the generic scheme (GS) and the entropy dissipating scheme (EDS) presented in [ZB00]. The scheme is given by

$$\frac{u_i^{k+1} - u_i^k}{\Delta t} + (a(u_{i-1}^{k+1}, u_i^{k+1})u_{i,\bar{x}x\bar{x}}^{k+1})_x = 0, \quad i = 1, 2, 3, ...N, \quad k = 1, 2, 3, ...M, \tag{2.46}$$

where i represents the grid index in space and k represents the grid index in time. In Equation (2.46), x and $\bar{x}$ are shorthand notations for forward and backward differences,

$$u_{i,x}^k = \frac{u_{i+1}^k - u_i^k}{\Delta x}, \quad u_{i,\bar{x}}^k = \frac{u_i^k - u_{i-1}^k}{\Delta x}. \tag{2.47}$$

We impose the Neumann boundary condition to the regularized problem (2.45). Central difference approximations are used at the boundary to derive the following conditions:

$$\begin{aligned} &h_{\epsilon x}(0) \implies u_0^k = u_2^k, \quad h_{\epsilon xxx}(0) \implies u_{-1}^k = u_3^k, \\ &h_{\epsilon x}(1) \implies u_{N-1}^k = u_{N+1}^k, \quad h_{\epsilon xxx}(0) \implies u_{N-2}^k = u_{N+2}^k, \\ &\text{for} \quad k = 1, 2, 3, 4...M. \end{aligned} \tag{2.48}$$

For GS, we define

$$a(s_1, s_2) = 0.5(f_\epsilon(s_1) + f_\epsilon(s_2)). \tag{2.49}$$

For EDS, we define

$$a(s_1, s_2) = \begin{cases} f_\epsilon(s_1) & s_1 = s_2 \\ \frac{s_1 - s_2}{G'(s_1) - G'(s_2)} & s_1 \neq s_2 \end{cases}, \quad \text{where } G''(s) = \frac{1}{f_\epsilon(s)}. \tag{2.50}$$

We specifically choose a fully implicit method because Equation (2.46) involves a diffusion term. The backward Euler method is often used to ensure the monotonicity and stability of problems with diffusion [ZB00]. Since Equation (2.46) is nonlinear, we use Newton's method (see Algorithm 1) to solve for the numerical solution at the next time step.

Figures 2.1 to 2.3 depict the reproduced images, illustrating the effectiveness of Zhornitskaya & Bertozzi's positivity-preserving numerical scheme for the lubrication equation with a near singular behavior (2.45). Both Figure 2.1 and Figure 2.2 are simulated with a uniform time and space discretization. An adaptive time stepping method (see Algorithm 3) is used to generate Figure 2.3 on the other hand, to demonstrate that the method (2.46) can be computationally efficiently implemented for a fine grid problem.

Figure 2.1 shows the numerical solutions obtained by the GS (2.49) with $\epsilon = 10^{-11}, 10^{-13}$, and 10^{-14} using a grid with 128 points on $[0, 1]$. The GS solutions develop finite time singularities for all three cases, as depicted in Figure 2.1, consistent with Zhornitskaya & Bertozzi's observation [ZB00]. In Figure 2.2, the numerical solutions obtained by the EDS (2.50) with $\epsilon = 10^{-11}, 10^{-13}$, and 10^{-14} using a grid with 128 points on $[0, 1]$ until

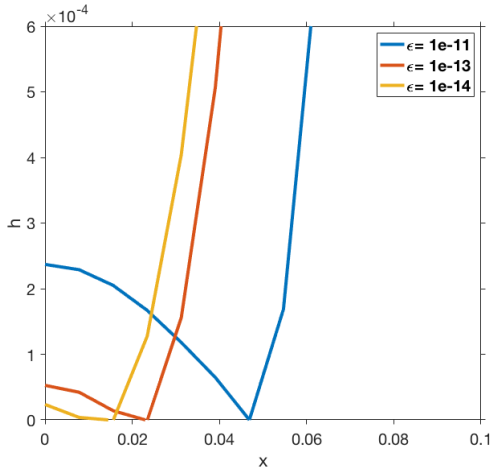

Figure 2.1: Numerical solutions of Equation (2.45) using the generic scheme (GS), specifically implementing Equation (2.46) with Equation (2.49). The computation is terminated earlier than $t = 0.001$ due to the occurrence of a finite time singularity. Simulations are conducted on a coarse grid (128 grid points on $[0, 1]$) with a uniform time step $\Delta t = 10^{-7}$. For each time step, Newton's method (see Algorithm 1) is employed to calculate the solution at the next time step, with a tolerance value of 10^{-8}. At $\epsilon = 10^{-11}, 10^{-13}$, and 10^{-14}, the GS exhibits a numerical singularity at the corresponding time $t = 0.0008$, $t = 0.00074$, and $t = 0.00073$. Figure 2.1 shows the reproduced results from Figure 9.2 of Zhornitskaya & Bertozzi's work [ZB00], obtained by implementing our code.

$t = 0.001$ are shown. Unlike the GS, the EDS does not introduce any singularity until the terminating time $t = 0.001$. Figure 2.3 presents the numerical solutions obtained by the EDS (2.50) with $\epsilon = 10^{-11}, 10^{-13}$, and 10^{-14} using a grid with 1028 points on $[0, 1]$ until $t = 0.001$. Again, the EDS does not introduce any singularity until the terminating time $t = 0.001$. Figure 2.3 exhibits similar solution profiles to Figure 2.2, illustrating the effective capture of solutions by EDS on a coarse mesh. Figure 2.3 shows the computational results obtained by the EDS (2.50) with $\epsilon = 10^{-11}, 10^{-13}$, and 10^{-14} using a grid with 1028 points on $[0, 1]$ until $t = 0.001$. The regenerated EDS does not introduce any singularity until the terminating time $t = 0.001$. Figure 2.3 is similar to 2.2, illustrating that the coarse grid

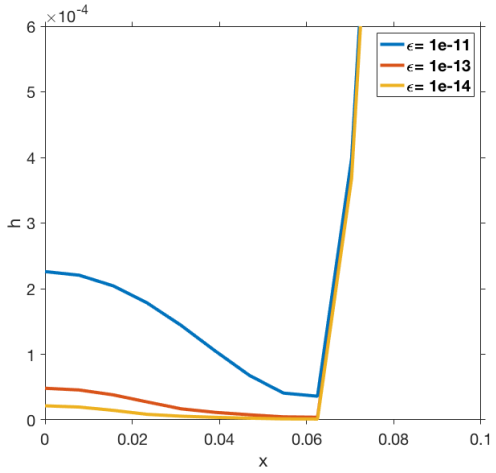

Figure 2.2: Numerical solutions of Equation (2.45) using the entropy dissipating scheme (EDS), specifically implementing Equation (2.46) with Equation (2.50). The computation is successfully continued until $t = 0.001$ without encountering any finite time singularity for $\epsilon = 10^{-11}, 10^{-13}$, and 10^{-14}. Simulations are conducted on a coarse grid (128 grid points on $[0, 1]$) with a uniform time step $\Delta t = 10^{-7}$. The solutions obtained from the coarse grid exhibit a good agreement with the solutions generated from a fine grid (see Figure 2.3). For each time step, Newton's method (see Algorithm 1) is employed to calculate the solution at the next time step, with a tolerance value of 10^{-8}. Figure 2.2 shows the reproduced results from Figure 9.3 of Zhornitskaya & Bertozzi's work [ZB00], obtained by implementing our code.

captures the solution profile well.

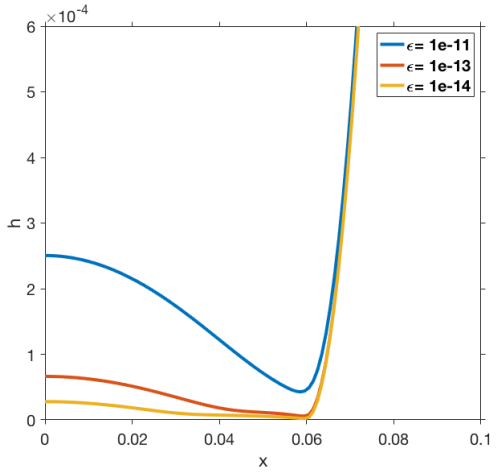

Figure 2.3: Numerical solutions of Equation (2.45) using the entropy dissipating scheme (EDS), specifically implementing Equation (2.46) with Equation (2.50). The computation is successfully continued until $t = 0.001$ without encountering any finite time singularity for $\epsilon = 10^{-11}, 10^{-13}$, and 10^{-14}. Simulations are conducted on a fine grid (1024 grid points on $[0, 1]$) with an adaptive time stepping method (see Algorithm 3) with $\log_{10}(\min \Delta t) = -7$. For each time step, Newton's method (see Algorithm 1) is employed to calculate the solution at the next time step, with a tolerance value of 10^{-14}. Figure 2.3 shows the reproduced results from Figure 9.4 of Zhornitskaya & Bertozzi's work [ZB00], obtained by implementing our code.

2.3.2 Dewetting liquid film on a solid substrate

In this section, we reproduce an example from Section 7 of Bertozzi et al.'s work [BGW01]. The example consists of the following lubrication-type equations with a nonlinear pressure p,

$$\begin{aligned} &h_t + (M(h)p_x)_x = 0 \quad \text{in} \quad (0, 20) \times (0, T) \subset \mathbb{R}^2, \\ &p = h_{xx} - \frac{1}{h^3} + \frac{\epsilon}{h^4}, \quad M(h) = h^3, \\ &p_x = h_x = 0 \quad \text{at} \quad x = 0 \text{ and } x = 20. \end{aligned} \tag{2.51}$$

In addition to the contribution from linearized surface tension represented by h_{xx}, the term p incorporates the effects of $-1/h^3$ and ϵ/h^4. These terms exemplify the combined influence of

the destabilizing long-range attractive force and the stabilizing short-range effect of Born repulsion. Oron & Bankoff [OB99] employed these terms to model the dewetting of a thin film on a layered solid substrate. Equation (2.51) is solved with the following initial conditions,

$$h_0(x) = 1 + 0.005\sin(6(x-13)^2) \quad \text{on} \quad x \in [0, 20]. \tag{2.52}$$

As the distance from $x = 13$ increases, the initial data exhibits increasing oscillations in a symmetric fashion. This type of initial data can generate complex patterns of droplets, which can display high sensitivity to the underlying structure of $h_0(x)$. Consequently, a robust numerical method is required to effectively simulate this example.

Bertozzi et al. [BGW01] conducted a simulation of Equation (2.51) with two different values of ϵ, specifically $\epsilon = 0.01$ and $\epsilon = 0.1$. In our study, we choose $\epsilon = 0.1$ to generate Figure 2.4. The choice of the ϵ determines the magnitude of the contribution from short-range repulsive forces. As ϵ approaches zero, the stabilizing effect on the thin film decreases, resulting in a slower coarsening process where droplets gradually merge into a single droplet. In Figure 2.4, it can be observed that initially separated droplets resulting from dewetting gradually merge into a series of droplets, eventually coalescing into a large droplet over a period. At approximately $t \approx 300116$, a simulation with $\epsilon = 0.1$ exhibits the formation of a single large droplet, which is comparable to the result achieved by Bertozzi et al. around $t \approx 6.125 \times 10^7$ using a smaller value of $\epsilon = 0.01$. Due to the complex nature of the dewetting dynamics at the initial stage, a robust numerical method is essential for accurate simulation. The numerical method employed for this simulation is presented in Section 2.4.

2.4 Positivity-preserving numerical method for a thin film model with nonlinear second order pressure

In this section, we present a finite difference method employed in Section 2.3.2 to generate Figure 2.4. We utilized a specific instance of the finite element method proposed by Grün

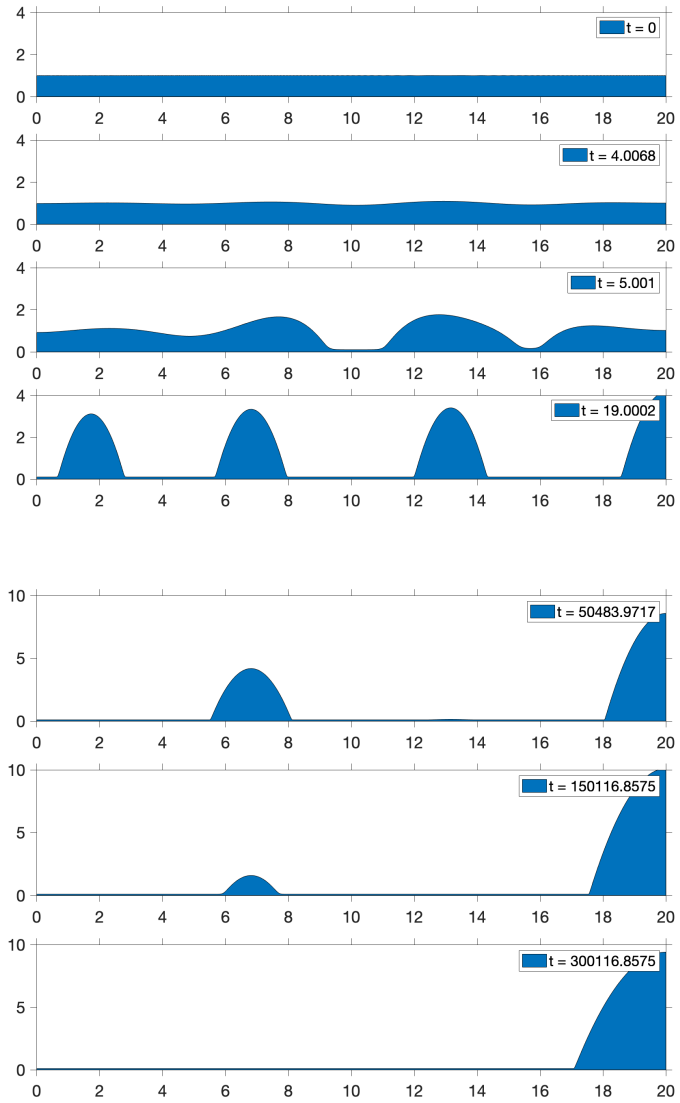

Figure 2.4: Numerical solutions of Equation (2.51) using the method described in Equation (2.57). $a(s_1, s_2)$ is defined as Equation (2.42) with $f(s) = \mathcal{M}(s) = s^3$ in this particular example. The computation is performed on a fine grid (4000 grids on $[0, 20]$) with an adaptive time stepping method (see Algorithm 3). Newton's method (see Algorithm 1) is employed for each time step with a tolerance of 10^{-7}. The simulation was executed on a MacBook Pro 13 inch (2020) with Apple M1 chip and 16GB RAM, taking 40 seconds. Figure 2.4 is the reproduced results of Figure 10 in Bertozzi et al.'s work [BGW01].

& Rumpf [GR01], which is subsequently formulated as a finite difference method. Finite element methods are advantageous when dealing with complex grid structures, such as local mesh refinement for resolving features near moving contact lines [ZB00, DK02]. On the other hand, finite difference methods are generally easier to implement in practice.

Zhornitskaya & Bertozzi [ZB00] proposed a method to reformulate the finite element method into a simple finite difference method. We summarize the procedure and derive the resulting numerical method. Suppose we have the following PDE that describes the dynamics of a thin film under the effect of nonlinear generalized pressure,

$$\begin{aligned} &h_t + \nabla \cdot (\mathcal{M}(h)\nabla(\Delta h - W'(h))) = 0 \ \text{ on } \ \Omega \times (0,T) \subset \mathbb{R}^3 \quad \text{or} \quad \mathbb{R}^4, \\ &\frac{\partial}{\partial \nu} h = \frac{\partial}{\partial \nu} \Delta h = 0 \ \text{ on } \ \partial\Omega \times (0,T), \\ &h(0,x) = h_0(x) \quad \text{in} \quad \Omega. \end{aligned} \tag{2.53}$$

In many cases, the energy $W \in C^2(\mathbb{R};\mathbb{R}^+)$ can be decomposed into a sum $W(h) = W_+(h) + W_-(h)$, where $W_+ \in C^2(\mathbb{R};\mathbb{R}^+)$ is a convex nonnegative function, and $W_- \in C^2(\mathbb{R};\mathbb{R}^+)$ is a concave function. Such splitting may not be unique, but it is useful in designing stable numerical methods. Discretizing the convex term implicitly and the concave term implicitly results in an energy stable method [Eyr98]. The main advantage of the convexity splitting method is that the convex term can often be chosen to be purely quadratic, with a first variation that is linear, so the numerical inversion becomes easier. This results in an efficient method that is often unconditionally or very weakly conditionally gradient stable.

Grün & Rumpf formulated the following finite element method that preserves the nonnegativity of a discrete solution [GR01],

$$\begin{aligned} &\left(\frac{U^{k+1} - U^k}{\Delta t}, \Theta\right)_h + (M(U^{k+1})\nabla P^{k+1}, \nabla\Theta) = 0, \\ &(\nabla U^{k+1}, \nabla\Psi) + (W'_+(U^{k+1}), \Psi)_h + (W'_-(U^k), \Psi)_h = (P^{k+1}, \Psi)_h. \end{aligned} \tag{2.54}$$

Here, we denote (η_1, η_2) as the standard inner product in L^2, and V^h as a linear finite element space in $H^{1,2}(\Omega)$. A basis of V^h is given by $\phi_j(x)$ satisfying $\phi_j(x_i) = \delta_{ij}$. $\mathcal{I}_h(u) =$

$\sum_{j\in J} u(x_j)\phi_j$, so that discrete inner product can be defined as $(\Theta,\Psi)_h := \int_\Omega \mathcal{I}_h(\Theta\Psi)$. The discrete mobility M is defined as the limit of $M_\sigma(U)$ as σ approaches zero, where M_σ is defined element-wise as

$$M_\sigma(U)|_E = \begin{cases} m_\sigma(U_1) & \text{if} \quad U_1 = U_2 \geq 0, \\ \left(\fint 1/m_\sigma(s)ds\right)^{-1} & \text{if} \quad U_1 \neq U_2. \end{cases} \tag{2.55}$$

In the above equation, U_1 and U_2 represent the values of U at the vertices of an element E, $\fint$ denotes the mean value integral, and $m_\sigma(u) = \mathcal{M}(\max(\sigma, u))$. Given an initial condition $(U^0, P^0) \in V^h \times V^h$, for $k = 0, 1, \ldots, N-1$, we seek (U^{k+1}, P^{k+1}) such that Equation (2.54) is satisfied for all $(\Theta, \Psi) \in V^h \times V^h$.

The above finite element method can be formulated as a finite difference scheme in one spatial dimension by choosing a proper basis function $\phi_j(x)$. We consider the following standard piecewise linear basis

$$\phi_j(x) = \begin{cases} \frac{x - x_{i-1}}{\Delta x} & \text{if} \quad x_{i-1} \leq x \leq x_i, \\ \frac{x_{i+1} - x}{\Delta x} & \text{if} \quad x_i \leq x \leq x_{i+1}. \end{cases} \tag{2.56}$$

Then, for $u_i^0 = h_0(i\Delta x)$ and $i = 1, \ldots N-1$, Equation (2.54) can be written as the following finite difference scheme:

$$\begin{aligned} &\frac{u_i^{k+1} - u_i^k}{\Delta t} + [a(u_{i-1}^{k+1}, u_i^{k+1}) p_{i,\bar{x}}^{k+1}]_x = 0, \\ &p_i^{k+1} - u_{i,\bar{x}x}^{k+1} + W'_+(u_i^{k+1}) + W'_-(u_i^k) = 0. \end{aligned} \tag{2.57}$$

Here, x and $\overline{x}$ are shorthand notations for forward and backward differences, as defined in Equation (2.47). Note that we use the same definition for $a(s_1, s_2)$ as in EDS (2.50). In the case when $W' = 0$, Equation (2.57) simplifies to Equation (2.46) since $p_i^{k+1} = u_{i,\overline{x}x}^{k+1}$.

CHAPTER 3

Thin liquid film flowing down a vertical fiber

Questions on the coating flow problem, which pertains to applying a thin fluid over a solid, have been posed by scientific communities for a considerable period [WR04, Que99, KRS12c, CM09, JFS19]. Earlier work classified the coating flow problem based on the geometry of the solid onto which the fluid is coated [Que99]. Examples include plate coating [GW22, LL88] (see Figure 3.1), roll coating [Gat45, Tay63], fiber coating [GW22, WT66], and coating of the inside of a tube [Tay60, Bre61]. For instance, Figure 3.1 provides an example of plate coating, depicting water wave patterns on a vertical plate. It illustrates the complex dynamics of falling liquid films at moderate Reynolds numbers. The initial flat-film flow undergoes dynamic transitions leading to the formation of a two-dimensional periodic wave train. Over time, these waves evolve into solitary waves and eventually develop into more complex three-dimensional patterns, as shown in Figure 3.1. Each wave is characterized by a prominent hump with a long, flat tail trailing behind (see Figure 3.2). The front of the hump is steep and is preceded by small ripples. This dynamic phenomenon is commonly observed in both empirical observations [Que90, KC94, JFS19, SZJ17] and theoretical predictions [KC94, CM06, RTG08] during the fiber coating process as well.

Fiber coating has received substantial attention due to its application in engineering. For instance, passing a cold steel wire through polymer [AH97] effectively protects the steel from corrosion. The toughness and strength of carbon fiber can be reinforced by dipping it in epoxy solution [LI94]. Naturally, one might wonder about the impact of different fluids on coating dynamics. What are the parameters that influence the thickness of the fiber coating?

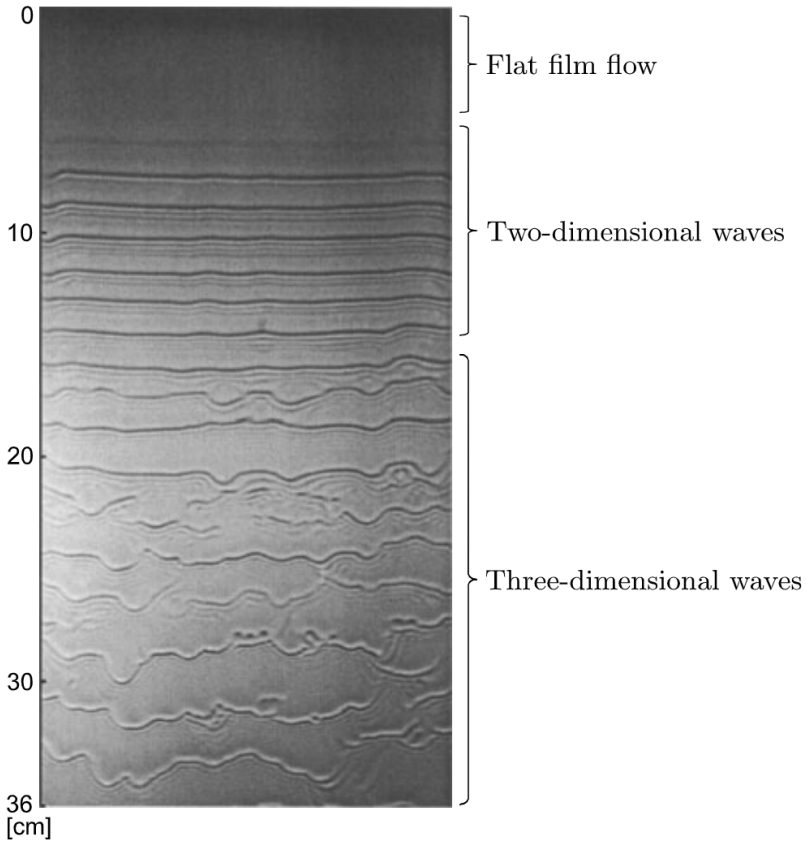

Figure 3.1: Dynamics of water film coating a vertical plate: naturally occurring waves on a water film flowing along a vertical plate at Reynolds number $Re = 33$. The initial flat-film flow undergoes dynamic transitions leading to the formation of two-dimensional and three-dimensional waves. Acknowledgment to Kalliadasis et al. [KRS12b], *Falling Liquid Films*, Introduction, Page 1-19, 2012, Springer Nature. Reproduced with permission from Springer Nature. Used with permission of AlChE journal, from "Three-dimensional wave dynamics on a falling film and associated mass transfer", Park & Nosoko [PN03], Volume 49, Issue 11, 2003; permission conveyed through Copyright Clearance Center, Inc.

How do the fluid properties affect the dynamics or shape of the fiber coating? In this Chapter, we ask these questions in the context of modeling a viscous liquid flowing down a vertical fiber.

3.1 The dynamics of a thin liquid film flowing down a vertical fiber

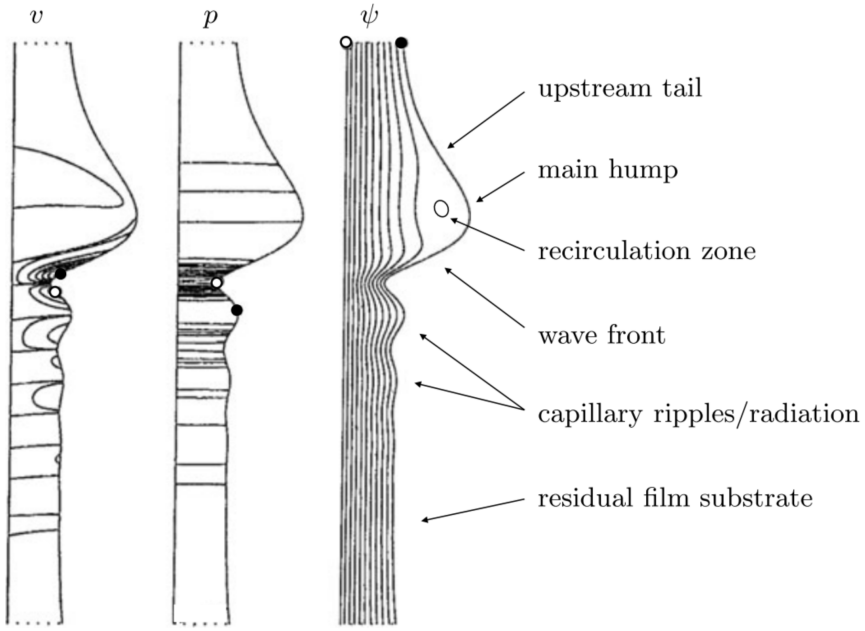

Figure 3.2: Dynamic of a falling film on a contour map, which is very similar to the coating dynamics of a thin fluid flowing down a vertical fiber. v represents the velocity of the fluid in the horizontal direction, p represents pressure, and ψ represents the stream function. Acknowledgment to Kalliadasis et al. [KRS12a], *Falling Liquid Films*, Boundary Layer Approximation, Page 65-93, 2012, Springer Nature. Reproduced with permission from Springer Nature. Reprinted from Salamon et al. [SAB94], with the permission of AIP Publishing.

A thin liquid film flowing down a fiber was first introduced from the context of withdrawing fibers from reservoirs [Que99, GW22, SGM02]. The coating flow is unstable and breaks up into axisymmetric droplets or finite-amplitude interfacial waves despite low inertial effects [KDB01, Que90]. For example, Figure 3.2 depicts a falling film dynamic that is very similar to the coating flow dynamic. The intricate dynamics are characterized by an upstream tail, a main hump, a wavefront, and subsequent capillary ripples. This type of instability is well-known and dates back to the 1870s when Lord Rayleigh discovered that the capillary

force of liquids causes fluid jet instability [Lor78]. He discovered that unstable liquid film breaks up into droplets for $\mathcal{L} > 2\pi\mathcal{R}$ for the axial length scale $\mathcal{L}$ and the radius of a fiber scale $\mathcal{R}$ [Lor78, KDB01]. The mechanism for the fiber coating is very similar. As the liquid flows downward, the liquid-gas interface is lowered by axisymmetric modulation of the free interface's period $\mathcal{L}$, where $\mathcal{L} > 2\pi\mathcal{R}$ [Que90]. Consequently, the surface tension causes instability of the liquid film in the azimuthal direction.

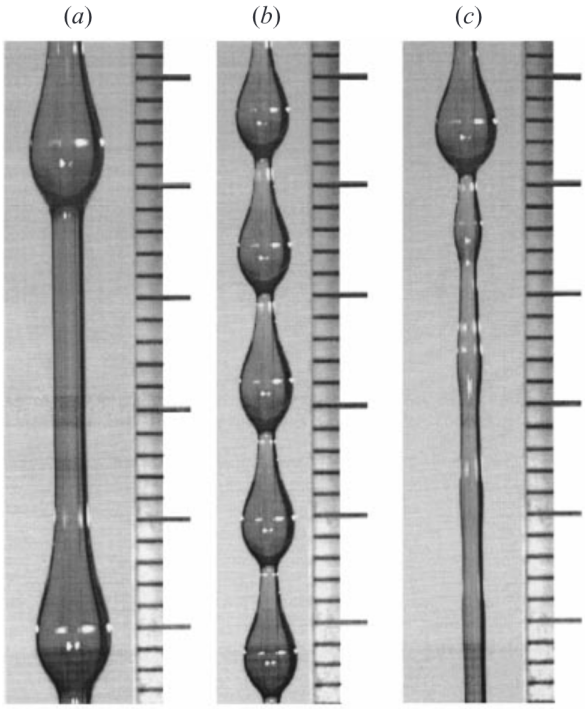

Figure 3.3: Three different flow regimes discovered by Kliakhandler et al. [KDB01]. We refer to these (a)-(c) regimes as convective, Rayleigh-Plateau, and isolated droplet regimes throughout the thesis. Reprinted with permission from Kliakhandler et al. [KDB01].

While surface tension destabilizes the flow in the azimuthal direction, it stabilizes the flow in the axial direction. This is a key physical feature of traveling beads down the vertical fiber; the surface tension plays both stabilizing and destabilizing roles [CM09]. In the azimuthal direction, the surface tension destabilizes the liquid layer by the Rayleigh mechanism, whereas in the axial direction, the surface tension stabilizes and restrains

the breakup of the film [Que90, KDB01, XD85]. This creeping flow, despite low inertial contributions, has rich dynamics including pulses and waves [CM09] due to various forces acting on it. For example, in 2001, Kliakhandler et al. observed and classified these three regimes as (a)-(c) (see Figure 3.3) from an experimental study using a caster oil with the Reynolds number around 10^{-2} [KDB01].

We refer to these (a)-(c) regimes as convective, Rayleigh-Plateau, and isolated droplet regimes throughout the paper using the convention suggested by Ji et al. [JFS19]. The convective regime observed when the flow rate is high corresponds to the flow profile, where irregular droplets collide with each other. The Rayleigh-Plateau regime corresponds to the flow profile, where beaded traveling waves propagate nearly constantly. The isolated droplet regime observed when the flow rate is low corresponds to the flow profile, where small wavy patterns follow well-separated large droplets. Varying the size of nozzle [SZJ17], the flow rate of the fluid, and the fiber radius [KDB01] all influence the beads' size and velocity, allowing one to observe the three regimes. Among these regimes, the Rayleigh-Plateau regime produces a uniformly spaced string of beads with a large liquid-gas interfacial area. Slowly falling droplets extend the contact time of the liquid with the gas and often result in the mixing of the gas and the liquid at the liquid-gas interface. As a result, the flow is well-suited for designing mass-transfer [UMO03, GLH12, CUM00] and heat-transfer devices [ZSW17, ZSJ18]. Recently, the applications are further extended to desalination [ZSJ19], water and CO_2 capturing [SZJ19], and microfluidics [GTV09]. Examples of such devices are illustrated in Figure 3.4.

3.2 Mathematical models of a thin liquid film flowing down a vertical fiber

Several models have been developed for fiber coating dynamics. Classical lubrication approximation is used to approximate the dynamics. Frenkel [Fre92], Kalliadasis & Chang [KC94],

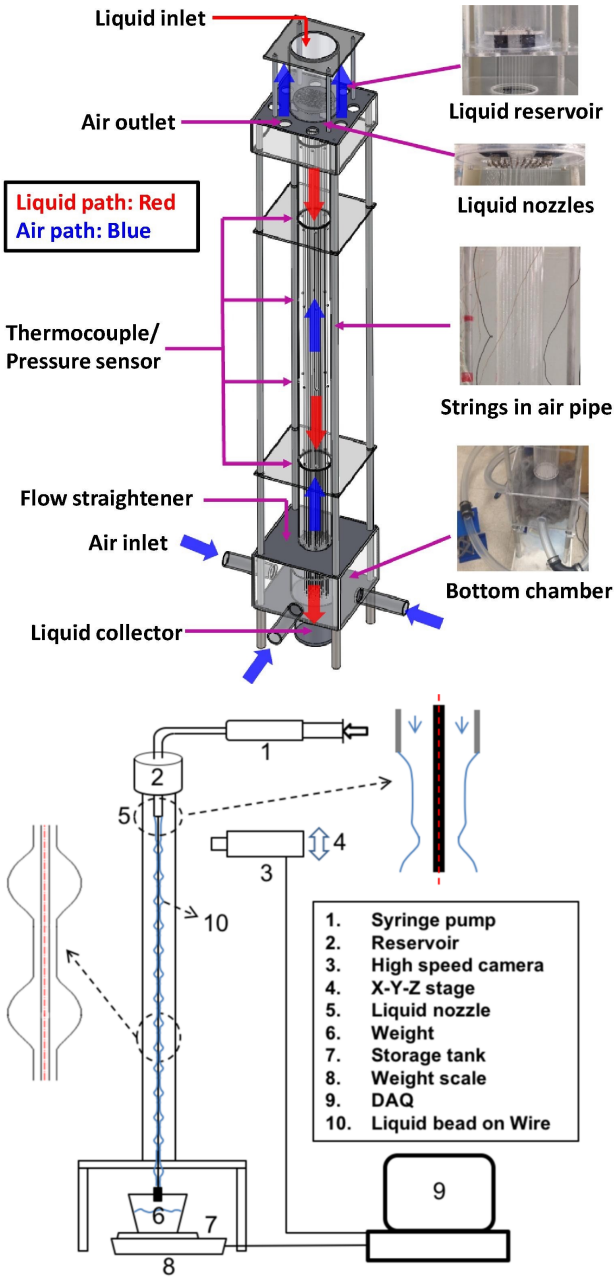

Figure 3.4: Top: Experimental setup for a direct contact heat exchanger using multiple strings. Reprinted from "Thermohydraulic characteristics of a multi-string direct-contact heat exchanger", Volume 126, Part A, Zheng et al. [ZSJ18], 536-544, Copyright (2018), with permission from Elsevier. Bottom: Experimental setup for the Rayleigh-Plateau regime study. Reprinted with permission from Sadeghpour et al. [SZJ17], Copyright (2017) American Chemical Society.

Kerchman & Frenkel [KF94], and Chang & Demekhin [CD99] proposed work on weakly nonlinear thin-film equations under the assumption that the film is a thin film. These investigations show that when subjected to large-magnitude waves, the flow reveals interesting dynamics. To describe moderate flow rate, Trifonov et al. [Tri92] first developed a system of evolution equations for both film thickness and volumetric flow rate. Following that, Kliakhandler et al. [KDB01] then proposed a model with fully nonlinear curvature, in which the film thickness is at least as large as the fiber radius.

Craster & Matar [CM06] also developed an evolution equation based on the assumption that the film thickness is at least as large as the fiber radius and that the bond number is low. They used a scaling that is similar to that used in long-wave theories of viscous fluids [ED94, ODB97]. Their model also includes surface tension that destabilizes the flow in the azimuthal direction while stabilizing the flow in the axial direction. In the same year, Sisoev et al. [SCM06] proposed an improved model of Trifonov et al. [Tri92] by incorporating the integral boundary layer method to describe the liquid film of moderate flow rate. Ruyer-Quil et al. [RTG08] employed the weighted residual method to introduce their simple (linear) and extended model (nonlinear), which included second-order dissipation. Both the extended and simple models predicted the bead speed of the Rayleigh-Plateau regime with errors of less than 10% and 1.2%, respectively.

Many previous models restricted their analysis on the no slip boundary condition at the solid-liquid interface until Haefner et al. [HBB15] employed the slip boundary condition. When the gravitational effect is ignored, Haefner et al. [HBB15] showed that the slippage has a significant effect on the growth rate of undulation. Later, Halpern & Wei [HW17] found that slip effects stimulate droplet formation and offered a likely hypothesis for obtaining different critical Bond numbers for droplet formation in the predicted case and experimental case. Chao et al.'s study [CDL18] also supported this idea since they observed that wall slippage increases the size and speed of droplets for thin liquid films flowing down a uniformly heated (cooled) cylinder.

Ji et al. [JFS19] also observed that keeping the slip term in their Film Stabilization model (FSM) affected the droplet size to grow taller and narrower compared to disregarding the slip term. They confirmed that the dependence of the bead speed on the slip length agrees with the work of Halpern and Wei [HW17]. While slip term has an impact on predicting bead propagation velocities, Ji et al [JFS19] concluded that it is not the most important factor that determines accurate prediction against experimental data. Instead, the film stabilization term plays a more critical role in accurately predicting the speed of the beads and, consequently, the transition between different flow regimes. This idea is further affirmed in Section 4.5.2, as simulations of our method without the slip effect shows a strong agreement with experimental data.

Indeed, it is not surprising to see that traveling beads play a vital part in determining flow regimes. The behavior of pulses and droplets is determined by the film thickness near these waves, according to both theories [KC94, CD99, YH13] and experiments [Que90, RTG08, CM06]. When the liquid film is thicker than a critical value c, the wave is propagated by combining fluid from nearby. On the other hand, thinner films are rather steady propagating traveling waves at a constant speed. In Chapter 4, we demonstrate that the film stabilization term is unnecessary for our positivity-preserving numerical method, thereby showing that our numerical method does not require an additional stabilizing effect.

Several articles also presented in-depth simulations of mathematical models and compared them with laboratory experiments [KDB01, CM06, DRK07, JFS19, JSJ20, JFS21]. Here, we introduce a few relevant articles. Kliakhandler et al. [KDB01] employed a standard pseudo-spectral technique and the fourth-order Runge-Kutta method to solve their evolution equation. The simulations were conducted with periodic boundary conditions. Their simulations closely matched the laboratory experimental data for the Rayleigh-Plateau regime and convective regimes in terms of the height of the prominent drop and the minimum thickness of the film. However, the simulations were not able to provide accurate estimates for the isolated droplet regimes. In addition, the distance between the drops was poorly estimated, with some

simulations yielding approximately half the distance observed in the laboratory experiments.

Craster & Matar [CM06] conducted two types of numerical simulations for their model: the traveling wave solution and the long-time solution. Both simulations were performed under the periodic boundary assumption and were compared against laboratory experimental data acquired by Craster & Matar themselves, as well as laboratory experimental data acquired by Kliakhandler et al. [KDB01]. In the case of traveling waves, solutions with smaller domain sizes exhibited slower speeds compared to those with larger domain sizes. This behavior represents that longer waves eventually catch up with and absorb the shorter waves, which aligns with laboratory experimental observations. For the long-time simulations, Craster & Matar [CM06] investigated the naturally selected "steady states" from families of solutions to their model. The significance of their simulations lies in successfully capturing small-amplitude wave patterns driven by instabilities for the isolated droplet regime, both upstream and downstream of the most prominent bead. While the presence of ripples downstream of the bead was consistent with experimental observations, the presence of ripples upstream of the bead was not.

Ruyer-Quil et al. [RTG08] conducted numerical simulations of their model, Craster & Matar's model [CM06], and Trifonov et al.'s model [Tri92] and compared them to experimental data acquired by Kliakhandler et al. [KDB01] and Duprat et al. [DRK07]. Traveling wave solutions for their model and Craster & Matar's model [CM06] were calculated numerically using the continuation software Auto97 developed by Doedel et al. [DCF98]. Although Ruyer-Quil et al.'s models [RTG08] underpredicted the propagation speeds of solutions in many cases, the speeds, maximum thickness of the film, and shapes of the solutions closely matched those of Craster & Matar's model [CM06] at the small wave number limit. The linear and nonlinear traveling wave solutions of Ruyer-Quil et al.'s model [RTG08] also better predicted small-amplitude wave patterns for the isolated droplet regime. Their simulations were almost absent of small wave patterns upstream of the most prominent bead, which is consistent with experimental observations.

In addition to conducting traveling wave solution simulations, Ruyer-Quil et al. [RTG08] utilized a second-order finite-difference quasi-linearized Crank-Nicolson scheme to obtain time-dependent simulations for their own model, as well as for Craster & Matar's [CM06] and Trifonov et al.'s models [Tri92]. They applied a soft boundary condition at the outlet, assuming that the flux behaves like a linear hyperbolic wave equation. The time-dependent simulations of their second-order nonlinear model exhibited good agreement with experimental data obtained by Kliakhandler et al. [KDB01], except for the isolated droplet regime, as well as with experimental data acquired by Duprat et al. [DRK07]. Ruyer-Quil et al. [RTG08] also pointed out that Craster & Matar's [CM06] and Trifonov et al.'s models [Tri92] were limited in their ability to simulate the spatiotemporal dynamics of the flow, as the numerical solutions did not correspond to the experimental observations for a few cases.

Following a series of articles on numerical simulations, Ji et al. [JFS19] pursued a similar approach and provided numerical simulations of the Craster & Matar model (CM) as well as their three new models: Slip Craster & Matar model (SCM), Full Curvature Model (FCM), and Film Stabilization Model (FSM). The focus of the simulations mostly lies on CM and FSM, as the other models were simulated to understand the contributions of the slip effect and full curvature to bead velocities and bifurcation. They numerically calculated traveling wave solutions of FSM and CM and compared the profiles with experimental data from Ji et al.'s own experiments [JFS19]. Notably, their FSM accurately predicted the bead speeds provided by the experimental data better than any other models and even worked well as nozzle sizes varied. Still, predicting the bead speed for the isolated droplet regime remained a challenge.

Ji et al. [JFS19] also simulated time-dependent FSM and CM models using a fully implicit second-order finite difference method. To study the regime transition from the Rayleigh-Plateau regime to the isolated droplet regime, they initialized the simulation with a slight perturbation of a traveling wave solution using the parameters from their isolated droplet regime experiment. As the simulation progressed, larger droplets that traveled faster merged

with smaller droplets, resulting in a typical isolated droplet regime. Additionally, their model captured the differences in the advancing and receding contact lines of droplets, although the distinction was less illustrated compared to the experimental data.

The most critical limitation of the current models and mathematical theory is that they are not fully capable of carefully characterizing regimes and their transitions. The convective regime and isolated droplet regimes were qualitatively described by the model from Kliakhandler et al. [KDB01] and Craster & Matar [CM06] but bead velocities of the flow were overestimated by a significant amount (over 40%). Ji et al. [JFS19] and Ruyer-Quil et al. [RTG08] presented better models predicting the bead velocities but these are still limited to the Rayleigh-Plateau regime. The challenges related to predicting the flow profile and bead velocities for isolated droplet regimes are repeatedly emphasized in several studies [KDB01, CM06, RTG08, JFS19] due to the inherent instability patterns near the beads. We have addressed this issue in Chapter 4 and provided simulations of the isolated droplet regime that match well with experimental data as well as effectively handle the instability near the droplet.

There was also some discrepancy in the bifurcation analysis of the Rayleigh-Plauteau state. For example, Craster & Matar concluded that the Rayleigh-Plataeu regime is a transient state when it is actually a steady-state phenomenon. Their model also produced isolated droplet regimes even when the experimental parameters were still in the Rayleigh-Plateau regime. Studies from Duprat et al. [DRK07] and Smolka et al. [SNG08] investigated regime transitions and steady-states of fiber coating flow further, but the quantitative model still could not resolve the discrepancies. Ji et al. [JFS19] addressed this issue in their paper and analyzed the relationship between the velocity of wave propagation and its effect on regime transitions. The article presented comprehensive experimental, theoretical, and numerical results on regime transitions, yet most of their analysis focused on a few specific cases within the Rayleigh-Plateau regime.

Despite these limitations, the film stabilization model proposed by Ji et al. [JFS19]

demonstrated remarkable performance when compared to experimental data. Not only did they successfully capture the bifurcation of regime transition from the Rayleigh-Plateau regime to the Isolated Droplet regime, but their study also accurately predicted bead velocities and flow profiles in the Rayleigh-Plateau regime. The model demonstrated a clear transition from the Rayleigh-Plateau regime to the isolated droplet regime, given the parameters used for laboratory experiments. The model correctly identifies the parameters for the Rayleigh-Plateau regime, while other models, such as CM, falsely predict the regime. As a consequence, we investigate their model thoroughly in the next section and modify it to create our numerical method in Chapter 4.

While studying the code provided by Ji et al. [JFS19], which implements a fully implicit second-order finite difference method, we observed multiple instances of a finite-time rupture of the film when using an underresolved grid within the range of physically relevant parameters. This phenomenon is not exclusive to their model but has also been observed in Ruyer-Quil et al.'s model [RTG08] when keeping their parameter α^1 relatively small. Additionally, we observed a finite-time rupture of the film while simulating the Craster & Matar model. The instability is attributed to the cylindrical geometry and leads to an unphysical blow-up in the time-dependent simulation. Ruyer-Quil et al. [RTG08] conjectured that this behavior is due to the poor convergence properties of the logarithmic function $\log(\alpha)$ as $\alpha \to 0$, but our observations indicate that even higher values of α can result in a finite-time rupture as well. We conjecture that as small waves are absorbed into larger droplets, the instabilities at downstream of a merged bead become amplified. This idea has motivated us to develop a positivity-preserving numerical method for thin film models on a fiber geometry.

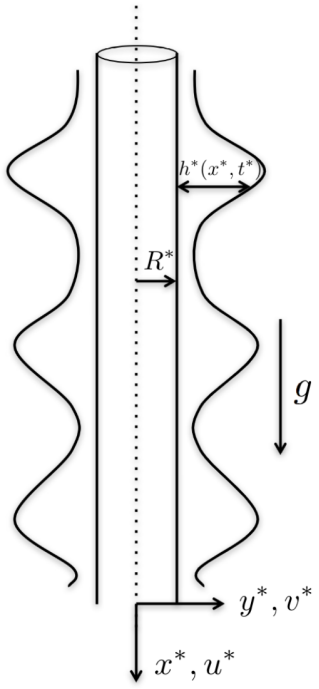

Figure 3.5: Schematic for the vertical fiber coating problem described in Section 3.1 with dimensional parameters. Reprinted with permission from Ji et al. [JFS19].

3.3 Derivation of a model equation

In this section, we derive a model from [JFS19] which will be used as our main partial differential equation to build our numerical method. The schematic of the liquid film flowing down on a vertical fiber with dimensional parameters is presented in Figure 3.5. We assume a Newtonian fluid flowing down a vertical cylinder of radius R^* (as shown in Figure 3.5). Assuming axis-symmetric flow in the azimuthal direction, one can write dimensional Navier-Stokes equations and the continuity equation as

$$u^*_{t^*} + u^* u^*_{x^*} + v^* u^*_{y^*} = -\frac{p^*_{x^*}}{\rho} + g + \nu \left(u^*_{x^*x^*} + \frac{u^*_{y^*}}{y^*} + u^*_{y^*y^*} \right), \tag{3.1}$$

[1]We denote it as α here since it is scales similarly to the α we used in Section 3.3

$$v^*_{t^*} + v^* v^*_{y^*} + u^* v^*_{x^*} = -\frac{p^*_{y^*}}{\rho} + \nu \left(\frac{v^*_{y^*}}{y^*} + v^*_{y^* y^*} - \frac{v^*}{y^{*2}} + v^*_{x^* x^*} \right), \tag{3.2}$$

$$v^*_{y^*} + \frac{v^*}{y^*} + u^*_{x^*} = 0, \tag{3.3}$$

where t^*, u^*, and v^* represents time, axial and radial velocity, respectively. p^* is pressure and g^* is the gravitational acceleration while ν represents the usual kinematic viscosity. We assume surface tension σ, density ρ, and kinematic viscosity ν of a liquid to be constant.

Equations (3.1)-(3.3) are solved subject to the boundary conditions imposed at two different locations: the solid-liquid interface at $y^* = R^*$ and the liquid-gas interface at $y^* = R^* + h^*$. At the solid-liquid interface, the flow must obey a no-penetration boundary condition with a slip or no slip condition,

$$v^* = 0, \quad u^* = \lambda^* u^*_{y^*} \quad \text{at} \quad y^* = R^*, \tag{3.4}$$

a slip condition for ($\lambda^* > 0$ [MWW05, HW17]) and the no slip condition for ($\lambda^* = 0$ [CM06]).

At the liquid-gas interface, the normal and the tangential stress must be balanced and must comply with the kinematic boundary condition as well,

$$p^* = \frac{2\mu}{1 + h^{*2}_{x^*}} (h^{*2}_{x^*} u^*_{x^*} - h^*_{x^*}(v^*_{x^*} + u^*_{y^*}) + v^*_{y^*}) + \frac{\sigma}{(1 + h^{*2}_{x^*})^{3/2}} \left(\frac{1 + h^{*2}_{x^*}}{R^* + h^*} - h^*_{x^* x^*} \right), \tag{3.5}$$

$$(1 - h^{*2}_{x^*})(v^*_{x^*} + u^*_{y^*}) + 2h^*_{x^*}(v^*_{y^*} - u^*_{x^*}) = 0, \tag{3.6}$$

$$h^*_{t^*} + u^* h^*_{x^*} = v^*, \tag{3.7}$$

at $y^* = R^* + h^*$. The next step is to scale Equations (3.1)-(3.7) with adequate dimensionless parameters in order to reduce the equations asymptotically. The key here is to solve the equations in the *long-wavelength* limit [CM06, ODB97]. In other words, one assumes that the thickness of the liquid film is much smaller than the characteristic axial length. Suppose the radial length scale is $\mathcal{H}$ and the streamwise length scale is $\mathcal{L} = \mathcal{H}/\epsilon$. The scaling ratio

$\epsilon = (\rho g \mathcal{H}^2/\sigma)^{1/3}$ balances the term σ introduced in p^* and the gravity g. The scaling of streamwise velocity, pressure, and time can then be defined by $\mathcal{H}, \mathcal{L}$, and ϵ which let us produce nondimensionalized equations containing ϵ and Re. We can observe $\epsilon = (\rho g \mathcal{H}^2/\sigma)^{1/3} \ll 1$ as the surface tension is dominant over the gravitational acceleration, letting us disregard higher order terms of ϵ. Similarly, the boundary conditions are reduced after asymptotic expansion with respect to ϵ.

The reduced set of equations is

$$1 - \frac{\partial p}{\partial x} + \frac{\partial^2 u}{\partial y^2} + \frac{u_y}{y} = 0, \tag{3.8}$$

$$-\frac{\partial p}{\partial y} = 0, \tag{3.9}$$

$$\frac{\partial u}{\partial x} + \frac{\partial v}{\partial y} + \frac{v}{y} = 0, \tag{3.10}$$

with boundary conditions,

$$v = 0, \quad u = \lambda u_y \quad \text{at} \quad y = R, \tag{3.11}$$

$$p = \frac{\alpha}{\epsilon^2(1+\alpha h)\sqrt{1+\epsilon^2 h_x^2}} - \frac{\partial^2 h}{\partial x^2}, \quad u_y = 0, \quad h_t + u h_x = v \quad \text{at} \quad y = R + h, \tag{3.12}$$

where $\alpha = \mathcal{L}/\mathcal{R}^*$ describes the aspect ratio between radial length and the fiber thickness.

Finally, by integrating (3.10) across the thin film width, we derive the evolution equation,

$$(1+\alpha h)\frac{\partial h}{\partial t} + \frac{\partial q}{\partial x} = 0, \quad \text{where} \quad q = \frac{1}{R}\int_R^{h+R} uy \, \mathrm{d}y. \tag{3.13}$$

In particular, if we assume the initial streamwise velocity to be the Nusselt solution,

$$u_0(y) = -\frac{1}{4}(y^2 - R^2) + \frac{1}{2}(h+R)^2 \log\left(\frac{y}{R}\right) + h\lambda\left(\frac{h}{2R} + 1\right). \tag{3.14}$$

The flow rate q can be further simplified as

$$q = \left(1 - \frac{\partial p}{\partial x}\right) q_0, \quad q_0 = \frac{1}{R}\int_R^{R+h} u_0 y \, \mathrm{d}y = \frac{h^3}{3}\phi(\alpha h) + \frac{h^2}{4}(\alpha h + 2)^2 \lambda. \tag{3.15}$$

Combining the equation (3.13) and the equation (3.15), we can write the generalized thin film equation as

$$\partial_t \left(h + \frac{\alpha}{2} h^2 \right) + \partial_x \left[\mathcal{M}(h) \left(1 - \partial_x \left[Z_{FS}(h) - \partial_x^2 h \right] \right) \right] = 0, \tag{3.16}$$

for

$$\mathcal{M}(h; \lambda, \alpha) = \frac{h^3}{3} \frac{\phi(\alpha h)}{\phi(\alpha)} + \frac{h^2 (\alpha h + 2)^2 \lambda}{4\phi(\alpha)}, \tag{3.17}$$

$$\phi(x) = \frac{3}{16 x^3} \left[(1+x)^4 (4 \log(1+x) - 3) + 4(1+x)^2 - 1 \right]. \tag{3.18}$$

In this equation, we approximate $p = h_{xx} - Z_{FS}(h)$ with

$$Z_{FS}(h) = \frac{\alpha}{\eta(1 + \alpha h)} - \frac{A}{h^3}. \tag{3.19}$$

One can understand the first term of Z_{FS} as a linearized unbalanced azimuthal curvature term while the second term represents disjoining pressure.

In this model, a long-range attractive part of the apolar van der Waals forces is used for $\Pi(h) = -A_H/h^3$, where A_H represents a positive Hamaker constant. Van der Waals interactions effects are frequently incorporated into the equation by adding disjoining pressure terms in lubrication equations [Gen85, ODB97, OB01, RB92]. $\Pi(h) = -A_H/h^3$ describes the liquid's wetting behavior on a solid substrate. Different formulas of disjoining pressure can be used by defining a combination of long-range and short-range intermolecular forces. For the review of this topic, we refer the readers to de Gennes [Gen85], Bonnet et al. [BEI09], and Israelachvili [Isr11].

CHAPTER 4

Positivity-preserving numerical method for a thin liquid film on a vertical cylindrical fiber

4.1 Introduction

Thin-film flows over fibers exhibit complex dynamical properties due to interplay among various forces, such as surface tension, viscous force, gravity, and inertia force. In the Rayleigh instability regime, an initially uniform flow quickly breaks up into regularly spaced beads, and forms traveling waves in the presence of gravity along the fiber direction [Que90, KRS12c]. The beaded morphology creates an array of localized high-curvature regions that act as radial sinks, making it attractive for devices for heat and mass transfer along the liquid-gas interfaces [SZJ19, GB21]. These thin-film flows have applications in gas absorption [UMO03, GLH12, CUM00], heat exchange [ZSW17, ZSJ18], microfluidics [GTV09], desalination [SZJ19], and others. The wide variety of potential applications attracted theoretical studies over the last few decades [CM09, KRS12c, CD99, DRG09, RTG08, SZJ17, Que90, Que99].

The fundamental component determining the profile of the thin liquid film on a vertical fiber is surface tension, which has a stabilizing effect on the axial curvatures, and destabilizing effect on the azimuthal curvatures of the interface [KDB01]. In addition, other factors increasing the flow's complexity are the cylindrical geometry of the fiber and the gravitational force. Experimentally, interfacial instabilities of the flow have been studied over decades [Que90, Que99]. Kliakhandler et al. experimentally characterized the three distinct regimes of interfacial patterns (a)-(c) [KDB01]. In this chapter, we use the convention by Ji et

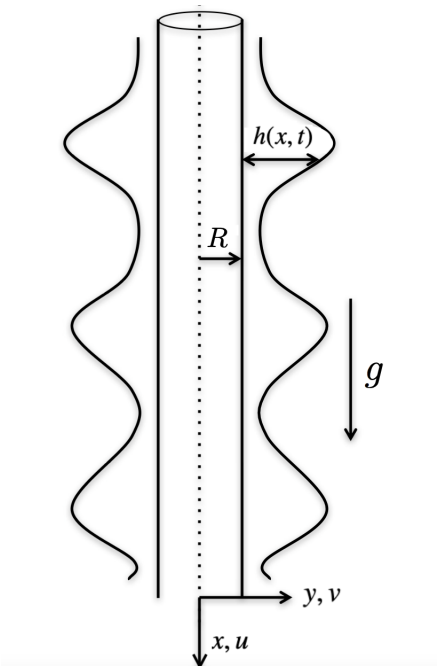

Figure 4.1: Illustration of a thin liquid film flowing down a vertical fiber.

al. [JFS19] and call (a)-(c) regimes convective, Rayleigh-Plateau, and isolated droplet regimes. The convective regime, observed when the flow rate is high, corresponds to the flow profile where irregular droplets collide with each other. The Rayleigh-Plateau regime corresponds to the flow profile, where beaded traveling waves propagate nearly constantly. The isolated droplet regime, observed when the flow rate is low, corresponds to the flow profile where small wavy patterns follow well-separated large droplets. The distinct dynamics of each regime and its transition is extensively studied, both theoretically and experimentally [Que99, RTG09, KRS12c, RK12, JFS19, JTC22].

In this chapter, we consider reduced-order models of the Navier-Stokes equations incorporating linear and nonlinear effects of the flow. Li and Chao [LC20] summarize a few notable methods: the gradient expansion method [Fre92, CM06, HW17, JFS19], the integral method [Tri92, SCM06], the weighted residual method [RTG08, RK12, DRG09], and the energy integral method [NO09]. The models are often classified according to the size of the Reynolds number. For the low Reynolds number cases, the flow profile is approximated

by the Stokes equations combined with the lubrication approximation [JFS19, CM06]. For moderate Reynolds number cases, one incorporates inertial terms in the governing equation using the weighted residual boundary integral method [RTG08, DRG09]. Many of the models are verified against the experimental data [RTG08, DRG09]. For example, a recent study by Ji et al. shows a good agreement with experimental data by correctly predicting bead velocities, flow profiles, and regime transition bifurcation [JFS19].

A major challenge is that fiber coating equations are extremely difficult to solve both numerically and analytically. They are typically fourth-order degenerate nonlinear parabolic equations due to the surface tension in the dynamics. We consider the following model from [JFS19]:

$$\begin{aligned} &\frac{\partial}{\partial t}\left(h+\frac{\alpha}{2}h^2\right)+\frac{\partial}{\partial x}\mathcal{M}(h)+\frac{\partial}{\partial x}\left[\mathcal{M}(h)\frac{\partial p}{\partial x}\right]=0,\\ &\mathcal{M}(h)=O(h^n),\ p=\frac{\partial^2 h}{\partial x^2}-\mathcal{Z}(h). \end{aligned} \tag{4.1}$$

Equation (4.1) is an evolution equation of the film thickness $h(x,t)$. From left to right,

- $\frac{\partial}{\partial t}(h+\frac{\alpha}{2}h^2)$ denotes the mass change over time where $\alpha=\mathcal{H}/\mathcal{R}\geq 0$ is the aspect ratio between the characteristic length scale of film thickness $\mathcal{H}$ to the fiber radius R.

- $\mathcal{M}(h)$ is often referred to as the mobility function that describes the hydrodynamic interactions of the transverse waves. Many times, $\mathcal{M}(h)=O(h^n)$. For example, setting $\mathcal{M}(h)$ to $\mathcal{M}(h)=h^3$ corresponds to the no-slip boundary condition, and setting $\mathcal{M}(h)$ to $h^3+\beta h^n$ for $n\in(0,3)$ corresponds to various Navier-slip conditions (cf. [Ber95a]). The smoothness of $\mathcal{M}(h)$ near $h=0$ determines the qualitative behavior of solutions at zero [GR01].

- The pressure p consists of two terms - the linearized curvature $\frac{\partial^2 h}{\partial x^2}$, representing the streamwise surface tension, and the $\mathcal{Z}(h)$, representing other nonlinear pressure effects. $\mathcal{Z}(h)$ often contains a destabilizing surface tension term that arises from the azimuthal curvature but can also include other terms.

Equation (4.1) is considered state of the art for this problem because it quantitatively agrees with bead velocities, flow profiles, and regime transition bifurcations as compared to experiments. Previously, the model by Kliakhandler et al. [KDB01] incorporated fully nonlinear curvature to capture the qualitative behavior of the Rayleigh-Plateau and isolated droplet regime. Nevertheless, this model overestimated the beads' velocity by 40%. Craster & Matar's model [CM06] revisited this idea and presented an asymptotic model describing Rayleigh-Plateau and isolated droplet regime but again overestimated the bead velocity. Their model also identified the Rayleigh-Plateau regime to be transient rather than a stationary state. Duprat et al. [DRK07], and Smolka et al. [SNG08] further studied regime transitions but predicting the regime transitions remained challenging. Ji et al.'s film stabilization model (FSM) [JFS19] improved the preceding models by incorporating a film stabilization term among generalized pressure terms. This stabilization term was inspired by the attractive part of the long-range apolar van der Waals forces, which are carefully studied for the well-wetting liquids [RB92, BEI09]. One can see that simulating such complex models is a delicate procedure. Thus, it is vital to have a robust numerical method for simulating complex spatiotemporal dynamics to predict flow profiles and regime transitions.

The degeneracy of the mobility function $\mathcal{M}(h)$ and the complex nonlinear pressure terms $\mathcal{Z}(h)$ are two hurdles one needs to clear to construct a robust numerical method. First, the degeneracy of the mobility function presents a substantial challenge in numerically solving Equation (4.1) since the solution may lose regularity as $h \to 0$. Second, the nonlinear term $\mathcal{Z}(h)$ in pressure p complicates the problem further since it is often relatively large in magnitude as $h \to 0$. As a result, the numerical method can suffer from instabilities as $h \to 0$. Therefore, keeping h positive is not only crucial for the solution to be physically meaningful but also important for the solution to be accurate. Fortunately, we found similarities between Equation (4.1) and many lubrication-type equations, and realized we could view Equation (4.1)

as a variant of a lubrication-type equation with generalized pressure,

$$\frac{\partial h}{\partial t} + \frac{\partial}{\partial x}\left(\mathcal{M}(h)\frac{\partial p}{\partial x}\right) = 0 \quad p = \frac{\partial^2 h}{\partial x^2} - \mathcal{Z}(h), \quad \text{where} \quad f(h) \sim h^n \quad \text{as} \quad h \to 0. \tag{4.2}$$

One may see that setting $\alpha = 0$ and $\frac{\partial}{\partial x}\mathcal{M}(h) = 0$ in Equation (4.1) results in Equation (4.2). Setting $\alpha = 0$ would mean neglecting the effect of the fiber, and $\frac{\partial}{\partial x}\mathcal{M}(h) = 0$ would mean neglecting the advection effect by liquid traveling downward. Such experimental and theoretical settings are discussed in various studies devoted to the lubrication theory so that we can take advantage of them [BGS03, LGB07, MBH10, GR01, Gru03]. We know the solution of (4.2) is smooth whenever the solution is positive but typically loses its regularity as the solution $h \to 0$ due to the degeneracy of the equation [BBD94, Ber96b]. We also know that the nonlinear pressure terms often introduce a large numerical instability as $h \to 0$, making it challenging to maintain the positive numerical solution [GR01, Gru03]. Examples of fiber coating problems include $\mathcal{Z}(h) = -(\alpha/\epsilon)^2 h$ in [YH13], assuming the thickness of the film is much smaller than the fiber radius ($\mathcal{H} \ll R$). Craster & Matar [CM06] used $\mathcal{Z}(h) = \frac{\alpha}{\eta(1+\alpha h)}$, assuming the film thickness comparable to the fiber radius ($\alpha = O(1)$). Ji et al. [JFS19] used that $\mathcal{Z}(h) = \frac{\alpha}{\eta(1+\alpha h)} - \frac{A}{h^3}$. In both the Craster & Matar model and Ji et al. model, we can expect numerical challenges when h is small. Indeed, we show in Section 4.5.1 that the numerical method used in [JFS19] can generate a false singularity as $h \to 0$ when the spatial grid size is underresolved. In other words, although the analytical solution of (4.1) is positive everywhere, the solution produced by a naive numerical method can produce negative values within some range of the solution when the grid size is underresolved. Such numerical methods can be quite difficult to extend to higher dimensions where grid refinement is computationally expensive. We also show that the negativity further prevents calculating the solution after the singularity. Thus, it is desirable to have a positivity-preserving numerical method that can perform well at different grid resolutions without spurious numerical singularities.

Constructing positivity-preserving methods for partial differential equations (PDEs) is addressed in a wealth of literature yet most of them are limited to the first or second-order equations [ZS10, ZS11, DP11, DJL21]. Equations above the second-order have no maximum

or comparison principles and higher-order spatial derivatives make the numerical system extremely stiff. Numerical methods for fourth or higher-order equations with positivity-preserving properties have received far less attention. Early works include [BBG98, ZB00, GR00, Gru03] and make use of entropy estimates to prove positivity. Some of the recent approaches use cut-off, or Lagrange multiplier methods which have a limitation in conserving mass or maintaining smoothness [LYZ20, LHV13]. Here we introduce a convex-splitting method that preserves physical quantities like energy, entropy, and mass [CWW19, DWZ19, HH20, GR01] which treats the stabilizing terms implicitly and the destabilizing terms explicitly. A few methods are unconditionally stable [Eyr98, VR03] which include the scalar auxiliary variable method by Huang et al. [HSW22]. The applications of these methods are to solve Cahn-Hilliard or Hele-Shaw cell-type equations.

This chapter presents a positivity-preserving numerical scheme that works on a general family of lubrication-type equations on cylindrical geometries. Positivity-preserving numerical methods have not been studied in the context of fiber coating, especially in the regime that is most relevant to physical experiments. The structure of the chapter follows. In Section 4.2, we prove properties that the PDE (4.1) holds and discuss how the PDE imparts such properties to our numerical methods. In Section 4.3, we introduce our numerical method and the state of art method used in Ji et al. [JFS19]. In Section 4, we present proof of the positivity and the consistency of our method. Section 4.5 contains numerical simulations of our methods. In particular, in Section 4.5.1, we compare simulations of our method with simulations of the state-of-the-art method while in Section 4.5.2, we compare simulations of our method with laboratory experimental data. We also demonstrate how to employ adaptive time stepping to efficiently implement our method in Section 4.5.3. An example without any numerical singular behavior is presented in Section 4.5.3.1 whereas an example with a finite time numerical singular behavior is presented in Section 4.5.3.2. We also compare the CPU time of simulating our method and the state-of-the-art method in Section 4.5.3.3.

4.2 Properties of the partial differential equation

This section investigates two essential properties of the continuous fiber coating Equation (4.1). We ensure that our numerical method preserves the discrete equivalent of the properties. We consider the following initial-boundary value problem:

$$(P)\begin{cases} \dfrac{\partial}{\partial t}\left(h+\dfrac{\alpha}{2}h^2\right)+\dfrac{\partial}{\partial x}\left[\mathcal{M}(h)\left(1+\dfrac{\partial p}{\partial x}\right)\right]=0 \text{ in } L_T=(0,L)\times(0,T)\subset\mathbb{R}^2, \\ p=\dfrac{\partial^2 h}{\partial x^2}-\mathcal{Z}_+(h)-\mathcal{Z}_-(h), \\ \text{periodic boundary conditions on } [0,L], \\ h(x,0)=h_0(x)>0. \end{cases}$$

The main difference from previous Equation (4.1) is that we split $\mathcal{Z}(h)$ into two parts: $\mathcal{Z}_+(h)$ and $\mathcal{Z}_-(h)$, where $\mathcal{Z}'_+(h)\geq 0$ and $\mathcal{Z}'_-(h)\leq 0$. Such splittings are not generally unique but useful in the design of stable numerical schemes. An example is discussed in Section 4.5.1. We assume periodic boundary conditions for simplicity and a positive initial condition to match the physical setting.

Here we assume that a smooth positive solution exists to the problem (P). The existence of a solution to problems such as (P) has been studied in depth [BF90, BP94, JTC22]. The general procedure is like this. First, one applies a regularization technique to the problem (P) to overcome the degeneracy and make the problem uniformly parabolic. The boundary condition can be extended to the whole line using a proper continuation technique such as the one suggested in [Sol65]. The well-known parabolic Schauder estimates [Sol65, Fri58] guarantees a unique solution in a small time interval say, $L_\sigma=(0,L)\times(0,\sigma)$. In the end, the limit of the regularized solution results in a smooth, positive solution. We direct our readers to [BF90, JTC22] for the full derivation. We believe a similar derivation is possible through the canonical approach, although the continuation of solutions past the initial small time interval requires a priori bounds on certain norms. A full discussion of the existence of the problem (P) is beyond the scope of this chapter.

The key idea of developing a positivity-preserving numerical method is to formulate an entropy estimate for the continuous problem (P). Such an estimate guarantees the positivity of solutions in the continuous setting. Therefore, designing a numerical method that satisfies the discrete equivalent of the entropy estimate will result in a positivity-preserving numerical method. For our problem (P), we define entropy $G(h)$ so that its derivative $G'(h)$ satisfies

$$G'(h) = (1 + \alpha h) \int_A^h \frac{1}{\mathcal{M}(s)}\, ds \quad \text{for some fixed } A > 0.$$

We point out that the positivity proof for a continuous solution in Section 4.2, the definition of numerical methods in Section 4.3, and the positivity proof for a discrete solution in Section 4.4 do not explicitly involve the constant $A > 0$. In other words, A is only involved in $G'(h)$ to ensure that it is well-defined. We claim that solutions to the problem (P) satisfy the conservation of mass and an entropy estimate.

Proposition 4.2.1. *Suppose that there exists a solution $h \in C^4(L_T)$ of (P), where $L_T = [0, L) \times [0, T)$. Suppose we further assume*

$$\mathcal{M}(h) = O(h^n),\ \mathcal{M}(h) \geq 0,$$
$$\mathcal{Z}_+,\ \mathcal{Z}_- \in C^2(\mathbb{R}^+), \quad \textit{and} \quad \mathcal{Z}'_+(h) \geq 0,\ \mathcal{Z}'_-(h) \leq 0.$$

Then, the solution h satisfies the following two properties:

$$(I)\ \int_0^L h(x,T) + \frac{\alpha}{2}h^2(x,T)\, dx = \int_0^L h(x,0) + \frac{\alpha}{2}h^2(x,0)\, dx \ (\textit{Conservation of mass}),$$
$$(II) \int_0^L G(h(x,T))\, dx \leq \int_0^L G(h(x,0))\, dx + \int_{L_T} \left(\frac{\mathcal{Z}_-(h)}{2}\right)^2 dxdt \ (\textit{Entropy estimate}).$$

Proof. The conservation of mass (I) is achieved by integrating the problem (P) on L_T,

$$\int_{L_T} \frac{\partial}{\partial t}\left(h + \frac{\alpha}{2}h^2\right) dxdt = -\int_{L_T} \frac{\partial}{\partial x}\left[\mathcal{M}(h)\left(1 + \frac{\partial p}{\partial x}\right)\right] dxdt$$
$$\implies \int_0^L \left(h(x,T) + \frac{\alpha}{2}h^2(x,T)\right) dxdt - \int_0^L \left(h(x,0) + \frac{\alpha}{2}h^2(x,0)\right) dxdt = 0.$$

Note that the periodic boundary condition removes the complex expression surrounded by $\frac{\partial}{\partial x}[\cdots]$ on the left-hand side of the equality in the first line.

The entropy estimate (II) is achieved by

$$\begin{aligned}\frac{d}{dt}\int_0^L G(h)dx &= \int_0^L G'(h)h_t dx \\ &= \int_0^L \left\{(1+\alpha h)h_t \int_A^h \frac{1}{\mathcal{M}(s)}ds\right\} dx \\ &= -\int_0^L \left\{\frac{\partial}{\partial x}\left[\mathcal{M}(h)\left(1+\frac{\partial p}{\partial x}\right)\right]\int_A^h \frac{1}{\mathcal{M}(s)}ds\right\} dx \\ &= \int_0^L h_x\left(1+\frac{\partial p}{\partial x}\right)dx.\end{aligned}$$

The equalities are justified using integration by parts. Note that the periodic boundary plays a crucial role in simplifying expressions on the boundary. We use the definition $p = h_{xx} - \mathcal{Z}(h) = h_{xx} - \mathcal{Z}_+(h) - \mathcal{Z}_-(h)$ in

$$\begin{aligned}\frac{d}{dt}\int_0^L G(h)dx &= \int_0^L h_x dx + \int_0^L h_x \frac{\partial}{\partial x}\left(h_{xx} - \mathcal{Z}(h)\right)dx \\ &= -\int_0^L h_{xx}^2 + \int_0^L h_{xx}\mathcal{Z}_-(h)dx - \int_0^L h_x^2 \mathcal{Z}'_+(h)dx \\ &= -\int_0^L \left(h_{xx} - \frac{Z_-(h)}{2}\right)^2 dx + \int_0^L \left(\frac{Z_-(h)}{2}\right)^2 dx - \int_0^L h_x^2\mathcal{Z}'_+(h)dx \\ &\le -\int_0^L \left(h_{xx} - \frac{Z_-(h)}{2}\right)^2 dx + \int_0^L \left(\frac{Z_-(h)}{2}\right)^2 dx.\end{aligned}$$

Again, the periodic boundary is crucial in eliminating $\int_0^L h_x dx$ in the first line. We simplify the expression by completing the square on the third line. We obtain the inequality in the last line because $\mathcal{Z}'_+(h) \ge 0$. Integrating over time gives us

$$\int_0^L G(h(x,T))\,dx + \int_{L_T}\left(h_{xx} - \frac{\mathcal{Z}_-(h)}{2}\right)^2 dxdt \le \int_0^L G(h(x,0))\,dx + \int_{L_T}\left(\frac{\mathcal{Z}_-(h)}{2}\right)^2 dxdt.$$

Finally, one can drop the second term on the left side of the inequality since it is nonnegative.

□

The above properties allow us to create a positivity-preserving numerical method due to the entropy estimate. Lubrication-type equations are well-known to satisfy entropy-dissipating

properties. Bernis et al. recognized the significance of the entropy dissipation property in third-order or higher degenerate parabolic equations and used it to prove the nonnegativity of weak solutions with sufficiently high degeneracy in one space dimension [BF90]. They also proved that the solution is unique and strictly positive if the mobility order $n \geq 4$. Following their work, several articles regarding lubrication-type equations discussed the importance of entropy estimates in numerical and analytical contexts [BBD94, BP96, ZB00, BBG98, GR00, GR01]. These ideas have largely been lacking in the fiber coating problem, except for the generalized entropy analysis done by Ji et al. [JTC22], which proves the existence of a nonnegative weak solution of a fiber-coating model with fully nonlinear curvature terms. In this chapter, we use these ideas to develop a positivity-preserving numerical solution.

4.3 Positivity-preserving finite difference method

In this section, we present a continuous time and discrete in space positivity-preserving finite difference method, Bounded Entropy Method (BEM), and compare it to a current state-of-the-art method General Method (GM) used in fiber coating models [JFS19]. Our method is second-order accurate in space while preserving the positivity of a numerical solution at each time. Our method is motivated by prior work by Zhornitskaya et al. [ZB00] and Grün et al. [GR01] for a simple lubrication model without the geometry and physics of fiber coating. Before introducing our method, we define the following notation.

Notation. *Suppose we divide our domain* $[0, L]$ *into* N *equally spaced grids of size* $\Delta x = L/N$. *Let* $u_i(t)$ *be a solution of a numerical method that is continuous in time and discrete in space at time* t *and on grid* i. *Define the forward difference in space and the backward difference in space as*

$$u_{i,x} = \frac{u_{i+1}(t) - u_i(t)}{\Delta x}, \quad u_{i,\bar{x}} = \frac{u_i(t) - u_{i-1}(t)}{\Delta x}.$$

Respectively, higher-order differences in space can be defined as

$$u_{i,\bar{x}x} = \frac{u_{i+1,\bar{x}} - u_{i,\bar{x}}}{\Delta x}, \quad u_{i,\bar{x}x\bar{x}} = \frac{u_{i,\bar{x}x} - u_{i-1,\bar{x}x}}{\Delta x}.$$

As we highlight the importance of the entropy $G(h)$ in designing a positivity-preserving method in Section 4.2, the discretized mobility $\mathcal{M}(h)$ is the key factor that determines the qualitative behavior of the solutions near zero. We define the discrete mobility function $m(s_1, s_2)$ according to Definition 4.3.1.

Definition 4.3.1 (Discretization of Mobility)**.** *The mobility term $\mathcal{M}(s)$ in the problem (P) is discretized to satisfy the following criteria [ZB00]:*

(a) $m(s, s) = \mathcal{M}(s)$,

(b) $m(s_1, s_2) = m(s_2, s_1)$,

(c) $m(s_1, s_2) \in C^4((0, \infty) \times (0, \infty)) \cap C([0, \infty] \times [0, \infty])$,

(d) $\forall \delta > 0$, *there exists* $\gamma > 0$ *such that* $s_1, s_2 > \delta \implies m(s_1, s_2) \geq \gamma > 0$.

The above definition of $m(s_1, s_2)$ is symmetric and continuously differentiable everywhere except possibly at 0. Condition (d) allows the $m(s_1, s_2)$ to be degenerate if one of the arguments $h \to 0$ but guarantees positivity if both of the arguments are greater than 0. Our positivity-preserving finite difference method, the Bounded Entropy Method (BEM) (4.3), presented below, satisfies Definition 4.3.1.

Bounded Entropy Method (BEM)**.** *The finite difference discretization of the problem (P) with continuous time is written as*

$$
\begin{aligned}
&(1 + \alpha u_i)\frac{du_i}{dt} + [m(u_{i-1}, u_i)(1 + p_{i,\bar{x}})]_x = 0, \quad p_i = u_{i,\bar{x}x} - \mathcal{Z}_+(u_i) - \mathcal{Z}_-(u_i), \\
&u_i(0) = u_0(i\Delta x),\ i = 0, 1, 2, \cdots, N, \\
&m(s_1, s_2) = \begin{cases} \mathcal{M}(s_1) & \text{if } s_1 = s_2, \\ (s_2 - s_1)/\int_{s_1}^{s_2} \frac{1}{\mathcal{M}(s)} ds & \text{if } s_1 \neq s_2. \end{cases}
\end{aligned}
\tag{4.3}
$$

In Section 4.4, we show that the above discretization of $\mathcal{M}(h)$ in the BEM (4.3) guarantees a discrete equivalent of the conservation of mass (I) and the entropy estimate (II). We also write the numerical method of Ji et al. [JFS19] as the following, which we refer to as GM (4.4).

Generic Method (GM). *The finite difference discretization of the problem* (P) *with continuous time is written as*

$$\begin{aligned} &(1+\alpha u_i)\frac{du_i}{dt} + [m(u_{i-1},u_i)(1+p_{i,\bar{x}})]_x = 0, \quad p_i = u_{i,\bar{x}x} - \mathcal{Z}_+(u_i) - \mathcal{Z}_-(u_i), \\ &u_i(0) = u_0(i\Delta x),\ i = 0,1,2,\cdots,N, \end{aligned} \tag{4.4}$$

where $m(s_1,s_2)$ *satisfies Definition 4.3.1.*

As an example of $m(s_1,s_2)$ used in GM (4.4), one can let $m(s_1,s_2) = \mathcal{M}(0.5(s_1+s_2))$ or $m(s_1,s_2) = 0.5(\mathcal{M}(s_1)+\mathcal{M}(s_2))$, where either one estimates the mobility at the midpoint. Note that $m(s_1,s_2)$ in BEM (4.3) and GM (4.4) uses center-difference, allowing the numerical method to conserve flux at each time step. Together with second-order consistency, both numerical methods are "shock capturing," which is a desirable property to have in conservation law type of equations [LeV90]. In the following section, we show that BEM (4.3) satisfies the conservation of mass and entropy estimate, which allows us to prove the positivity of the numerical method.

4.4 Positivity of numerical solutions

In the previous section, we claim that $m(s_1,s_2)$ in BEM (4.3) satisfies a discrete equivalent of the conservation of mass and the entropy estimates discussed in Section 4.2. In this section, we prove our claim through Proposition 4.4.1 and explain how such discretizations preserve the positivity of BEM (4.3) through Theorem 4.4.1. Our method is inherently more complex than entropy dissipating schemes for traditional lubrication-type equations because of three reasons. First, the time derivative of Equation (4.1) involves the geometry of the cylindrical fiber $\frac{\alpha}{2}h^2$. Second, a nonlinear advection $\frac{\partial}{\partial x}\mathcal{M}(h)$ is incorporated. Lastly, nonlinear pressure

p entails a destabilizing azimuthal curvature $\frac{\alpha}{\eta(1+\alpha h)}$. The coupled entropy estimate expression in Proposition 2.1 is consequently more complicated than "entropy dissipation", which is the case for the conventional lubrication-type equations. The following proposition is a discrete analog of Proposition 2.1.

Proposition 4.4.1. *Suppose $u_i(t)$ is a solution of the BEM (4.3) at time t and ith grid in space. Suppose we further assume*

$$\mathcal{M}(h) = O(h^n),\ \mathcal{M}(h) \geq 0,$$
$$\mathcal{Z}_+,\ \mathcal{Z}_- \in C^2(\mathbb{R}^+), \quad \mathcal{Z}'_+(h) \geq 0,\ \mathcal{Z}'_-(h) \leq 0,$$
$$G'(h) = (1+\alpha h)\int_A^h \frac{1}{\mathcal{M}(s)}\, ds \text{ for some fixed } A > 0.$$

Then, $u_i(t)$ satisfies the following two properties given $T > 0$:

$$(I)\ \sum_i \left(u_i(T) + \frac{\alpha}{2}u_i(T)^2\right)\Delta x = \sum_i \left(u_i(0) + \frac{\alpha}{2}u_i(0)^2\right)\Delta x$$

(*Discrete conservation of mass*),

$$(II)\sum_i G(u_i(T))\Delta x \leq \sum_i G(u_i(0))\Delta x + \int_0^T \sum_i \left(\frac{\mathcal{Z}_-(u_i(s))}{2}\right)^2 \Delta x ds$$

(*Discrete entropy estimate*).

Proof. The proof of the statements is very similar to the proof of Proposition 2.1. The only difference is that we multiply by Δx and sum over $i = 0, 1, 2, \cdots, N-1$ instead of integrating over space. Discrete conservation of mass (I) is achieved by integrating the first line of (4.3) by time and summing over $i = 0, 1, 2, \cdots, N-1$,

$$\int_0^T \sum_i (1+\alpha u_i)\frac{du_i}{dt}\Delta x = -\int_0^T \sum_i [m(u_{i-1}, u_i)(1 + p_{i,\bar{x}})]_x \Delta x$$
$$\implies \sum_i \left(u_i(T) + \frac{\alpha}{2}u_i(T)^2\right)\Delta x - \sum_i \left(u_i(0) + \frac{\alpha}{2}u_i(0)^2\right)\Delta x = 0.$$

As we saw in the continuous case, the periodic boundary condition removes the expression surrounded by $[\cdots]_x$.

The discrete entropy estimate (II) follows by

$$\begin{aligned}
\frac{d}{dt}\sum_i G(u_i)\Delta x &= \sum_i G'(u_i)\frac{du_i}{dt}\Delta x \\
&= -\sum_i \int_A^{u_i} \frac{1}{\mathcal{M}(s)} ds [a(u_{i-1},u_i)(1+p_{i,\bar{x}})]_x \Delta x \\
&= \sum_i \frac{1}{\Delta x}\left(\int_{u_{i-1}}^{u_i} \frac{1}{\mathcal{M}(s)} ds\right) a(u_{i-1},u_i)(1+p_{i,\bar{x}})\Delta x \\
&= \sum_i u_{i,\bar{x}}(1+p_{i,\bar{x}})\Delta x \\
&= \sum_i \left\{-(u_{i,\bar{x}x})^2 - u_{i,\bar{x}}[\mathcal{Z}'_+(u_i)]_{\bar{x}} + u_{i,\bar{x}x}\mathcal{Z}_-(u_i)\right\}\Delta x \\
&\leq -\sum_i \left(u_{i,\bar{x}x} - \frac{\mathcal{Z}_-(u_i)}{2}\right)^2 \Delta x + \sum_i \left(\frac{\mathcal{Z}_-(u_i)}{2}\right)^2 \Delta x.
\end{aligned}$$

Until the fourth line, the equalities are justified by integration by parts. Note that the periodic boundary plays a crucial role in simplifying expressions on the boundary and eliminating $\sum_i u_{i,\bar{x}}\Delta x$ in the fourth line. We obtain the inequality in the last line after completing the square and using the fact that $\mathcal{Z}'_+ \geq 0$. From the inequality, one integrates over time from 0 to T, which results in

$$\begin{aligned}
&\sum_i G(u_i(T))\Delta x + \int_0^T \sum_i \left(u_{i,\bar{x}x}(s) - \frac{\mathcal{Z}_-(u_i(s))}{2}\right)^2 \Delta x ds \\
&\leq \sum_i G(u_i(0))\Delta x + \int_0^t \sum_i \left(\frac{\mathcal{Z}_-(u_i(s))}{2}\right)^2 \Delta x ds.
\end{aligned}$$

Finally, one can drop the second term on the left side since it is nonnegative and the desired entropy estimate is achieved. □

We have two versions of theorems on the positivity: (a) a priori bound - depending on Δx and (b) a posteriori bound assuming a uniform Lipschitz condition on the numerical solution. We note that the solution is observed to have a uniform Lipschitz bound in all of our numerical simulations. Thus, the uniform Lipschitz assumption is observed numerically and thus can be used in an *a posteriori* argument. We leave proving the smoothness of PDE, such as establishing a uniform Lipschitz bound, as future work.

Theorem 4.4.1. *(Positivity of BEM) Suppose we have the same assumptions as Proposition 4.1. We further assume that* $(Z_-(s))^2 \leq C_1$ *for any* $s \geq 0$ *and the initial data* $u_i(0) > 0$. *Then, the solution of BEM* (4.3) *at time* $T > 0$, $u_i(T)$, *satisfies the following conditions:*

(a) if $n \geq 2$, *there exists* δ *such that* $u_i(T) \geq \delta(\Delta x) > 0$ *for all* i,

(b) if $n > 2$ *and* $u_i(t)$ *is uniformly Lipchitz on* $[0, T]$, $|u_i(s) - u_j(s)| \leq C_L|(i-j)\Delta x|$, $\forall i, j$, $\forall 0 \leq s \leq T$, *for some* $C_L > 0$, *there is a posteriori lower bound* δ, *independent of* Δx, *such that* $u_i(T) \geq \delta > 0$.

Proof. Notice that we assume that $\mathcal{M}(h) = O(h^n)$ and consider cases where $n \geq 2$. Thus, for the sake of simplicity, we take $\mathcal{M}(h) = h^n$ throughout the proof. More general cases can be proved similarly. Let us first prove statement (a). The given assumptions allow us to use the discrete entropy estimate (II) from Proposition 4.4.1.

First, we claim that $\sum_i G(u_i(T))\Delta x \leq C$ for a fixed constant C as any $u_i(T) \to 0$. Since we take $\mathcal{M}(h) = h^n$, we explicitly calculate $G(h)$ as

$$G(h) = \begin{cases} -\log h + O(h) + O(1) & \text{if } n = 2, \\ \frac{1}{(n-1)(n-2)} h^{-(n-2)} + O(h^{3-n}) + O(1) & \text{if } 2 < n < 3, \\ \frac{1}{2h} - \frac{\alpha}{2} \log h + O(h) + O(1) & \text{if } n = 3, \\ \frac{1}{(n-1)(n-2)} h^{-(n-2)} + \frac{\alpha}{(n-1)(n-3)} h^{-(n-3)} + O(h) + O(1) & \text{if } n > 3. \end{cases}$$

Here, the choice of A only affects the coefficients of the higher-order terms but not the leading-order term. Each $G(u_i(0))$ is also well defined because we have fixed initial data $u_i(0) > 0$. This leads us to conclude

$$\sum_i G(u_i(0))\Delta x \leq C_0 \text{ for some constant } C_0.$$

We also assume $(Z_-(u_i(s)))^2 \leq C_2$, which implies

$$\int_0^T \sum_i \left(\frac{\mathcal{Z}_-(u_i(s))}{2} \right)^2 \Delta x ds \leq C_2 T \text{ for some constant } C_2 \text{ as any } u_i(T) \to 0.$$

Hence, we get

$$\sum_i G(u_i(T))\Delta x \le \sum_i G(u_i(0))\Delta x + \int_0^T \sum_i \left(\frac{\mathcal{Z}_-(u_i(s))}{2}\right)^2 \Delta x ds \le C_0 + C_2 T \le C.$$

Next, we show that $\delta(T) = \min_i u_i(T) \ge 0$ using the boundedness of $\sum_i G(u_i(T))\Delta x$. Notice that each leading-order term of $G(\delta)$ is positive as $\delta \to 0$ up to constant differences,

$$G(\delta) = \begin{cases} -\log\delta + O(\delta) + O(1) & \text{if } n = 2, \\ \frac{1}{(n-1)(n-2)}\delta^{-(n-2)} + O(\delta^{3-n}) + O(1) & \text{if } 2 < n < 3, \\ \frac{1}{2\delta} - \frac{\alpha}{2}\log\delta + O(\delta) + O(1) & \text{if } n = 3, \\ \frac{1}{(n-1)(n-2)}\delta^{-(n-2)} + \frac{\alpha}{(n-1)(n-3)}\delta^{-(n-3)} + O(\delta) + O(1) & \text{if } n > 3. \end{cases}$$

Thus, $\delta \to 0$ implies $G(\delta) \to +\infty$, which contradicts $\sum_i G(u_i(T))\Delta x \le C$. Hence, we achieve $\min_i u_i(T) = \delta > 0$.

To prove (b), we use $\sum_i G(u_i(T))\Delta x \le C$ as well. From part (a), we have nonnegativity of $u_i(T)$, which implies

$$G(u_i(T)) = \int_B^{u_i} (1+\alpha v) \int_A^v \frac{1}{\mathcal{M}(s)} ds dv + O(1) \ge \int_B^{u_i} \int_A^v \frac{1}{\mathcal{M}(s)} ds dv + O(1),$$

for some $B > 0$.

Therefore,

$$\begin{aligned} C &\ge \sum_i G(u_i(T))\Delta x \ge \sum_i \int_B^{u_i} \int_A^v \frac{1}{\mathcal{M}(s)} ds dv \Delta x + O(1) \\ &\ge \sum_i \int_B^{u_i} \int_A^v \frac{1}{s^n} ds dv \Delta x + O(1) = \sum_i u^{2-n}\Delta x + O(1). \end{aligned}$$

Suppose $\delta(T) = \min_i u_i(T)$ occurs at i^*. Due to the uniform Lipschitzness, $u_i \le \delta + C_L|(i^* - i)\Delta x|$, $\forall i$, we obtain

$$\begin{aligned} \tilde{C} &\ge \sum_i \frac{1}{u_i^{n-2}}\Delta x \ge \sum_i \frac{\Delta x}{(\delta + C_L|(i-i^*)\Delta x|)^{n-2}} \ge \sum_i \frac{\Delta x}{(\delta + C_L(i\Delta x))^{n-2}} \\ &\ge \int_0^L \frac{dx}{(\delta + C_L x)^{n-2}} \ge \frac{1}{C_L\delta^{n-1}} \int_0^{LC_L/\delta} \frac{ds}{(1+s)^{n-2}}. \end{aligned}$$

If $\frac{LC_L}{\delta} \leq 1 \implies \delta \geq LC_L$ so we have a lower bound δ independent of Δx. In the case when $\frac{LC_L}{\delta} \geq 1$,

$$\tilde{C} \geq \frac{1}{C_L \delta^{n-1}} \int_0^1 \frac{ds}{(1+s)^n} = \frac{C'}{\delta^{n-1}},$$
$$\implies \delta \geq \left(\frac{C'}{\tilde{C}}\right)^{1/n-1}.$$

□

Corollary 4.4.2. *Continuous time, discrete space, numerical solutions of the Craster-Matar model (CM) [CM06] and the Film Stabilization Model (FSM) [JFS19] are positive at any time $T > 0$ and grid point i if we use the BEM* (4.3)*.*

Proof. For the two cases, the same mobility function $\mathcal{M}(h)$ is used, but different $\mathcal{Z}(h)$ is used. They are

$$\mathcal{M}(h) = \frac{h^3}{3}\frac{\phi(\alpha h)}{\phi(\alpha)} + \frac{h^2(\alpha h + 2)^2 \lambda}{4\phi(\alpha)},$$
$$\phi(x) = \frac{3}{16x^3}\left[(1+x)^4(4\log(1+x) - 3) + 4(1+x)^2 - 1\right],$$
$$\mathcal{Z}_{CM}(h) = \mathcal{Z}_{CM-}(h) = \frac{\alpha}{\eta(1+\alpha h)},$$
$$\mathcal{Z}_{FSM}(h) = \mathcal{Z}_{FSM+} + \mathcal{Z}_{FSM-} = -\frac{A_H}{h^3} + \frac{\alpha}{\eta(1+\alpha h)}.$$

We prove that the assumptions are satisfied for Theorem 4.4.1 by showing that $\mathcal{M}(h) = O(h^2)$ as $h \to 0$ and $(\mathcal{Z}_-(s))^2 \leq \left(\frac{\alpha}{\eta}\right)^2$. We simplify the calculation by letting $y = \alpha h$,

$$\begin{aligned}\frac{h^3\phi(\alpha h)}{3\phi(\alpha)} &= \frac{1}{16\alpha^3\phi(\alpha)}\left[(y+1)^4(4\log(y+1) - 3) + 4(y+1)^2 - 1 + 4\lambda\alpha y^2(y+2)^2\right] \\ &= \frac{1}{C}\left[A_4 y^4 + A_3 y^3 + A_2 y^2 + A_1 y + A_0\right],\end{aligned}$$

where

$$A_4 = 4\alpha\lambda + 4\log(y+1) - 3,\ A_3 = 16\alpha\lambda + 16\log(y+1) - 12,$$
$$A_2 = 16\alpha\lambda + 24\log(y+1) - 14, A_1 = 16\log(y+1) - 4,\ A_0 = 4\log(y+1).$$

As $y \to 0$, $\log(y+1) = O(y)$, which implies

$$\frac{h^3\phi(\alpha h)}{3\phi(\alpha)} = O(y^2) + \frac{1}{C}[A_1 y + A_0] = O(y^2) + 16y^2 - 4y + 4y = O(y^2) = O(s^2).$$

Finally, for any $s \geq 0$, we have

$$\mathcal{Z}_-(s) = \frac{\alpha}{\eta(1+\alpha s)} \leq \frac{\alpha}{\eta}.$$

To finish the proof, we apply Theorem 4.4.1 and see that the numerical solutions of both CM and FSM are positive. □

Theorem 4.4.3 (Consistency)**.** *GM* (4.4) *and BEM* (4.3) *are second-order consistent in space. That is, given a smooth solution $u(x,t)$ of the problem (P), a local truncation error $\tau_i(t)$ is $O(\Delta x^2)$ for*

$$\tau_i(t) = (1+\alpha u_i)u_{i,t} + [m(u_{i-1}, u_i)(1 + p_{i,\bar{x}})]_x.$$

Proof. Let us denote $u_i = u(i\Delta x, t)$ to simplify the notation. First, note that both GM and BEM have very similar formulations and satisfy Definition 4.3.1. Thus, we can use an approach similar to [ZB00]. After a Taylor expansion, we achieve

$$\begin{aligned} m(s_1, s_2) = m(s+\Delta s, s-\Delta s) &= m(s,s) + \frac{\partial m}{\partial s_1}(s,s)\Delta s - \frac{\partial m}{\partial s_2}(s,s)\Delta s + \beta(s)\Delta s^2 + O(\Delta s^2) \\ &= \mathcal{M}(s) + \beta(s)\Delta s^2 + O(\Delta s^2), \end{aligned}$$

where $s = \frac{s_1+s_2}{2}$, $\Delta s = \frac{s_1-s_2}{2}$, and

$$\beta(s) = \frac{1}{2}\left(\frac{\partial^2 m(s,s)}{\partial s_1^2} - 2\frac{\partial^2 m(s,s)}{\partial s_1 \partial s_2} + \frac{\partial^2 m(s,s)}{\partial s_2^2}\right).$$

We cancel out $O(\Delta s)$ terms by using the symmetry of $m(s_1, s_2)$, according to (b) from Definition 4.3.1. We also obtain

$$\begin{aligned} p_{i,\bar{x}} &= u_{i,\bar{x}x\bar{x}} - [\mathcal{Z}(u_i)]_{\bar{x}}\,, \\ u_{i,\bar{x}x\bar{x}} &= \frac{u_{i+1} - 3u_i + 3u_{-1} - u_{i-2}}{\Delta x^3} = u^{(3)}_{i-\frac{1}{2}} + \alpha(x_{i-\frac{1}{2}})\Delta x^2 + O(\Delta x^4), \\ [\mathcal{Z}(u_i)]_{\bar{x}} &= \mathcal{Z}'(u_{i-\frac{1}{2}})\frac{u_i - u_{i-1}}{\Delta x} + \mathcal{Z}''(u_{i-\frac{1}{2}})\frac{(u_i - u_{i-\frac{1}{2}})^2 - (u_{i-1} - u_{i-\frac{1}{2}})^2}{2\Delta x} + O(\Delta x^2) + O(\Delta x^4) \\ &= \mathcal{Z}'(u_{i-\frac{1}{2}})\left[u'_{i-\frac{1}{2}} + \frac{\Delta x^2}{24}u^{(3)}_{i-\frac{1}{2}} + O(\Delta x^4)\right] + \mathcal{Z}''(u_{i-1/2})\left[\frac{\Delta x^2}{8}u'_{i-\frac{1}{2}}u''_{i-\frac{1}{2}} + O(\Delta x^4)\right]. \end{aligned}$$

After simplification,

$$p_{i,\bar{x}} = u^{(3)}_{i-\frac{1}{2}} + \mathcal{Z}'(u_{i-\frac{1}{2}})u'_{i-\frac{1}{2}} + \gamma(x_{i-\frac{1}{2}})\Delta x^2 + O(\Delta x^4)$$

for some smooth function $\gamma(x)$. As a result,

$$\begin{aligned}
[m(u_{i-1},u_i)(1+p_{i,\bar{x}})]_x &= \frac{1}{\Delta x}\left[m(u_i,u_{i+1})(1+p_{i+1,\bar{x}}) - m(u_{i-1},u_i)(1+p_{i,\bar{x}})\right] \\
&= \frac{1}{\Delta x}\left\{\mathcal{M}\left(\frac{u_i+u_{i+1}}{2}\right) + \beta\left(\frac{u_i+u_{i+1}}{2}\right)\left(\frac{u_{i+1}-u_i}{2}\right)^2 + O(\Delta x^3)\right\} \\
&\quad \left\{1 + u^{(3)}_{i+\frac{1}{2}} + \mathcal{Z}'(u_{i+\frac{1}{2}})u'_{i+\frac{1}{2}} + \gamma(x_{i+\frac{1}{2}})\Delta x^2 + O(\Delta x^4)\right\} \\
&\quad - \frac{1}{\Delta x}\left\{\mathcal{M}\left(\frac{u_i+u_{i-1}}{2}\right) + \beta\left(\frac{u_i+u_{i-1}}{2}\right)\left(\frac{u_{i-1}-u_i}{2}\right)^2 + O(\Delta x^3)\right\} \\
&\quad \left\{1 + u^{(3)}_{i-\frac{1}{2}} + \mathcal{Z}'(u_{i-\frac{1}{2}})u'_{i-\frac{1}{2}} + \gamma(x_{i-\frac{1}{2}})\Delta x^2 + O(\Delta x^4)\right\}.
\end{aligned}$$

Note that for any continuously differentiable function, $g(s)$ is defined as

$$\begin{aligned}
g\left(\frac{u_i+u_{i+1}}{2}\right) &= g(u_{i+\frac{1}{2}}) + g'(u_{i+\frac{1}{2}})\frac{u''_{i+\frac{1}{2}}}{2}\left(\frac{\Delta x}{2}\right)^2 + O(\Delta x^4), \\
\left(\frac{u_{i+1}-u_i}{2}\right)^2 &= (u'_{i+\frac{1}{2}})^2\left(\frac{\Delta x}{2}\right)^2 + O(\Delta x^4).
\end{aligned}$$

The above properties can be applied to $\mathcal{M}(s)$ and $\beta(s)$. Hence we conclude

$$[m(u_{i-1},u_i)(1+p_{i,\bar{x}})]_x = \left[\mathcal{M}(u_i)(1+u^{(3)}_i - Z'(u_i)u'_i)\right]' + O(\Delta x^2).$$

□

4.5 Numerical simulation

In this section, we present numerical simulations based on the continuous time methods in Section 4.3 with a practical discrete-time adaptive time stepping method. We illustrate the benefit of using BEM over GM in a physically relevant setting in comparison to results from laboratory experiments. Throughout Section 4.5, we solve the problem (P) with the specific

functions,

$$\begin{aligned}
&\mathcal{M}(h) = \frac{h^3\phi(\alpha h)}{3\phi(\alpha)}, \quad \phi(X) = \frac{3}{16X^3}[(1+X)^4(4\log(1+X)-3)+4(1+X)^2-1], \\
&\mathcal{Z}_+(h) = -\frac{A_H}{h^3}, \quad \mathcal{Z}_-(h) = \frac{\alpha}{\eta(1+\alpha h)}.
\end{aligned} \tag{4.5}$$

This corresponds to the FSM in Ji et al. [JFS19] with $\lambda = 0$. In their work, setting $\lambda = 0$ matched the experimental data better than setting $\lambda > 0$. Thus, this is a good example to demonstrate our method on. The film stabilization term $\mathcal{Z}_+(h)$ takes the functional form of disjoining pressure, with A_H corresponding to the Hamaker constant. Increasing the value of A_H stabilizes the flow. The parameter η acts as a scaling parameter in the azimuthal curvature $\mathcal{Z}_-(h)$, and decreasing its value destabilizes the flow.

For each simulation, we use the functions in Equation (4.5) and dimensionless parameters α, η, A_H, and a dimensionless initial data $h_0(x)$ on domain $[0, L]$. In Section 4.5.1 and Section 4.5.3, we use dimensionless variables to compare the performance of the two numerical schemes. Whereas, in Section 4.5.2, the simulation is compared with experimental data, so the numerical results are converted back to a dimensional scale. The dimensionless parameters and the initial data are chosen to be in the range of physically meaningful values. Many times, we choose the initial data as a slightly perturbed constant state,

$$h_0(x) = \bar{h}(1 + 0.01\sin(\pi x/L)).$$

The initial condition represents the profile of a flat liquid film at the onset of the instability, where $\bar{h}$ is a critical flow parameter that governs the size, spacing, and frequency of the liquid beads, consequently having a strong influence on the flow regime [SZJ17].

4.5.1 Comparison of numerical methods

In this section, we compare the simulation of the BEM and GM in a physically relevant setting. We simulate the BEM and GM with the functions (4.5) with dimensionless parameters

$\alpha = 10.6$, $\eta = 0.223227$, $A_H = 0.001$. We choose the initial data as

$$h_0(x) = 1.471(1 + 0.01\sin(\pi x/L)),\ L = 24.0.$$

The numerical schemes presented in Section 4.4 are continuous in time. Thus, we must discretize the time step for the practical implementation. We discretize the continuous method (4.3) using the θ-weighted time-step method with $\theta = \frac{1}{2}$. This leads to the semi-implicit BEM method:

Bounded Entropy Method (Semi-Implicit BEM)**.**

$$\begin{aligned}
&\left(1 + \alpha\frac{u_i^{k+1} + u_i^k}{2}\right)\left(\frac{u_i^{k+1} - u_i^k}{\Delta t}\right) + [m(u_{i-1}^{k+1}, u_i^{k+1})(1 + p_{i,\bar{x}}^{k+1})]_x = 0,\\
&p_i^{k+1} = u_{i,\bar{x}x}^{k+1} - \mathcal{Z}_+(u_i^{k+1}) - \mathcal{Z}_-(u_i^k),\\
&u_i(0) = u_0(i\Delta x),\ i = 0, 1, 2, \cdots, N,\\
&m(s_1, s_2) = \begin{cases} \mathcal{M}(s_1) & \text{if } s_1 = s_2,\\ (s_2 - s_1)/\int_{s_1}^{s_2} \frac{1}{\mathcal{M}(s)} ds & \text{if } s_1 \neq s_2. \end{cases}
\end{aligned} \tag{4.6}$$

While other terms involving spatial differences, including $\mathcal{Z}_+$, are discretized implicitly, we note that $\mathcal{Z}_-$ is discretized explicitly. Such discretization is a well-known technique that increases the stability of a numerical method by treating a concave term and a convex term separately [GR01, Gru03]. One may employ a fully implicit method, but this typically requires Δt to be very small. We observe that the semi-implicit method is stable for larger time steps. When using the semi-implicit scheme, we accelerate the simulations by incorporating adaptive time stepping, as discussed in detail in Section 4.5.3. We also note that one has to numerically calculate $\int_{s_1}^{s_2} \frac{1}{\mathcal{M}(s)} ds$ while evaluating $m(s_1, s_2)$. We use the Simpson's method with 2-4 grids to numerically integrate $1/\mathcal{M}(h)$ on $[u_{i-2}, u_{i-1}], [u_{i-1}, u_i]$, and so on. Similarly, we discretize the continuous method (4.4) using the fully implicit time-stepping scheme in [JFS19].

We take $m(s_1, s_2) = \mathcal{M}\left(0.5(s_1 + s_2)\right)$, which satisfies Definition 4.3.1. The calculation of $m(s_1, s_2)$ for GM is relatively simple since it does not require numerical integration. As

mentioned before, GM is fully implicit so Δt needs to be well-controlled and kept small. Thus, when we compare the simulation of BEM (4.6) to GM (4.7) in Section 4.5.1-4.5.2, we use a fixed Δt unless the numerical method fails to converge in which case we decrease Δt by half. In Section 4.5.3, we show an example of BEM (4.6) implemented with the adaptive time stepping algorithm (see Algorithm 3) to demonstrate more efficient implementation. For both methods, we use Newton's method at each time step to solve discrete nonlinear equations (see Algorithm 1). The Newton's method returns `True` if it successfully solves for the numerical solution at the next time step within 15 iterations; otherwise, it returns `False`. When the Newton's method fails, we decrease Δt by 50% and try Newton's method again. The detailed procedure of the Newton's method with fixed time stepping is written in Algorithm 2.

The Newton's algorithm is specifically written for BEM (4.6), but setting $\mathbf{f}(\mathbf{u}^k)$ as the left side expression of the equality of equation (10) in Algorithm 1 results in the algorithm for GM (4.7). The function `NewtonMethod` has the input of the numerical solution at kth time step $\mathbf{u}^k$, the current time step Δt, and the tolerance value tol which determines the success or failure of the Newton's iteration. `NewtonMethod` returns `True` if $\|\mathbf{f}(\mathbf{u}^k)\|_\infty < tol$ after the for loop and updates the numerical solution by setting $\mathbf{u}^k = \mathbf{u}^{k+1}$. `NewtonMethod` gives a chance of 15 iteration, but in practice, we see that the method satisfies $\|\mathbf{f}(\mathbf{u}^k)\|_\infty < tol/10$ within 3-4 iteration. When $\|\mathbf{f}(\mathbf{u}^k)\|_\infty \geq tol$, `NewtonMethod` returns `False`.

In the case when `NewtonMethod` returns `False`, we decrease Δt by 50% and try `NewtonMethod` again with the same $\mathbf{u}^k$ and tol (see Algorithm 1 and Algorithm 3). The Algorithm 2 is used to generate Figure 4.2 and Figure 4.3. Notice that Δt is only decreased when `NewtonMethod` returns `False`. If `NewtonMethod` fails more than 4 consecutive times, we completely stop the simulation.

Algorithm 1: Newton's method for BEM

Input: numerical solution $\mathbf{u}^k$, the current time step Δt, and a tolerance value tol for the convergence success criteria.

Output: `True` or `False` depending on whether the method succeed or fail.

`NewtonMethod(`$\mathbf{u}^k$`,`Δt`,`tol`):`

$\mathbf{u}^{k+1} = \mathbf{u}^k$; `% Initial guess for the Newton's method`

for $i = 0$ **to** 15 **do**

  $\mathbf{f}(\mathbf{u}^k) =$ `the left side of the equality of equation` (4.6); `%` `Use` (4.7) `for GM`

  $\mathbf{u}^{k+1} = \mathbf{u}^k - (\nabla \mathbf{f}(\mathbf{u}^k))^{-1}\mathbf{f}(\mathbf{u}^k)$;

  if $\|\mathbf{f}(\mathbf{u}^k)\|_\infty < tol/10$ **then**
    `break;`

  end

end

if $\|\mathbf{f}(\mathbf{u}^k)\|_\infty < tol$ **then**
  return `True;`

else
  return `False;`

end

Algorithm 2: Simulation with fixed time stepping

Input: discrete initial data $\mathbf{u}^0$, the time step Δt, the end time t_{end}, and a tolerance value *tol* for the convergence success criteria.

Output: $\mathbf{u}^k$ at the t_{end} if the simulation succeeds. Otherwise outputs $\mathbf{u}^k$ at the time of the simulation failure.

`Simulate(`$\mathbf{u}^0$`,`Δt`,`t_{end}`):`

`set` $t = 0$`, bad = 0, and` $\mathbf{u}^k = \mathbf{u}^0$`;`

while $t < t_{end}$ **do**

  if *NewtonMethod(*$\mathbf{u}^k$*,* Δt*, tol) == True* **then**

    $t = t + \Delta t$; `% Update time`

    $\mathbf{u}^k = \mathbf{u}^{k+1}$; `% Update the numerical solution`

    `bad = 0;`

  else

    `bad = bad+1;`

    $\Delta t = \Delta t * 0.5$; `% Try the Newton's Method with smaller` Δt

    if $bad > 4$ **then**

      `exit(1);` `% Stop the simulation`

    end

  end

end

Generic Method (Implicit GM)**.**

$$\begin{aligned}
&\left(1+\alpha\frac{u_i^{k+1}+u_i^k}{2}\right)\left(\frac{u_i^{k+1}-u_i^k}{\Delta t}\right)+[m(u_{i-1}^{k+1},u_i^{k+1})(1+p_{i,\bar{x}}^{k+1})]_x=0,\\
&p_i^{k+1}=u_{i,\bar{x}x}^{k+1}-\mathcal{Z}_+(u_i^{k+1})-\mathcal{Z}_-(u_i^{k+1}),\\
&u_i(0)=u_0(i\Delta x),\ i=0,1,2,\cdots,N,\\
&m(s_1,s_2)=\begin{cases}\mathcal{M}(s_1) & \text{if } s_1=s_2,\\ \mathcal{M}\left(0.5(s_1+s_2)\right) & \text{if } s_1\neq s_2.\end{cases}
\end{aligned}\tag{4.7}$$

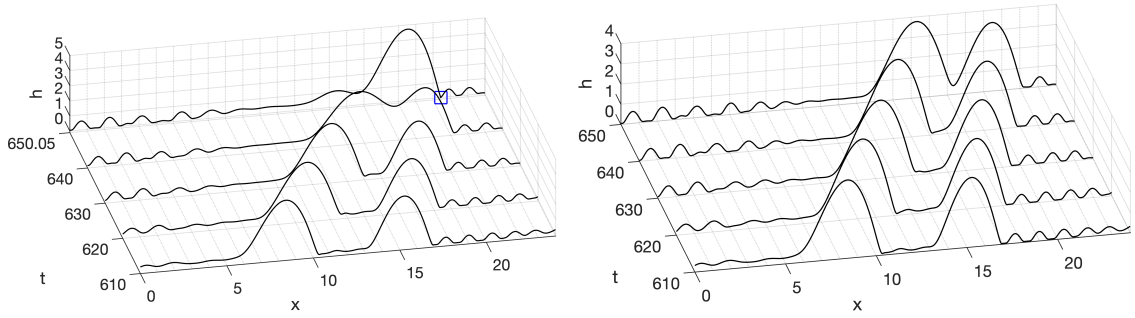

(a) GM (b) BEM

Figure 4.2: Simulation results with (a) the Generic Method (GM) from Equation (4.7) from $t = 610$ to $t = 650.05$ and (b) the Bounded Entropy Method (BEM) from Equation (4.6) from $t = 610$ to $t = 650$ on a coarse grid (3072 grid points on $[0, 24]$). The details of the simulation are described in Section 4.5.1. The plots illustrate the difference between the evolution profiles of traveling droplets as they merge. At $t = 640$, GM prematurely fuses two droplets while the BEM does not. Because of instabilities caused during the merging, GM develops negativity at $t = 650.05$, indicated by the blue square marker. The instability also causes the Newton's method (see Algorithm 1) to fail for GM at $t = 650$, so $\Delta t = 0.1$ is decreased by half $\Delta t = 0.05$. On the other hand, BEM can handle such instability and maintain the positivity of the film thickness while keeping the time step size $\Delta t = 0.1$.

Figure 4.2 and Figure 4.3 compare numerical simulations of GM (4.7) and BEM (4.6)

methods on a dimensionless domain $[0, 24]$. In Figure 4.2, one observes a classic evolution of isolated droplet dynamics where the bigger droplet collides with a smaller one and merges into one droplet as the solution propagates. Figure 4.3 is a closeup of the results from Figure 4.2 at the time of singularity. To generate Figure 4.2 and Figure 4.3, we simulate GM on a fine grid (6144 grid points on $[0, 24]$) until dimensionless time $t = 610$ with $\Delta t = 10^{-4}$ fixed. At this time $t = 610$, we extract the data corresponding to a coarse grid (3072 grid points on $[0, 24]$, which is twice the grid size of the fine grid) and set it as an initial condition for Figure 4.2 and Figure 4.3. From this time, we simulate BEM and GM on the coarse grid with fixed $\Delta t = 0.1$. Figure 4.2(a) illustrates the evolution of the simulation of GM while Figure 4.2(b) illustrates the evolution of the simulation of BEM. At $t = 650.05$ in Figure 4.2(a), one observes that the numerical solution becomes negative at one grid point in an underresolved mesh setting. Notice that Figure 4.2(a) has a singularity at $t = 650.05$ instead of $t = 650.0$ or $t = 650.1$ despite keeping $\Delta t = 0.1$ fixed. This is because, at $t = 650$, the Newton's method for GM fails. As a consequence, the time steps $\Delta t = 0.1$ is decreased by half, $\Delta t = 0.05$ (see Algorithm 2 in Section 4.5. The Newton's method succeeds after decreasing the time step by half, yet the recovered solution has a negative h value. On the other hand, BEM successfully maintains positivity throughout the dynamics.

In Figure 4.3, one observes the detailed profile of each simulation at the time of the numerical singularity. We continue the simulation in Figure 4.2 until $t = 654$. Note that we observe the numerical singularity on the coarse GM (4.7) simulation at $t = 650.05$ for the first time. The coarse GM simulation continues to have a negative value in contrast to the coarse BEM (4.6) simulation, which stays positive. Having a singularity is critical since it often prevents further numerical simulation and provides inaccurate results. It is also unphysical because no finite time rupture is observed in the experiment. Such numerical singularities are commonly observed with GM method in this dynamic regime of the simulation. The details of the fixed time closeup are described in the caption of Figure 4.3. One can see that the singularity affects the shape of the solution making the numerical prediction inaccurate. Let

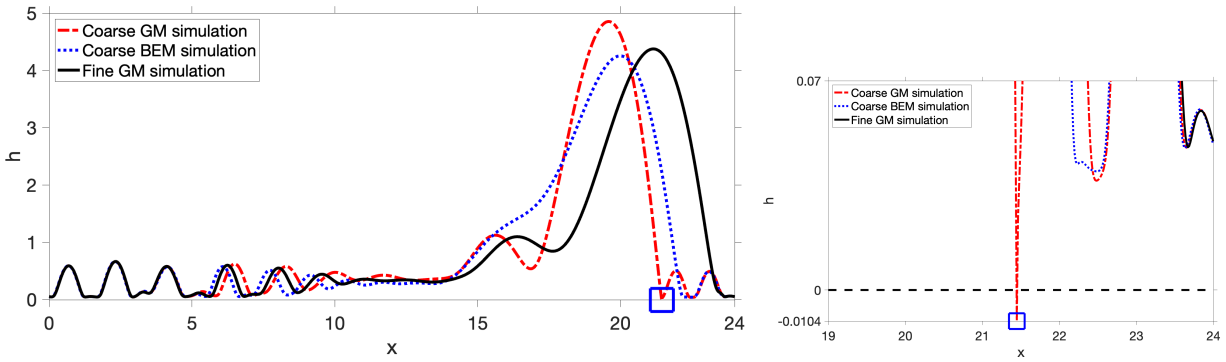

(a) Simulation comparison (b) Simulation comparison (enlarged)

Figure 4.3: Closeup of a coarse grid simulation (3072 points on $[0, 24]$) around $t = 654$. The details of the simulation are described in Section 4.5.1. The coarse GM simulation is taken at $t = 654.45$, the coarse BEM simulation is taken at $t = 654.40$, and the fine GM simulation is taken at $t = 654.41$. Figure 4.3(a) represents the full profile, and Figure 4.3(b) represents the closeup profile near the singularity. Note that h of the coarse GM simulation goes below the zero line indicated in dashed black at $t = 654.4500$, whereas the coarse BEM simulation does not go below the zero line at $t = 654.400$. The fine GM simulation uses twice as many grid points (6144 grid points on $[0, 24]$) and is captured at $t = 654.4100$. Besides the phase shift, the coarse BEM simulation agrees better with the fine GM simulation in a sense that the average l_2 error (l_2 error $= 2.0116$) across the domain is lower than the average l_2 error caused by the coarse GM simulation (l_2 error $= 2.5999$). The average l_2 error was calculated by Equation (4.8).

us take a closer look at the downstream and upstream profile of the droplet in Figure 4.3. We see that the coarse BEM (4.6) simulation has more smoothness downstream of the droplet (from $x = 23$ to $x = 24$), whereas GM (4.7) simulation has a finite time pinchoff (marked by a blue square). We also see that BEM's wavy pattern at the upstream matches better with the experiment than GM's (from $x = 0$ to $x = 15$). Furthermore, the coarse BEM simulation has a lower average l_2 error (l_2 error $= 2.0116$) than the error caused by the coarse GM simulation (l_2 error $= 2.5999$) despite using different schemes. Here, we define the average l_2

error as

$$l_2 \,\text{error} = \frac{1}{L}\sum_i (u_i - u_i^*)^2, \tag{4.8}$$

where u_i is the simulation results on the coarse grid and u_i^* is the simulation result on the fine grid at the corresponding points of the coarse grid.

4.5.2 Comparison with laboratory experiments

Here we compare predictions from our method with the experimental data. In the experiment, the coating flow is created by injecting fluid into the nozzle with an inner diameter of 0.8 mm using a programmable syringe pump. We use Rhodorsil silicone oil v50, which is a well-wetting liquid with the density $\rho = 963$ kg/m^3, kinematic viscosity $\nu = 50$ mm^2/s, and surface tension $\sigma = 20.8$ mN/m at $20°C$. The corresponding capillary length $l_c = 1.5$ mm. The fluid flows along a 0.6 m-long Nylon string that is hung vertically. The radius of the Nylon string is 0.1 mm. A high-speed camera captures the flow at a frame rate of 1000 frames/second. We estimate the measurement uncertainty in the liquid bead radius and length to be approximately $\pm$ 0.08 mm, and that in the liquid bead spacing approximately $\pm$ 0.3 mm. Further details of our experimental setup, procedure, and data analysis can be found in a previous publication [SZJ17].

We consider two cases: the Rayleigh-Plateau case and the isolated droplet case. We do not consider the convective regime because it requires different boundary conditions. For the first case, we let the flow rate be 0.08 g/s for a fiber with a radius of 0.1 mm and a nozzle inner diameter (nozzle ID) of 0.8 mm. The experiments and corresponding numerical method both exhibit the Rayleigh-Plateau regime (see Figure 4.4). For the second case, we let the flow rate be 0.006 g/s for the same fiber. For these parameters, one observes the isolated droplet regime (see Figure 4.5).

The experimentally obtained images are processed and segmented by the built-in methods in MATLAB, where we have incorporated the Canny method and Otsu's method. By processing

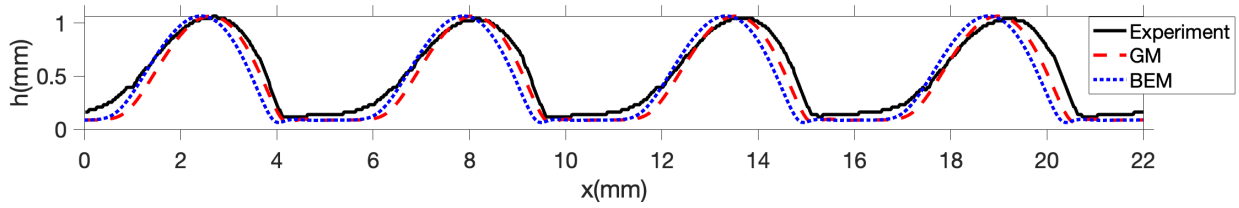

Figure 4.4: Comparison between laboratory experimental data and simulation data of the numerical methods. The details of the simulation and laboratory data acquisition are described in Section 4.5.2. GM (4.7) and BEM (4.6) are simulated with a fine grid (1000 grid points on the domain $[0, 5]$) and then shifted horizontally to match the phase. The experimental profile (indicated by the solid black line) follows the Rayleigh-Plateau regime extracted from an experiment conducted with a flow rate of 0.08 g/s, a fiber radius of 0.1 mm, and a nozzle ID of 0.8 mm.

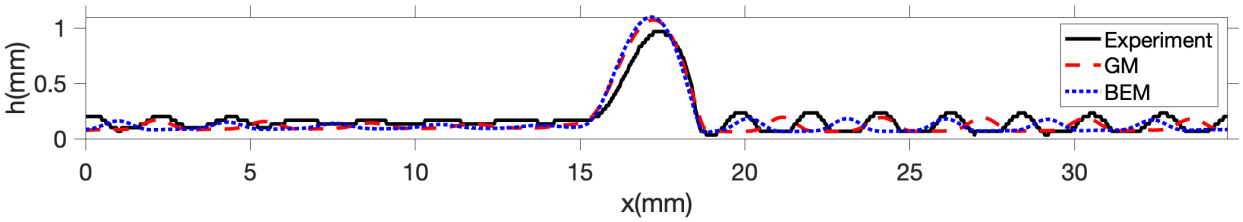

Figure 4.5: Comparison between laboratory experimental data and simulation data of the numerical methods. The details of the simulation and laboratory data acquisition are described in Section 4.5.2. GM (4.7) and BEM (4.6) are simulated with a relatively coarse grid (1999 grid points on the domain $[0, 39.338]$) and then shifted horizontally to match the phase. The experimental profile (indicated by the black solid line) follows the isolated droplet regime extracted from an experiment conducted with a flow rate of 0.06 g/s, a fiber radius of 0.1 mm, and a nozzle ID of 0.8 mm.

high-resolution optical images and using other experimental values such as the flow rate, fiber radius, the density of the fluid ρ, and the kinematic viscosity ν, we obtain a characteristic length scale h_N and the estimated period L of traveling beads. Using these values, one can calculate dimensionless parameters α, η, and nondimensional scaling constants. We must

perform this task for each experimental case since the resulting parameters are different. To generate Figure 4.4 and Figure 4.5, we simulate GM (4.7) and BEM (4.6) on a dimensionless domain and scale back to dimensional data to compare with the experimental data.

Figure 4.4 illustrates the simulation results of GM (4.7) and BEM (4.6) compared with the experimental data of the Rayleigh-Plateau regime. We simulate GM and BEM with the functions (4.5) with corresponding $\alpha = 5.8856$ and $\eta = 0.2912$ with a stabilizing parameter chosen to be $A_H = 10^{-11}$. We choose the initial data as a slightly perturbed constant state

$$h_0(x) = \bar{h}(1 + 0.01\sin(\pi x/L)),\ L = 5.0,\ \bar{h} = 0.9568.$$

Note that the stabilizing parameter A_H is relatively small compared to η or α or the average film thickness $\bar{h}$. We simulate GM and BEM on a fine grid until dimensionless time $t = 250.006$ with an adaptive time stepping method (see Algorithm 3) where $10^{-3} \leq \Delta t \leq 10^{-2}$. The adaptive time stepping was used to expedite the simulation process, but we made sure the $\max \Delta t$ is small enough for an accurate simulation (i.e., one results in the almost identical simulation if we keep $\Delta t = 10^{-4}$, fixed). After the simulation, we dimensionalize the data by multiplying scaling constants with respect to space and time. One can see that the three simulations match well despite the fact that both GM and BEM slightly underpredict the bead traveling speed as they go further along the x-direction.

Figure 4.5 illustrates the simulation results of GM (4.7) and BEM (4.6) compared with the experimental data of the isolated droplet regime. We simulate GM and BEM with Equation (4.5) with corresponding $\alpha = 3.092621559$ and $\eta = 0.123$ with a stabilizing parameter chosen to be $A_H = 4.0 \times 10^{-2}$. Note that the stabilizing parameter A_H is bigger than the value we choose to simulate the Rayleigh-Plateau regime. We have simulated GM and BEM with a slightly perturbed constant state condition as the initial data, but the simulation has resulted in a dramatically different and unphysical profile from the experimental data. We expect this to be natural because the profile of the isolated droplet regime is inherently more complex than the Rayleigh-Plateau regime. We expect that there are several different steady states, and it may depend on the initial data intricately. Therefore, we extract

the initial condition from the experiment and use an interpolating sine series to find the best-fitting smooth function. We enforce a periodic boundary condition by cropping the data appropriately so that the h_0 at $x = 0$ matches h_0 at $x = L$. After cropping, we use a moving average filter to smooth data even further. The code implementation details are published in a GitHub repository. After acquiring the initial data, we simulate GM and BEM on a fine grid until dimensionless time $t = 807.107$ for GM and $t = 827.8070$ for BEM with an adaptive time stepping method (see Algorithm 3) where $10^{-3} \leq \Delta t \leq 10^{-2}$. The adaptive time stepping is used to expedite the simulation process again. Similar to the Rayleigh-Plateau simulation, we dimensionalize the data by multiplying scaling constants with respect to space and time. One can see that both simulations predict the width of the droplet well with slight overprediction of the height of the droplet. We note that BEM describes the pinchoff behavior downstream of the bead better (from $x = 18mm$ to $x = 20mm$) than GM since GM is nearly flat in this region (from $x = 18mm$ to $x = 20mm$) in Figure 4.5.

4.5.3 Adaptive time stepping method

Adaptive time stepping can optimize the performance of the numerical method while still accurately capturing the droplet propagation. In the early stage of the computation, we expect to see a lot of change in the shape of the graph. Therefore, one wishes to keep the time step very small to capture the accurate profile of the solution. However, as the computation progress, the algorithm approaches a nearly steady state. It becomes costly to implement a small time step calculation for many iterations, while such a small step iteration does not contribute much to the change of the profile or the phase. Here we use an adaptive time stepping method (see Algorithm 3) motivated by the method in [KB13, BBD94].

The main idea is to use a dimensionless local truncation error for every time step and see if it surpasses a tolerance value that we impose. This choice of adaptive method was inspired by similar ideas in [BBD94, KB13]. We define the dimensionless local truncation error using

the following formula,

$$LTE(t^{k+1})_i = \left| e_i^{k+1} - \frac{\Delta t}{\Delta t_{old}} e_i^k \right|,$$

for

$$e_i^{k+1} = \frac{u_i^{k+1} - u_i^k}{u_i^k},\ e_i^k = \frac{u_i^k - u_i^{k-1}}{u_i^{k-1}},\ \Delta t = t^{k+1} - t^k,\ \Delta t_{old} = t^k - t^{k-1}.$$

The details of the entire algorithm are given by Algorithm 3. Note that we store information from the previous timestep $\mathbf{u}^{k-1}$ to calculate $\mathbf{LTE}(t^{k+1})$. If one successfully calculates $\mathbf{u}^{k+1}$ with the Newton's method, we increase our time step by 1%, calculate $\mathbf{LTE}(t^{k+1})$, and check $||\mathbf{LTE}(t^{k+1})||_\infty < tol_1$. If $||\mathbf{LTE}(t^{k+1})||_\infty < tol_1$ more than `countMax` times (in our case, we let `countMax` $= 3$ throughout Section 4.5.3), we increase our time step by 20%. To speed up the simulation even further, one may increase the percentage to a higher value while the time step reduces by half if the Newton's method fails. If the error is bigger than tol_1, we proceed to calculate the next time step. In the case when the Newton's method fails, we decrease our time step by 50% and try the Newton's method again.

4.5.3.1 Adaptive time stepping example without a near singular behavior

We simulate the semi-implicit BEM (4.6) with the functions (4.5), and dimensionless parameters $\alpha = 5.0$, $\eta = 0.02$, $A_H = 10^{-5}$. We choose the initial data as

$$h_0(x) = 0.95(1 + 0.01\sin(\pi x/L)),\ L = 1.0,$$

and use 100 grid points on [0,1]. We start with initial $\Delta t = 10^{-3}$ and use Algorithm 3 to increase Δt until $t = 1.0$ with $tol_1 = 10^{-1}$ and `countMax` $= 3$. Figure 4.6 illustrates the increase of Δt throughout the simulation when η is relatively high and the stabilizing parameter A_H is relatively high. Because the parameters are selected to simulate a relatively stable coating flow, the $||\mathbf{LTE}(t^{k+1})||_\infty < tol_1$ condition is satisfied whenever the Newton's method succeeds. Thus, every third-time step (note that `countMax` $= 3$), Δt increases by 20%.

Algorithm 3: Adaptive time stepping method

Input: discrete initial data $\mathbf{u}^0$, time step Δt, final time t_{end}, an adaptive time tolerance value tol_1, the maximum number of count `countMax`.

Output: $\mathbf{u}^k$ at the t_{end} if the simulation succeeds. Otherwise outputs $\mathbf{u}^k$ at the time of the simulation failure.

`SimulateAdaptive(`$\mathbf{u}^0, \Delta t, t_{end}$`):`

`set` $t = 0$`, bad = 0, count = 0, and` $\mathbf{u}^k = \mathbf{u}^0$`;`

while $t < t_{end}$ **do**

  if *NewtonMethod(*$\mathbf{u}^k, \Delta t, tol_1$*) == True* **then**

    $t = t + \Delta t, \mathbf{u}^k = \mathbf{u}^{k+1}$; `% Update time and solution`

    $\Delta t = \Delta t * 1.01$; `% Increase` Δt `by 1%`

    `calculate` $\mathbf{e}^{k+1}, \mathbf{e}^k$`, and` $\mathbf{LTE}(t^{k+1})$`;`

    if $\|\mathbf{LTE}(t^{k+1})\|_\infty < tol_1$ **then**

      `count=count+1;`

      if $count =$ *countMax* **then**

        $\Delta t = \Delta t * 1.2$; `% Increase` Δt `by 20%`

        `count = 0;`

      end

    end

  else

    `bad = bad+1;`

    $\Delta t = \Delta t * 0.5$; `% Try the Newton's Method with smaller` Δt

    if $bad > 4$ **then**

      `exit(1);` `% Stop the simulation`

    end

  end

end

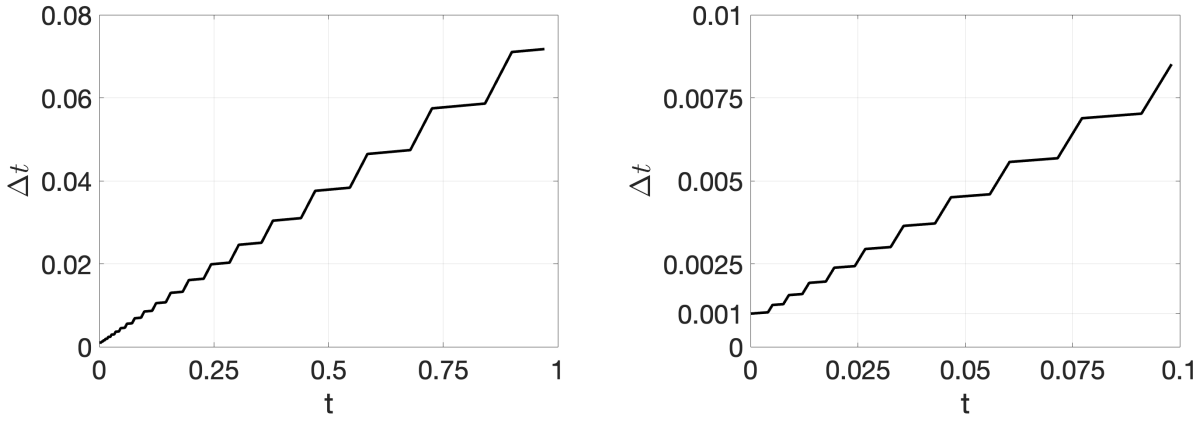

(a) Δt over simulation

(b) Δt over simulation (enlarged)

Figure 4.6: Plots of Δt for the simulation described in Section 4.5.3.1 for $0 < t < 1$. Newton's iteration always succeeds, so Δt continuously increases by 1% every time while an additional increase of 20% (20 times in total) occurs every third time. The image on the right shows a closeup of the early time interval from $t = 0$ to $t = 0.1$.

4.5.3.2 Adaptive time stepping example with a near singular behavior

We simulate the semi-implicit BEM (4.6) with the functions (4.5), and dimensionless parameters $\alpha = 5.0$, $\eta = 0.005$, $A_H = 0$. We choose the initial data as

$$h_0(x) = 0.95(1 + 0.01\sin(\pi x/L)),\ L = 1.0,$$

and use 100 grid points on [0,1]. We start with initial $\Delta t = 10^{-3}$ and use Algorithm 3 to increase Δt until $t = 1.0$ with $tol_1 = 10^{-1}$ and `countMax` $= 3$ again. Since we set the stabilizing parameter $A_H = 0$ and take a lower η value, we observe a singular behavior of the simulated flow (see Figure 4.8). Figure 4.7 illustrates the increase of Δt throughout the simulation when there is a singular behavior. Unlike Figure 4.6, the $||\mathbf{LTE}(t^{k+1})||_\infty \geq tol_1$ from $t = 0.045228$ to $t = 0.0918907$. In this region, Δt is increased by 1% to carefully handle the transition of droplet dynamics (see Figure 4.8).

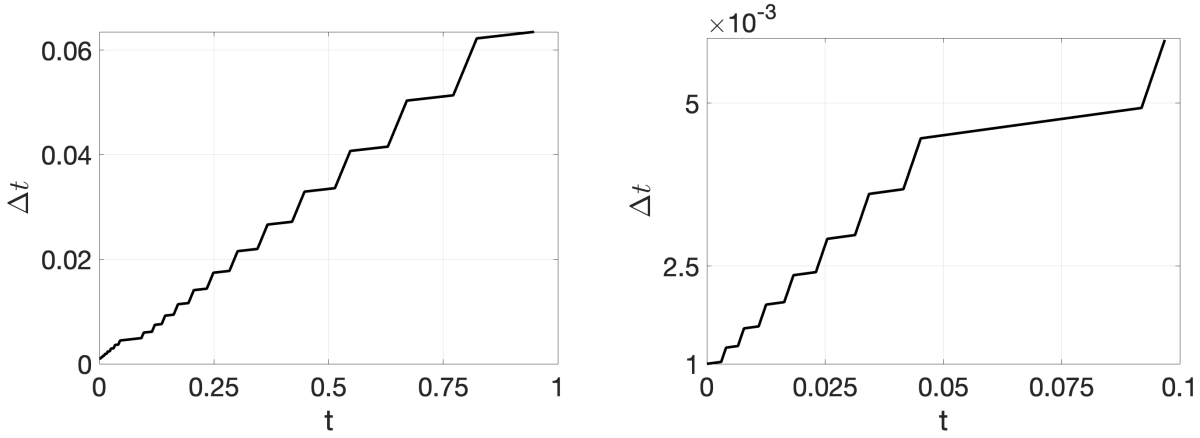

(a) Δt over simulation

(b) Δt over simulation (enlarged)

Figure 4.7: Plots of Δt for the simulation described in Section 4.5.3.2 for $0 < t < 1$. Newton's iteration always succeeds, so Δt continuously increases by 1% every time. However, unlike Figure 4.6, an additional 20% increase occurs irregularly. In fact, from $t = 0.045228$ to $t = 0.0918907$, Δt does not increase. The image on the right shows a closeup of the early time interval from $t = 0$ to $t = 0.1$.

4.5.3.3 Computational efficiency and accuracy

In this section, we demonstrate the computational efficiency of our method BEM over GM. We simulate semi-implicit BEM (4.6) and implicit GM (4.7) with the functions (4.5), and dimensionless parameters $\alpha = 5.0$, $\eta = 0.005$, $A_H = 0$. We choose the initial data as

$$h_0(x) = 0.45(1 + 0.01\sin(\pi x/L)),\ L = 1.0,$$

and record the CPU time of each method on three different grid sizes. Note that this is a similar setting as the simulation run in Section 4.5.3.2. When we use the fixed time stepping (see Algorithm 2 in Section 4.5) for BEM and GM, we let $\Delta t = 10^{-3}$. When we use the adaptive time stepping, which is only used for BEM, we use Algorithm 3 with initial $\Delta t = 10^{-3}$, $tol_1 = 10^{-3}$, and `countMax` $= 3$. Each GM simulation is run until the numerical solution fails to preserve positivity, resulting in different termination times. On the

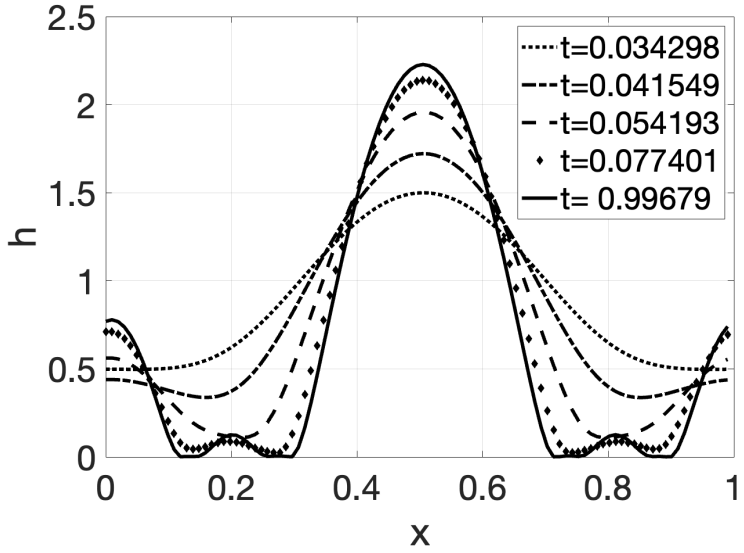

Figure 4.8: Evolution of a flow with a singular behavior described in Section 4.5.3.2. All of the plots have $h \geq 6.0942 \times 10^{-4}$.

other hand, each BEM always preserves the positivity of the numerical solution regardless of using any time stepping method so that it can be run until any time. For a fair CPU time comparison, we run BEM until GM fails with the respective grid sizes. By examining Table 4.1, one may notice the computational benefits of using adaptive time stepping with increased grid points.

	Time stepping	Positivity	CPU time
GM with $\Delta x = 0.01$	Fixed	Fails at $t = 0.299$	$0.286s$ until $t = 0.299$
BEM with $\Delta x = 0.01$	Fixed	Success	$0.374s$ until $t = 0.299$
BEM with $\Delta x = 0.01$	Adaptive	Success	$0.317s$ until $t = 0.299$
GM with $\Delta x = 0.005$	Fixed	Fails at $t = 1.09594$	$0.602s$ until $t = 1.09594$
BEM with $\Delta x = 0.005$	Fixed	Success	$1.08s$ until $t = 1.096$
BEM with $\Delta x = 0.005$	Adaptive	Success	$0.412s$ until $t = 1.09678$
GM with $\Delta x = 0.0025$	Fixed	Fails at $t = 3.4765$	$2.959s$ until $t = 3.4765$
BEM with $\Delta x = 0.0025$	Fixed	Success	$4.727s$ until $t = 3.477$
BEM with $\Delta x = 0.0025$	Adaptive	Success	$0.724s$ until $t = 3.51201$

Table 4.1: Computational cost comparison of BEM and GM for the example discussed in Section 4.5.3.3.

CHAPTER 5

Conclusion and future work

Numerical methods for simulating thin liquid films have been extensively studied over several decades [BBG98, ZB00, GR00, GR01]. Carefully simulating the dynamics of the fluid at the solid-liquid interface remains a challenging task and is still an active area of research [ZXR22, BSW22, DPM18, AN17]. As emphasized throughout the thesis, the intrinsic positivity property of the liquid film is essential at the discrete level of the numerical solution; it ensures that the solutions are physical and practical for various scientific and engineering applications.

Numerous articles in the literature present numerical simulation of the fiber coating problem [JFS19, JSJ20, JFS21, ZZS23, NO09, BRK14, JD22], and a considerable amount of work has been put into designing mathematical models [JFS19, JFS21, JSJ20, JD22, ZZS23]. However, less work has been done to design numerical methods for this geometry. Designing a numerical method requires careful attention due to the complexity of the solution, which involves the effects of cylindrical geometry, disjoining pressure, and stabilizing and destabilizing intermolecular forces. This thesis addresses the gap between state of the art numerical methods for thin films in simple geometries and numerical methods for fiber coating.

In this thesis, we introduce a positivity-preserving finite difference method for the problem of fiber-coating a vertical cylindrical fiber. While the prior state-of-the-art method (GM) achieves close agreement with experiments and successfully captures regime transitions, it struggles to match the flow profiles as the film thickness becomes small. In particular, the GM needs significant grid refinement to resolve very thin films without an artificial numerical

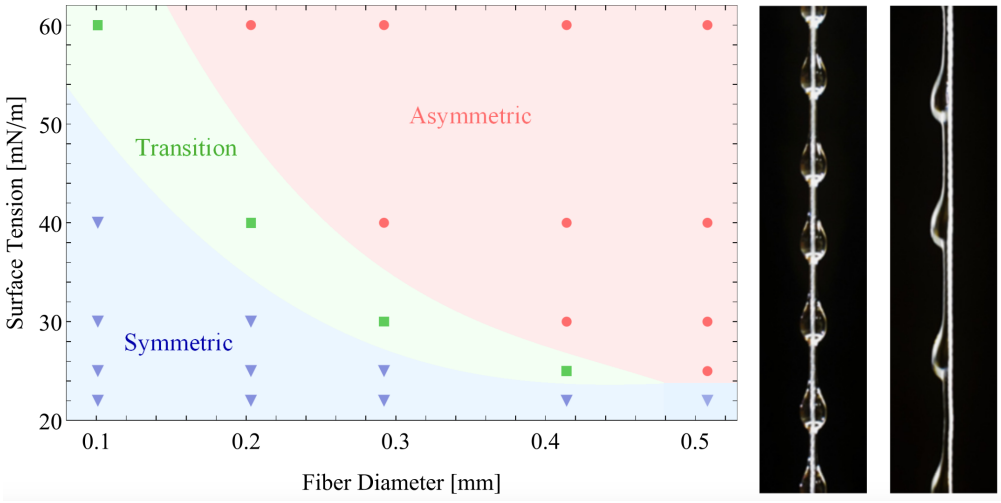

Figure 5.1: Left: Phase diagram of the bead morphology depending on surface tension and fiber diameters. Middle: Bead symmetry observed in a laboratory experiment. Right: Bead asymmetry observed in a laboratory experiment. Reprinted figure with permission from Gabbard & Bostwick [GB21]. Copyright (2021) by the American Physical Society, `https://doi.org/10.1103/PhysRevFluids.6.034005`.

singularity. We prove that our BEM preserves positivity given $\mathcal{M}(h) = O(h^n)$ for $n \geq 2$ and, furthermore, that there exists a lower bound independent of grid size given an a posteriori Lipschitz bound on the solution (something that has always been observed in experiments). By constructing a generalized entropy estimate, we extend the idea of positivity-preserving methods for basic lubrication equations to the problem involving cylindrical geometry, gravity, and nonlinear pressure. This technique has promise for thin liquid film equations with complex geometry, advection effect, and other surface tension effects.

There are a number of directions one can pursue from this work. One obvious direction is to prove the convergence of the BEM. Such work would benefit from additional regularity and positive results for the continuum of PDE. Another direction is to generalize the method to the fully 2D fiber coating problem, for example, using ADI methods such as [WB03] or considering more general geometries as in [GBS06]. Gabbard & Bostwick observed that the

asymmetric behavior of the traveling bead depends on the fiber radius and surface tension of the flow (see Figure 5.1) [GB21]. Thus, incorporating this behavior in a higher-dimensional model will be meaningful. In order to extend our method to higher dimensional cases, additional a posteriori assumptions on numerical and analytical solutions must be made. Finally, it would be interesting to consider other types of boundary conditions since the experiment is not periodic in space. The boundary conditions on an inlet and an outlet of the flow can change if other models are considered, such as one that includes a nozzle geometry [JSJ20] or a thermal effect [JFS21].

REFERENCES

[AB20] T. Alazard and D. Bresch. "Functional inequalities and strong Lyapunov functionals for free surface flows in fluid dynamics." *arXiv:2004.03440 [math.AP]*, 2020.

[AGS10] V. S. Ajaev, T. Gambaryan-Roisman, and P. Stephan. "Static and dynamic contact angles of evaporating liquids on heated surfaces." *Journal of Colloid and Interface Science*, **342**(2):550–558, 2010.

[AH97] S. Akter and M. S. J. Hashmi. "High speed nylon coating of wire using a plasto-hydrodynamic pressure unit." *Journal of Materials Processing Technology*, **63**(1-3):453–457, 1997.

[AHM02] V. S. Ajaev, G. M. Homsy, and S. J. S. Morris. "Dynamic response of geometrically constrained vapor bubbles." *Journal of Colloid and Interface Science*, **254**(2):346–354, 2002.

[Aja04] V. S. Ajaev. "Viscous flow of a volatile liquid on an inclined heated surface." *Journal of Colloid and Interface Science*, **280**(1):165–173, 2004.

[AK09] A. Atena and M. Khenner. "Thermocapillary effects in driven dewetting and self assembly of pulsed-laser-irradiated metallic films." *Physical Review B*, **80**(7):075402, 2009.

[AN17] A. Alharbi and S. Naire. "An adaptive moving mesh method for thin film flow equations with surface tension." *Journal of Computational and Applied Mathematics*, **319**:365–384, 2017.

[AR04] N. Alleborn and H. Raszillier. "Spreading and sorption of a droplet on a porous substrate." *Chemical Engineering Science*, **59**(10):2071–2088, 2004.

[AW03] V. S. Ajaev and D. A. Willis. "Thermocapillary flow and rupture in films of molten metal on a substrate." *Physics of Fluids*, **15**(10):3144–3150, 2003.

[Bat67] G. K. Batchelor. *An introduction to fluid dynamics*. Cambridge University Press, 1967.

[BB02] A. L. Bertozzi and M. Bowen. "Thin film dynamics: theory and applications." In *Modern Methods in Scientific Computing and Applications*, pp. 31–79. Springer, Dordrecht, 2002.

[BB04] J. W. Barrett and J. F. Blowey. "Finite element approximation of a nonlinear cross-diffusion population model." *Numerische Mathematik*, **98**(2):195–221, 2004.

[BBD94] A. L. Bertozzi, M. P. Brenner, T. F. Dupont, and L. P. Kadanoff. "Singularities and similarities in interface flows." In *Trends and Perspectives in Applied Mathematics*, pp. 155–208. Springer New York, 1994.

[BBG98] J. W. Barrett, J. F. Blowey, and H. Garcke. "Finite element approximation of a fourth order nonlinear degenerate parabolic equation." *Numerische Mathematik*, **80**(4):525–556, 1998.

[BBG01] J. W. Barrett, J. F. Blowey, and H. Garcke. "On fully practical finite element approximations of degenerate Cahn-Hilliard systems." *ESAIM: Mathematical Modelling and Numerical Analysis*, **35**(4):713–748, 2001.

[BBW98] A. J. Bernoff, A. L. Bertozzi, and T. P. Witelski. "Axisymmetric surface diffusion: Dynamics and stability of self-similar pinchoff." *Journal of Statistical Physics*, **93**:725–776, 1998.

[BC12] M. Bruna and S. J. Chapman. "Diffusion of multiple species with excluded-volume effects." *The Journal of Chemical Physics*, **137**(20):204116, 2012.

[BCO01] M. Bertalmío, L.-T. Cheng, S. Osher, and G. Sapiro. "Variational problems and partial differential equations on implicit surfaces." *Journal of Computational Physics*, **174**(2):759–780, 2001.

[BEI09] D. Bonn, J. Eggers, J. Indekeu, J. Meunier, and E. Rolley. "Wetting and spreading." *Reviews of Modern Physics*, **81**(2):739, 2009.

[BEJ14] M. Bukal, E. Emmrich, and A. Jüngel. "Entropy-stable and entropy-dissipative approximations of a fourth-order quantum diffusion equation." *Numerische Mathematik*, **127**(2):365–396, 2014.

[Ber95a] F. Bernis. *Viscous flows, fourth order nonlinear degenerate parabolic equations and singular elliptic problems*, pp. 40–56. Free Boundary Problems: Theory and Applications, Pitman Research Notes in Mathematics Series 323, Longman House, London, J. I. Diaz, M. Herrero, A. Linan, J. L. Vazquez, eds. 1995a.

[Ber95b] A. L. Bertozzi. *Loss and gain of regularity in a lubrication equation for thin viscous films*, pp. 72–85. Free Boundary Problems: Theory and Applications, Pitman Research Notes in Mathematics Series 323, Longman House, London, J. I. Diaz, M. Herrero, A. Linan, J. L. Vazquez, eds. 1995b.

[Ber96a] F. Bernis. *Integral inequalities with applications to nonlinear degenerate parabolic equations*, pp. 57–65. Nonlinear Problems in Applied Mathematics. SIAM, Philadelphia, 1996a.

[Ber96b] A. L. Bertozzi. "Symmetric singularity formation in lubrication-type equations for interface motion." *SIAM Journal on Applied Mathematics*, **56**(3):681–714, 1996b.

[BF90] F. Bernis and A. Friedman. "Higher order nonlinear degenerate parabolic equations." *Journal of Differential Equations*, **83**(1):179–206, 1990.

[BF03] R. J. Braun and A. D. Fitt. "Modelling drainage of the precorneal tear film after a blink." *Mathematical Medicine and Biology*, **20**(1):1–28, 2003.

[BG04] A. L. Bertozzi and J. B. Greer. "Low-curvature image simplifiers: Global regularity of smooth solutions and Laplacian limiting schemes." *Communications on Pure and Applied Mathematics Sciences*, **57**(6):764–790, 2004.

[BGL02] J. Becker, G. Grün, M. Lenz, and M. Rumpf. "Numerical methods for fourth order nonlinear degenerate diffusion problems." *Applications of Mathematics*, **47**(6):517–543, 2002.

[BGS03] J. Becker, G. Grün, R. Seemann, H. Mantz, K. Jacobs, K. R. Mecke, and R. Blossey. "Complex dewetting scenarios captured by thin-film models." *Nature Materials*, **2**(1):59–63, 2003.

[BGW01] A. L. Bertozzi, G. Grün, and T. P. Witelski. "Dewetting films: bifurcations and concentrations." *Nonlinearity*, **14**(6):1569, 2001.

[BKO93] S. Boatto, L. P. Kadanoff, and P. Olla. "Traveling-wave solutions to thin-film equations." *Physical Review E*, **48**(6):4423, 1993.

[BN04] J. W. Barrett and R. Nürnberg. "Convergence of a finite element approximation of surfactant spreading on a thin film in the presence of van der Waals forces." *IMA Journal of Numerical Analysis*, **24**(2):323–363, 2004.

[BP94] A. L. Bertozzi and M. Pugh. "The lubrication approximation for thin viscous films: the moving contact line with a 'porous media' cut-off of van der Waals interactions." *Nonlinearity*, **7**(6):1535, 1994.

[BP96] A. L. Bertozzi and M. Pugh. "The lubrication approximation for thin viscous films: Regularity and long-time behavior of weak solutions." *Communications on Pure and Applied Mathematics*, **49**(2):85–123, 1996.

[BPW92] F. Bernis, L. A. Peletier, and S. M. Williams. "Source type solutions of a fourth order nonlinear degenerate parabolic equation." *Nonlinear Analysis: Theory, Methods and Applications*, **18**(3):217–234, 1992.

[Bra12] R. J. Braun. "Dynamics of the tear film." *Annual Review of Fluid Mechanics*, **44**:267–297, 2012.

[Bre61] F. P. Bretherton. "The motion of long bubbles in tubes." *Journal of Fluid Mechanics*, **10**(2):166–188, 1961.

[BRK14] M. Binz, W. Rohlfs, and R. Kneer. "Direct numerical simulations of a thin liquid film coating an axially oscillating cylindrical surface." *Fluid Dynamics Research*, **46**(4):041402, 2014.

[BSR13] M. Benzaquen, T. Salez, and E. Raphaël. "Intermediate asymptotics of the capillary-driven thin-film equation." *The European Physical Journal E*, **36**(8):82, 2013.

[BSW22] V. Bogdanov, F. S. Schranner, J. M. Winter, S. Adami, and N. A. Adams. "A level-set-based sharp-interface method for moving contact lines." *Journal of Computational Physics*, **467**:111445, 2022.

[BT07] J. C. Burton and P. Taborek. "Two-dimensional inviscid pinch-off: An example of self-similarity of the second kind." *Physics of Fluids*, **19**(10):102109, 2007.

[CD99] H.-C. Chang and E. A. Demekhin. "Mechanism for drop formation on a coated vertical fibre." *Journal of Fluid Mechanics*, **380**:233–255, 1999.

[CDL18] Y. Chao, Z. Ding, and R. Liu. "Dynamics of thin liquid films flowing down the uniformly heated/cooled cylinder with wall slippage." *Chemical Engineering Science*, **175**:354–364, 2018.

[CGR17] P. Colli, G. Gilardi, E. Rocca, and J. Sprekels. "Optimal distributed control of a diffuse interface model of tumor growth." *Nonlinearity*, **30**(6):2518, 2017.

[Chu10] N. Chutsagulprom. *Thin film flows in curved tubes.* PhD thesis, University of Oxford, UK, 2010.

[CJT03] J. A. Carrillo, A. Jüngel, and S. Tang. "Positive entropic schemes for a nonlinear fourth-order parabolic equation." *Discrete and Continuous Dynamical Systems-B*, **3**(1):1–20, 2003.

[CM06] R. V. Craster and O. K. Matar. "On viscous beads flowing down a vertical fibre." *Journal of Fluid Mechanics*, **553**:85–105, 2006.

[CM09] R. V. Craster and O. K. Matar. "Dynamics and stability of thin liquid films." *Reviews of Modern Physics*, **81**(3):1131, 2009.

[CPT10] M. Chugunova, M. C. Pugh, and R. M. Taranets. "Nonnegative solutions for a long-wave unstable thin film equation with convection." *SIAM Journal on Mathematical Analysis*, **42**(4):1826–1853, 2010.

[CUM00] H. Chinju, K. Uchiyama, and Y. H. Mori. ""String-of-beads" flow of liquids on vertical wires for gas absorption." *AIChE Journal*, **46**(5):937–945, 2000.

[CWW19] W. Chen, C. Wang, X. Wang, and S. M. Wise. "Positivity-preserving, energy stable numerical schemes for the Cahn-Hilliard equation with logarithmic potential." *Journal of Computational Physics: X*, **3**:100031, 2019.

[DCF98] E. J. Doedel, A. R. Champneys, T. F. Fairgrieve, Y. A. Kuznetsov, B. Sandstede, and X. Wang. "Auto97: Continuation and bifurcation software for ordinary differential equations (with homcont)." *Technical Report, Concordia University*, 1998.

[DD07] É. J. M. Delhez and É. Deleersnijder. "Overshootings and spurious oscillations caused by biharmonic mixing." *Ocean Modelling*, **17**(3):183–198, 2007.

[DJF20] Y. Dukler, H. Ji, C. Falcon, and A. L. Bertozzi. "Theory for undercompressive shocks in tears of wine." *Physical Review Fluids*, **5**(3):034002, 2020.

[DJL21] Q. Du, L. Ju, X. Li, and Z. Qiao. "Maximum bound principles for a class of semilinear parabolic equations and exponential time-differencing schemes." *SIAM Review*, **63**(2):317–359, 2021.

[DK02] J. A. Diez and L. Kondic. "Computing three-dimensional thin film flows including contact lines." *Journal of Computational Physics*, **183**(1):274–306, 2002.

[DKB00] J. A. Diez, L. Kondic, and A. L. Bertozzi. "Global models for moving contact lines." *Physical Review E*, **63**(1):011208, 2000.

[DLL19] Z. Ding, Z. Liu, R. Liu, and C. Yang. "Breakup of ultra-thin liquid films on vertical fiber enhanced by Marangoni effect." *Chemical Engineering Science*, **199**:342–348, 2019.

[DLS91] B. Derrida, J. L. Lebowitz, E. R. Speer, and H. Spohn. "Dynamics of an anchored Toom interface." *Journal of Physics A: Mathematical and General*, **24**(20):4805, 1991.

[DMM10] B. Düring, D. Matthes, and J. P. Milišić. "A gradient flow scheme for nonlinear fourth order equations." *Discrete and Continuous Dynamical Systems - B*, **14**(3):935, 2010.

[DMR05] P. Degond, F. Méhats, and C. Ringhofer. "Quantum energy-transport and drift-diffusion models." *Journal of Statistical Physics*, **118**:625–667, 2005.

[DP11] J. Droniou and C. L. Potier. "Construction and convergence study of schemes preserving the elliptic local maximum principle." *SIAM Journal on Numerical Analysis*, **49**(2):459–490, 2011.

[DPM18] S. Das, H. V. Patel, E. Milacic, N. G. Deen, and J. A. M. Kuipers. "Droplet spreading and capillary imbibition in a porous medium: A coupled IB-VOF method based numerical study." *Physics of Fluids*, **30**(1):012112, 2018.

[DRG09] C. Duprat, C. Ruyer-Quil, and F. Giorgiutti-Dauphiné. "Spatial evolution of a film flowing down a fiber." *Physics of Fluids*, **21**(4):042109, 2009.

[DRK07] C. Duprat, C. Ruyer-Quil, S. Kalliadasis, and F. Giorgiutti-Dauphiné. "Absolute and convective instabilities of a viscous film flowing down a vertical fiber." *Physical Review Letters*, **98**(24):244502, 2007.

[DWZ19] L. Dong, C. Wang, H. Zhang, and Z. Zhang. "A positivity-preserving, energy stable and convergent numerical scheme for the Cahn-Hilliard equation with a Flory–Huggins–Degennes energy." *Communications in Mathematical Sciences*, **17**(4):921–939, 2019.

[ED94] J. Eggers and T. F. Dupont. "Drop formation in a one-dimensional approximation of the Navier–Stokes equation." *Journal of Fluid Mechanics*, **262**:205–221, 1994.

[Egg18] J. Eggers. "Role of singularities in hydrodynamics." *Physical Review Fluids*, **3**(11):110503, 2018.

[Eyr98] D. J. Eyre. "Unconditionally gradient stable time marching the Cahn-Hilliard equation." *MRS Online Proceedings Library (OPL)*, **529**, 1998.

[FG18] J. Fischer and G. Grün. "Existence of positive solutions to stochastic thin-film equations." *SIAM Journal on Mathematical Analysis*, **50**(1):411–455, 2018.

[Fre92] A. L. Frenkel. "Nonlinear theory of strongly undulating thin films flowing down vertical cylinders." *Europhysics Letters*, **18**(7):583, 1992.

[Fri58] A. Friedman. "Interior estimates for parabolic systems of partial differential equations." *Journal of Mathematics and Mechanics*, **7**(3):393–417, 1958.

[Gar94] C. L. Gardner. "The quantum hydrodynamic model for semiconductor devices." *SIAM Journal on Applied Mathematics*, **54**(2):409–427, 1994.

[Gat45] E. K. Gatcombe. "Lubrication characteristics of involute spur gears: A theoretical investigation." *Transactions of the American Society of Mechanical Engineers*, **67**(3):177–185, 1945.

[GB04] J. B. Greer and A. L. Bertozzi. "Traveling wave solutions of fourth order PDEs for image processing." *SIAM Journal on Mathematical Analysis*, **36**(1):38–68, 2004.

[GB21] C. T. Gabbard and J. B. Bostwick. "Asymmetric instability in thin-film flow down a fiber." *Physical Review Fluids*, **6**(3):034005, 2021.

[GBR02] G. Grün, J. Becker, and M. Rumpf. "On space-time-adaptive convergent finite-element schemes for a general class of lubrication-type equations." In *Proceedings of the 5th World Congress on Computational Mechanics.*, 2002.

[GBS06] J. B. Greer, A. L. Bertozzi, and G. Sapiro. "Fourth order partial differential equations on general geometries." *Journal of Computational Physics*, **216**(1):216–246, 2006.

[Gen85] P.-G. de Gennes. "Wetting: statics and dynamics." *Reviews of Modern Physics*, **57**(3):827, 1985.

[GG19] H. Grillmeier and G. Grün. "Nonnegativity preserving convergent schemes for stochastic porous-medium equations." *Mathematics of Computation*, **88**(317):1021–1059, 2019.

[GH10] J. M. Gomba and G. M. Homsy. "Regimes of thermocapillary migration of droplets under partial wetting conditions." *Journal of Fluid Mechanics*, **647**:125–142, 2010.

[GJS04] P. H. Gaskell, P. K. Jimack, M. Sellier, and H. M. Thompson. "Efficient and accurate time adaptive multigrid simulations of droplet spreading." *International Journal for Numerical Methods in Fluids*, **45**(11):1161–1186, 2004.

[GLH12] J. Grünig, E. Lyagin, S. Horn, T. Skale, and M. Kraume. "Mass transfer characteristics of liquid films flowing down a vertical wire in a counter current gas flow." *Chemical Engineering Science*, **69**(1):329–339, 2012.

[GM81] H. P. Greenspan and B. M. McCay. "On the wetting of a surface by a very viscous fluid." *Studies in Applied Mathematics*, **64**(2):94–112, 1981.

[Gom12] J. M. Gomba. "Thin-film flows with moving contact lines: An approach to reducing computing time." *Physical Review E*, **85**(5):056701, 2012.

[GR00] G. Grün and M. Rumpf. "Nonnegativity preserving convergent schemes for the thin film equation." *Numerische Mathematik*, **87**(1):113–152, 2000.

[GR01] G. Grün and M. Rumpf. "Simulation of singularities and instabilities arising in thin film flow." *European Journal of Applied Mathematics*, **12**(3):293–320, 2001.

[Gre78] H. P. Greenspan. "On the motion of a small viscous droplet that wets a surface." *Journal of Fluid Mechanics*, **84**(1):125–143, 1978.

[Gru01] G. Grün. "On Bernis' interpolation inequalities in multiple space dimensions." *Zeitschrift für Analysis und ihre Anwendungen*, **20**(4):987–998, 2001.

[Gru03] G. Grün. "On the convergence of entropy consistent schemes for lubrication type equations in multiple space dimensions." *Mathematics of Computation*, **72**(243):1251–1279, 2003.

[Gru05] G. Grün. "Droplet spreading under weak slippage—existence for the Cauchy problem." *Communications in Partial Differential Equations*, **29**(11-12):1697–1744, 2005.

[GT06] L. Gosse and G. Toscani. "Lagrangian numerical approximations to one-dimensional convolution-diffusion equations." *SIAM Journal on Scientific Computing*, **28**(4):1203–1227, 2006.

[GTV09] T. Gilet, D. Terwagne, and N. Vandewalle. "Digital microfluidics on a wire." *Applied Physics Letters*, **95**(1):014106, 2009.

[GW22] F. S. Goucher and H. Ward. "XC. A problem in viscosity: The thickness of liquid films formed on solid surfaces under dynamic conditions." *The London, Edinburgh, and Dublin Philosophical Magazine and Journal of Science*, **44**:1002–1014, 1922.

[GW03] K. B. Glasner and T. P. Witelski. "Coarsening dynamics of dewetting films." *Physical Review E*, **67**(1):016302, 2003.

[HBB15] S. Haefner, M. Benzaquen, O. Bäumchen, T. Salez, R. Peters, J. D. McGraw, K. Jacobs, E. Raphaël, and K. Dalnoki-Veress. "Influence of slip on the Plateau-Rayleigh instability on a fibre." *Nature Communications*, **6**(1):7409, 2015.

[HH20] J. Hu and X. Huang. "A fully discrete positivity-preserving and energy-dissipative finite difference scheme for Poisson–Nernst–Planck equations." *Numerische Mathematik*, **145**(1):77–115, 2020.

[HIM94] K. Hattori, M. Ishikawa, and Y. H. Mori. "Strings of liquid beads for gas-liquid contact operations." *AIChE Journal*, **40**(12):1983–1992, 1994.

[Hoc81] L. M. Hocking. "Sliding and spreading of thin two-dimensional drops." *The Quarterly Journal of Mechanics and Applied Mathematics*, **34**(1):37–55, 1981.

[HSW22] F. Huang, J. Shen, and K. Wu. "Bound/positivity preserving and unconditionally stable schemes for a class of fourth order nonlinear equations." *Journal of Computational Physics*, **460**:111177, 2022.

[HW17] D. Halpern and H.-H. Wei. "Slip-enhanced drop formation in a liquid falling down a vertical fibre." *Journal of Fluid Mechanics*, **820**:42–60, 2017.

[Isr11] J. N. Israelachvili. *Intermolecular and surface forces (Third Edition)*. Academic Press, 2011.

[JD22] W. Jiang and Z. Ding. "Thin liquid films down a vertical microfiber: Effect of curvature elasticity." *Physical Review E*, **105**(3):035104, 2022.

[JFS19] H. Ji, C. Falcon, A. Sadeghpour, Z. Zeng, Y. S. Ju, and A. L. Bertozzi. "Dynamics of thin liquid films on vertical cylindrical fibres." *Journal of Fluid Mechanics*, **865**:303–327, 2019.

[JFS21] H. Ji, C. Falcon, E. Sedighi, A. Sadeghpour, Y. S. Ju, and A. L. Bertozzi. "Thermally-driven coalescence in thin liquid film flowing down a fibre." *Journal of Fluid Mechanics*, **916**, 2021.

[JM08] A. Jüngel and D. Matthes. "The Derrida–Lebowitz–Speer–Spohn equation: Existence, nonuniqueness, and decay rates of the solutions." *SIAM Journal on Mathematical Analysis*, **39**(6):1996–2015, 2008.

[JP01] A. Jüngel and R. Pinnau. "A positivity-preserving numerical scheme for a nonlinear fourth order parabolic system." *SIAM Journal on Numerical Analysis*, **39**(2):385–406, 2001.

[JP03] A. Jüngel and R. Pinnau. "Convergent semidiscretization of a nonlinear fourth order parabolic system." *ESAIM: Mathematical Modelling and Numerical Analysis*, **37**(2):277–289, 2003.

[JSJ20] H. Ji, A. Sadeghpour, Y. S. Ju, and A. L. Bertozzi. "Modelling film flows down a fibre influenced by nozzle geometry." *Journal of Fluid Mechanics*, **901**, 2020.

[JTC22] H. Ji, R. Taranets, and M. Chugunova. "On travelling wave solutions of a model of a liquid film flowing down a fibre." *European Journal of Applied Mathematics*, **33**(5):864–893, 2022.

[Jun09] A. Jüngel. *Transport equations for semiconductors*. Springer, 2009.

[JW17] H. Ji and T. P. Witelski. "Finite-time thin film rupture driven by modified evaporative loss." *Physica D: Nonlinear Phenomena*, **342**:1–15, 2017.

[KA09] J. Klentzman and V. S. Ajaev. "The effect of evaporation on fingering instabilities." *Physics of Fluids*, **21**(12):122101, 2009.

[Kal00] S. Kalliadasis. "Nonlinear instability of a contact line driven by gravity." *Journal of Fluid Mechanics*, **413**:355–378, 2000.

[KB13] T. Kostić and A. L. Bertozzi. "Statistical density estimation using threshold dynamics for geometric motion." *Journal of Scientific Computing*, **54**:513–530, 2013.

[KC94] S. Kalliadasis and H.-C. Chang. "Drop formation during coating of vertical fibres." *Journal of Fluid Mechanics*, **261**:135–168, 1994.

[KCD16] P. K. Kundu, I. M. Cohen, and D. R. Dowling. "Chapter 9 - laminar flow." In *Fluid mechanics (Sixth Edition)*, pp. 409–467. Academic Press, Boston, 2016.

[KD01] L. Kondic and J. A. Diez. "Pattern formation in the flow of thin films down an incline: Constant flux configuration." *Physics of Fluids*, **13**(11):3168–3184, 2001.

[KD06] I. Klapper and J. Dockery. "Role of cohesion in the material description of biofilms." *Physical Review E*, **74**(3):031902, 2006.

[KDB01] I. L. Kliakhandler, S. H. Davis, and S. G. Bankoff. "Viscous beads on vertical fibre." *Journal of Fluid Mechanics*, **429**:381–390, 2001.

[KF94] V. I. Kerchman and A. L. Frenkel. "Interactions of coherent structures in a film flow: simulations of a highly nonlinear evolution equation." *Theoretical and Computational Fluid Dynamics*, **6**(4):235–254, 1994.

[Kin89] J. R. King. "The isolation oxidation of silicon: the reaction-controlled case." *SIAM Journal on Applied Mathematics*, **49**(4):1064–1080, 1989.

[KJB23] B. Kim, H. Ji, A. L. Bertozzi, A. Sadeghpour, and Y. S. Ju. "A positivity-preserving numerical method for a thin liquid film on a vertical cylindrical fiber (submitted for publication)." *Journal of Computational Physics*, **218**(1):152–166, 2023.

[KRS12a] S. Kalliadasis, C. Ruyer-Quil, B. Scheid, and M. G. Velarde. *Boundary Layer Approximation*, pp. 65–93. Springer London, London, 2012a.

[KRS12b] S. Kalliadasis, C. Ruyer-Quil, B. Scheid, and M. G. Velarde. *Introduction*, pp. 1–19. Springer London, London, 2012b.

[KRS12c] S. Kalliadasis, C. Ruyer-Quil, B. Scheid, and M. G. Velarde. *Falling liquid films*. Springer, 2012c.

[KS08] E. Khain and L. M. Sander. "Generalized Cahn-Hilliard equation for biological applications." *Physical Review E*, **77**(5):051129, 2008.

[Lac82] A. A. Lacey. "The motion with slip of a thin viscous droplet over a solid surface." *Studies in Applied Mathematics*, **67**(3):217–230, 1982.

[Lau05] R. S. Laugesen. "New dissipated energies for the thin fluid film equation." *Communications on Pure and Applied Analysis*, **4**(3):613–634, 2005.

[LC20] P. Li and Y. Chao. "Marangoni instability of self-rewetting films modulated by chemical reactions flowing down a vertical fibre." *Chemical Engineering Science*, **227**:115936, 2020.

[LeV90] R. J. LeVeque. *Numerical methods for conservation laws*. Springer, 1990.

[LGB07] H.-W. Lu, K. Glasner, A. Bertozzi, and C.-J. Kim. "A diffuse-interface model for electrowetting drops in a Hele-Shaw cell." *Journal of Fluid Mechanics*, **590**:411–435, 2007.

[LHV13] C. Lu, W. Huang, and E. S. Van Vleck. "The cutoff method for the numerical computation of nonnegative solutions of parabolic PDEs with application to anisotropic diffusion and lubrication-type equations." *Journal of Computational Physics*, **242**:24–36, 2013.

[LI94] M. Labronici and H. Ishida. "Toughening composites by fiber coating: a review." *Composite Interfaces*, **2**(3):199–234, 1994.

[LL88] L. Landau and B. Levich. "Dragging of a liquid by a moving plate." In *Dynamics of Curved Fronts*, pp. 141–153. Elsevier, 1988.

[Lor78] F. R. S. Lord Rayleigh. "On the instability of jets." *Proceedings of the London Mathematical Society*, **1**(1):4–13, 1878.

[LPD19] Y. Liu, C. Peco, and J. Dolbow. "A fully coupled mixed finite element method for surfactants spreading on thin liquid films." *Computer Methods in Applied Mechanics and Engineering*, **345**:429–453, 2019.

[LYZ20] B. Li, J. Yang, and Z. Zhou. "Arbitrarily high-order exponential cut-off methods for preserving maximum principle of parabolic equations." *SIAM Journal on Scientific Computing*, **42**(6):A3957–A3978, 2020.

[MBD08] K. L. Maki, R. J. Braun, T. A. Driscoll, and P. E. King-Smith. "An overset grid method for the study of reflex tearing." *Mathematical Medicine and Biology: A Journal of the IMA*, **25**(3):187–214, 2008.

[MBH10] K. L. Maki, R. J. Braun, W. D. Henshaw, and P. E. King-Smith. "Tear film dynamics on an eye-shaped domain I: pressure boundary conditions." *Mathematical Medicine and Biology: A Journal of the IMA*, **27**(3):227–254, 2010.

[MBU10] K. L. Maki, R. J. Braun, P. Ucciferro, W. D. Henshaw, and P. E. King-Smith. "Tear film dynamics on an eye-shaped domain. part 2. Flux boundary conditions." *Journal of Fluid Mechanics*, **647**:361–390, 2010.

[MCT02] T. G. Myers, J. P. F. Charpin, and C. P. Thompson. "Slowly accreting ice due to supercooled water impacting on a cold surface." *Physics of Fluids*, **14**(1):240–256, 2002.

[Mic15] M. Michal. *Analytical and Numerical Analysis of Lubrication Coating Flow Models*. PhD thesis, The Claremont Graduate University, 2015.

[MO17] D. Matthes and H. Osberger. "A convergent Lagrangian discretization for a nonlinear fourth-order equation." *Foundations of Computational Mathematics*, **17**(1):73–126, 2017.

[Moc83] M. S. Mock. *Analysis of mathematical models of semiconductor devices*. Boole Press, 1983.

[Mun04] A. Münch. "Fingering instability in dewetting films induced by slippage." 2004.

[MW05] A. Münch and B. Wagner. "Contact-line instability of dewetting thin films." *Physica D: Nonlinear Phenomena*, **209**(1-4):178–190, 2005.

[MWW05] A. Münch, B. Wagner, and T. P. Witelski. "Lubrication models with small to large slip lengths." *Journal of Engineering Mathematics*, **53**(3):359–383, 2005.

[MWW18] A. Mavromoustaki, L. Wang, J. Wong, and A. L. Bertozzi. "Surface tension effects for particle settling and resuspension in viscous thin films." *Nonlinearity*, **31**(7):3151, 2018.

[Mye98] T. G. Myers. "Thin films with high surface tension." *SIAM Review*, **40**(3):441–462, 1998.

[NCM15] S. Nesic, R. Cuerno, E. Moro, and L. Kondic. "Fully nonlinear dynamics of stochastic thin-film dewetting." *Physical Review E*, **92**(6):061002, 2015.

[NM83] P. Neogi and C. A. Miller. "Spreading kinetics of a drop on a rough solid surface." *Journal of Colloid and Interface Science*, **92**(2):338–349, 1983.

[NO09] E. Novbari and A. Oron. "Energy integral method model for the nonlinear dynamics of an axisymmetric thin liquid film falling on a vertical cylinder." *Physics of Fluids*, **21**(6):062107, 2009.

[OB99] A. Oron and S. Bankoff. "Dewetting of a heated surface by an evaporating liquid film under conjoining/disjoining pressures." *Journal of Colloid and Interface Science*, **218**(1):152–166, 1999.

[OB01] A. Oron and S. G. Bankoff. "Dynamics of a condensing liquid film under conjoining/disjoining pressures." *Physics of Fluids*, **13**(5):1107–1117, 2001.

[ODB97] A. Oron, S. H. Davis, and S. G. Bankoff. "Long-scale evolution of thin liquid films." *Reviews of Modern Physics*, **69**(3):931, 1997.

[OM17] H. Osberger and D. Matthes. "Convergence of a fully discrete variational scheme for a thin-film equation." *Topological Optimization and Optimal Transport: In the Applied Sciences*, **17**:356, 2017.

[PGS01] R. D. Passo, L. Giacomelli, and A. Shishkov. "The thin film equation with nonlinear diffusion." *Communications in Partial Differential Equations*, **26**(9-10):1509–1557, 2001.

[PHM19] D. Peschka, S. Haefner, L. Marquant, K. Jacobs, A. Münch, and B. Wagner. "Signatures of slip in dewetting polymer films." *Proceedings of the National Academy of Sciences*, **116**(19):9275–9284, 2019.

[Pin00] R. Pinnau. "The linearized transient quantum drift diffusion model—stability of stationary states." *ZAMM-Zeitschrift für Angewandte Mathematik und Mechanik*, **80**(5):327–344, 2000.

[Pin01] R. Pinnau. "Numerical approximation of the transient quantum drift-diffusion model." *Nonlinear Analysis: Theory, Methods and Applications*, **47**(9):5849–5860, 2001.

[Pin02] R. Pinnau. "A review on the quantum drift-diffusion model." *Transport Theory and Statistical Physics*, **31**(4-6):367–395, 2002.

[PN03] C. D. Park and T. Nosoko. "Three-dimensional wave dynamics on a falling film and associated mass transfer." *AIChE Journal*, **49**(11):2715–2727, 2003.

[PRT04] L. Pareschi, G. Russo, and G. Toscani. "A kinetic approximation of Hele–Shaw flow." *Comptes Rendus Mathematique*, **338**(2):177–182, 2004.

[PVK18] K. Poulios, A. Vølund, and P. Klit. "Finite element method for starved hydrodynamic lubrication with film separation and free surface effects." *Computer Methods in Applied Mechanics and Engineering*, **339**:281–297, 2018.

[Que90] D. Quéré. "Thin films flowing on vertical fibers." *Europhysics Letters*, **13**(8):721, 1990.

[Que99] D. Quéré. "Fluid coating on a fiber." *Annual Review of Fluid Mechanics*, **31**(1):347–384, 1999.

[Raj13] A. Rajasekharan. "Effects of varied physical mechanisms on the evolution of lubricant interface during heat-assisted magnetic recording." In *ASME 2013 Conference on Information Storage and Processing Systems*. American Society of Mechanical Engineers Digital Collection, 2013.

[RB92] B. Reisfeld and S. G. Bankoff. "Non-isothermal flow of a liquid film on a horizontal cylinder." *Journal of Fluid Mechanics*, **236**:167–196, 1992.

[RK12] C. Ruyer-Quil and S. Kalliadasis. "Wavy regimes of film flow down a fiber." *Physical Review E*, **85**(4):046302, 2012.

[RTG08] C. Ruyer-Quil, P. Treveleyan, F. Giorgiutti-Dauphiné, C. Duprat, and S. Kalliadasis. "Modelling film flows down a fibre." *Journal of Fluid Mechanics*, **603**:431–462, 2008.

[RTG09] C. Ruyer-Quil, S. P. M. J. Trevelyan, F. Giorgiutti-Dauphiné, C. Duprat, and S. Kalliadasis. "Film flows down a fiber: Modeling and influence of streamwise viscous diffusion." *The European Physical Journal Special Topics*, **166**(1):89–92, 2009.

[SAB94] T. R. Salamon, R. C. Armstrong, and R. A. Brown. "Traveling waves on vertical films: Numerical analysis using the finite element method." *Physics of Fluids*, **6**(6):2202–2220, 1994.

[SCM06] G. M. Sisoev, R. V. Craster, O. K. Matar, and S. V. Gerasimov. "Film flow down a fibre at moderate flow rates." *Chemical Engineering Science*, **61**(22):7279–7298, 2006.

[SGM02] A. Q. Shen, B. Gleason, G. H. McKinley, and H. A. Stone. "Fiber coating with surfactant solutions." *Physics of Fluids*, **14**(11):4055–4068, 2002.

[SMC12] T. Salez, J. D. McGraw, S. L. Cormier, O. Bäumchen, K. Dalnoki-Veress, and E. Raphaël. "Numerical solutions of thin-film equations for polymer flows." *The European Physical Journal E*, **35**(11):1–9, 2012.

[SNG08] L. B. Smolka, J. North, and B. K. Guerra. "Dynamics of free surface perturbations along an annular viscous film." *Physical Review E*, **77**(3):036301, 2008.

[Sol65] V. A. Solonnikov. "On boundary value problems for linear parabolic systems of differential equations of general form." In *Boundary value problems of mathematical physics. Part 3. On boundary value problems for linear parabolic systems of differential equations of general form*, volume 83, pp. 3–163. Trudy Matematicheskogo Instituta imeni V.A. Steklova, 1965.

[SRX07] P. Sun, R. D. Russell, and J. Xu. "A new adaptive local mesh refinement algorithm and its application on fourth order thin film flow problem." *Journal of Computational Physics*, **224**(2):1021–1048, 2007.

[SZJ17] A. Sadeghpour, Z. Zeng, and Y. S. Ju. "Effects of nozzle geometry on the fluid dynamics of thin liquid films flowing down vertical strings in the Rayleigh-Plateau regime." *Langmuir*, **33**(25):6292–6299, 2017.

[SZJ19] A. Sadeghpour, Z. Zeng, H. Ji, N. Dehdari Ebrahimi, A. L. Bertozzi, and Y. S. Ju. "Water vapor capturing using an array of traveling liquid beads for desalination and water treatment." *Science Advances*, **5**(4):eaav7662, 2019.

[Tay60] G. I. Taylor. "Deposition of a viscous fluid on a plane surface." *Journal of Fluid Mechanics*, **9**(2):218–224, 1960.

[Tay63] G. I. Taylor. "Cavitation of a viscous fluid in narrow passages." *Journal of Fluid Mechanics*, **16**(4):595–619, 1963.

[TK87] A. B. Tayler and J. R. King. "Free boundaries in semi-conductor fabrication." In *International Colloquium on Free Boundary Problems, Irsee, Bavaria, West Germany*, volume 1, pp. 243–259, 1987.

[TKS07] J. Trice, R. Kalyanaraman, and R. Sureshkumar. "Computational modelling of laser-induced self-organization in nanoscopic metal films for predictive nanomanufacturing." In *Instrumentation, Metrology, and Standards for Nanomanufacturing*, p. 66480K. International Society for Optics and Photonics, 2007.

[Tri92] Y. Y. Trifonov. "Steady-state traveling waves on the surface of a viscous liquid film falling down on vertical wires and tubes." *AIChE journal*, **38**(6):821–834, 1992.

[TW18] R. M. Taranets and J. T. Wong. "Existence of weak solutions for particle-laden flow with surface tension." *Discrete and Continuous Dynamical Systems-A*, **38**(10):4979, 2018.

[UMO03] K. Uchiyama, H. Migita, R. Ohmura, and Y. H. Mori. "Gas absorption into string-of-beads liquid flow with chemical reaction: application to carbon dioxide separation." *International Journal of Heat and Mass Transfer*, **46**(3):457–468, 2003.

[VR03] B. P. Vollmayr-Lee and A. D. Rutenberg. "Fast and accurate coarsening simulation with an unconditionally stable time step." *Physical Review E*, **68**(6):066703, 2003.

[VRB18] O. Vantzos, S. Raz, and M. Ben-Chen. "Real-time viscous thin films." *ACM Transactions on Graphics (TOG)*, **37**(6):1–10, 2018.

[WB03] T. P. Witelski and M. Bowen. "ADI schemes for higher-order nonlinear diffusion equations." *Applied Numerical Mathematics*, **45**(2-3):331–351, 2003.

[WD82] M. B. Williams and S. H. Davis. "Nonlinear theory of film rupture." *Journal of Colloid and Interface Science*, **90**(1):220–228, 1982.

[WLF08] S. M. Wise, J. S. Lowengrub, H. B. Frieboes, and V. Cristini. "Three-dimensional multispecies nonlinear tumor growth—I: model and numerical method." *Journal of Theoretical Biology*, **253**(3):524–543, 2008.

[WR04] S. J. Weinstein and K. J. Ruschak. "Coating flows." *Annual Review of Fluid Mechanics*, **36**:29–53, 2004.

[WT66] D. A. White and J. A. Tallmadge. "A theory of withdrawal of cylinders from liquid baths." *AIChE Journal*, **12**(2):333–339, 1966.

[XD85] J.-J. Xu and S. H. Davis. "Instability of capillary jets with thermocapillarity." *Journal of Fluid Mechanics*, **161**:1–25, 1985.

[YH13] L. Yu and J. Hinch. "The velocity of 'large' viscous drops falling on a coated vertical fibre." *Journal of Fluid Mechanics*, **737**:232–248, 2013.

[ZB00] L. Zhornitskaya and A. L. Bertozzi. "Positivity-preserving numerical schemes for lubrication-type equations." *SIAM Journal on Numerical Analysis*, **37**(2):523–555, 2000.

[Zha09] Y. Zhang. "Counting the stationary states and the convergence to equilibrium for the 1-D thin film equation." *Nonlinear Analysis: Theory, Methods and Applications*, **71**(5-6):1425–1437, 2009.

[ZL99] W. W. Zhang and J. R. Lister. "Similarity solutions for van der Waals rupture of a thin film on a solid substrate." *Physics of Fluids*, **11**(9):2454–2462, 1999.

[ZS10] X. Zhang and C.-W. Shu. "On positivity-preserving high order discontinuous Galerkin schemes for compressible Euler equations on rectangular meshes." *Journal of Computational Physics*, **229**(23):8918–8934, 2010.

[ZS11] X. Zhang and C.-W. Shu. "Maximum-principle-satisfying and positivity-preserving high-order schemes for conservation laws: survey and new developments." *Proceedings of the Royal Society A: Mathematical, Physical and Engineering Sciences*, **467**(2134):2752–2776, 2011.

[ZSJ18] Z. Zeng, A. Sadeghpour, and Y. S. Ju. "Thermohydraulic characteristics of a multi-string direct-contact heat exchanger." *International Journal of Heat and Mass Transfer*, **126**:536–544, 2018.

[ZSJ19] Z. Zeng, A. Sadeghpour, and Y. S. Ju. "A highly effective multi-string humidifier with a low gas stream pressure drop for desalination." *Desalination*, **449**:92–100, 2019.

[ZSW17] Z. Zeng, A. Sadeghpour, G. Warrier, and Y. S. Ju. "Experimental study of heat transfer between thin liquid films flowing down a vertical string in the Rayleigh-Plateau instability regime and a counterflowing gas stream." *International Journal of Heat and Mass Transfer*, **108**:830–840, 2017.

[ZWJ15] Z. Zeng, G. Warrier, and Y. S. Ju. "Study of the fluid dynamics of thin liquid films flowing down a vertical string with counterflow of gas." In *ASME International Mechanical Engineering Congress and Exposition*, volume 8B. American Society of Mechanical Engineers, 2015.

[ZXR22] Q. Zhao, S. Xu, and W. Ren. "A level set method for the simulation of moving contact lines in three dimensions." *Communications in Computational Physics*, **32**:1310–1331, 2022.

[ZZS23] C. Zhao, Y. Zhang, and T. Si. "Slip-enhanced Rayleigh–Plateau instability of a liquid film on a fibre." *Journal of Fluid Mechanics*, **954**:A46, 2023.